MODELLING THE HYDRODYNAMICS WITHIN THE MANGROVE TIDAL FLATS IN THE FIRTH OF THAMES

A thesis

submitted in partial fulfilment

of the requirements for the degree

of

Master of Science (Research)

in Earth and Ocean Sciences

at

The University of Waikato

by

Rebekah Rose Haughey

THE UNIVERSITY OF
WAIKATO
Te Whare Wānanga o Waikato

2017

ABSTRACT

Understanding how mangroves control shoreline stability, through altering hydrodynamic and sedimentation patterns, is important to predicting how resilient our coastline is to climate change. Recent work has shown that some mangrove ecosystems may modify the morphology, and allow the seabed to evolve upward with rising sea level, and thus alleviating the pressure on coastal adaptation.

This study is focussed on improving the understanding of the hydrodynamics within the mangrove habitat in the Firth of Thames, New Zealand. The mangrove habitat within the Firth of Thames is a shallow, muddy and rapidly prograding environment. The main aim of this study was to determine whether or not, the mangroves influence the dynamics of the tidal wave propagation, which in turn can have implications for the sedimentation patterns and shoreline stability within the Firth of Thames.

A hydrodynamic model for the Firth of Thames was developed using Delft3D. A coarse resolution grid was created to simulate the offshore tidal wave propagation and used to force a nested, fine resolution grid within the mangrove intertidal flats. A field deployment was completed during May 2016, where in the offshore region water levels, current velocities and suspended sediment measurements were taken, and within the mangrove forest, water levels, bed elevations and vegetation characteristics were measured. Field measurements were used to calibrate both the overall and nested models.

Comparisons between model outputs, with and without vegetation included in the model, indicate that the presence of mangroves does influence the tidal wave dynamics across the intertidal flats. Two of the main effects of vegetation were reduced current velocity and tidal amplitude. Regardless of whether mangroves were present, the model showed flood dominance across the upper intertidal flat and ebb dominance at the seaward edge of the intertidal flat. However, with vegetation included this pattern of tidal asymmetry was enhanced, due to the nonlinear effect of friction.

A series of numerical experiments were also performed to understand the control of sea bed roughness and vegetation characteristics (vegetation roughness, pneumatophore height, plus pneumatophore and tree density) on the size, spatial changes and timing of tidal currents. Pneumatophore density had the largest influence on model outputs, with increasing pneumatophore density causing a reduction in currents and a delay in the drainage of the ebb tide.

Based on the hydrodynamic model outputs and measurements of offshore suspended sediment concentrations, rough calculations were completed to estimate the net flux of sediment into the forest over time. Estimated sediment fluxes were surprisingly similar to the estimated volume deposited sediment between the 2005 and 2016 elevation surveys.

Physical processes, such as tidal asymmetry, are likely to have caused the initial accretion and tidal flat development, making it suitable for mangrove growth. However, now that there is a vast area of mangroves, they are altering the hydrodynamics and therefore are also contributing to the accretion and overall stability of the system.

ACKNOWLEDGEMENTS

First and foremost, I would like to sincerely thank my two awesome supervisors, Dr Karin Bryan and Dr Erik Horstman. Thank you both for all of your support and advice throughout all aspects of this project. I have really appreciated your ongoing enthusiasm and also your contribution towards the field work was super helpful.

Thank you to the Waikato Regional Council for funding the project. I am also grateful to have received the Dr Stella Frances Scholarship from the Waikato Regional Council and the Department of Conservation, and also the Environmental Research Institute Scholarship from the University of Waikato.

I also thank the Waikato Regional Council for providing me with data. I especially thank Stephen Hunt for helping me to source the data from different people within the Council.

Thank you to Andrew Swales, from NIWA, for providing me with elevation data from the previous surveys.

A huge thanks to Dean Sandwell, for helping with the setup and deployment of instruments, I would have been lost otherwise. Also, thank you Dirk Immenga for organising all of the offshore deployment. I would also like to thank Ben Stewart, Thomas El'Saillos, Dudley Bell, Warrick Powrie for assisting with the field work in the lovely, muddy, Firth of Thames. Thank you also, to those involved in the Marsden project (field team: Karin Bryan, Erik Horstman, Julia Mullarney, Caitland Gillard, Hieu Nguyen, David Culliford, Rex Fairweather), for providing me with velocity data and thank you to Julia Mullarney for providing water level data from an earlier experiment.

To all of the members in the Coastal Marine Group who have helped answer my various queries in the office, thank you. Especially thank you to Berengere Dejeans for being my patient Matlab teacher. Thank you to Glen Stichbury for assisting me with processing some of the bathymetry/GIS data and to Liz Brodie and Brett Loper for the technical support with computer setups and installing Delft3D.

I would like to thank the team at MetOcean for allowing me to occasionally use some desk space throughout the year. Also, thank you to Sarah Gardiner for helping me with understanding different bathymetric data sets.

And last but not least, a massive thanks to my family and friends. Your support, encouragement and prayers have been an essential part in helping me to successfully complete this thesis.

TABLE OF CONTENTS

LIST OF FIGURES

CHAPTER ONE

CHAPTER THREE

CHAPTER FOUR

CHAPTER FIVE

CHAPTER SIX

CHAPTER SEVEN

LIST OF TABLES

CHAPTER THREE

CHAPTER FOUR

CHAPTER FIVE

CHAPTER SIX

CHAPTER SEVEN

CHAPTER ONE – INTRODUCTION

1.1 Overview

Mangrove ecosystems have a wide range of ecological, economic and cultural values. However, mangrove systems are fragile and it is not clear whether they will remain stable during global climate change and increasing anthropogenic pressure (Duke *et al.*, 2007; Donato *et al.,* 2011). Field and theoretical studies have shown that biophysical functioning of mangrove habitats involves complex feedbacks between the flow, sediment and vegetation (van Maanen *et al.*, 2015; Horstman *et al.,* 2015; Furukawa *et al.,* 1997). Typically, mangrove forests are regarded as mud sinks, as the drag imposed by the vegetation reduces current velocity which in turn favours sediment accumulation (Horstman *et al.,* 2015; Wolanski, 1995). A key question that is currently being posed by coastal scientists is whether the morphological accretion of tidal flats can keep up with sea level rise and how mangroves contribute to mediating accretion rates (Woodroffe, 1990; van Maanen *et al.*, 2015).

The Firth of Thames is an interesting site to study the biophysical feedbacks within mangrove forests as, unlike many of the previously studied sites; it is a rapidly expanding, vast area of mangrove intertidal flats that lacks extensive channel networks. In addition to the Firth's different morphology, a recent study by Swales *et al.,* (2015) indicates that the mangrove recruitment does not measurably enhance sedimentation rates, which is in contrast to previous studies.

Swales *et al.* (2015), focused on determining whether the mangroves act as opportunists, with their development being driven by preceding accretion events and favourable physical processes or whether biophysical feedbacks with the recruiting mangroves strongly influence sedimentation and resulting shoreline morphology. Through investigating sediment cores, Swales *et al.* (2015) suggest that the influence of biophysical feedbacks on sedimentation is minor, as the major transition from low to high sediment accumulation rates occurred before mangroves were established within the system. Swales *et al.* (2015) also implies that once the mangrove forest had matured, the sediment accumulation rates were

equal to that rate of sea level rise due to the negative feedback between surface-elevation gain and sediment delivery. These findings differ from other studies as they suggest that the mangroves have little influence on the evolution of intertidal flat system, and instead their distribution is solely the result of physical processes. However, Swales *et al.* (2015) mentions that the evolution of the mangrove intertidal flat system is much more complex than simple tidal flat progradation and accretion with sea level changes.

So, although the mangroves in the Firth of Thames may not have enhanced the initial tidal flat accretion, it is yet unknown whether and how much the present mangrove forest is contributing to the sediment accumulation rates and shoreline stability. The purpose of this study is to investigate further on what effect, if any, the mangroves have on the physical processes within the Firth of Thames, in particular on the hydrodynamics. The hydrodynamics within an intertidal system form one of the main controllers on sedimentation patterns and consequently the morphological stability. Hence, gaining insight into what interactions occur between the mangroves and hydrodynamics is one of the first important steps to a better understanding of how the system develops.

1.2 Research aim and objectives

The primary aim of this research is to determine whether or not the mangroves in the Firth of Thames influence the dynamics of the tidal wave as it propagates across the intertidal flats.

1.2.1 Hypothesis

The mangroves in the Firth of Thames influence the tidal wave dynamics through reducing current velocities and altering the shape of the tidal wave profile as it propagates across the intertidal flat.

1.2.2 Objectives

Objective 1: Collect field data for a preliminary understanding of hydrodynamic patterns within the southern Firth of Thames and for model calibration.

Objective 2: Develop a calibrated hydrodynamic model, using Delft3D, for the southern Firth of Thames, including the mangrove forest.

Objective 3: Perform a series of numerical experiments to understand the controls of seabed drag, form drag, and vegetation characteristics on the size, spatial changes and timing of tidal currents.

Objective 4: Use outputs from the hydrodynamic model to infer and discuss the influence of the mangroves on the tidal wave propagation and ultimately the stability of the forest.

1.3 Study Site

The Firth of Thames is an 800 km^2 meso-tidal estuarine embayment located on the east coast of the North Island of New Zealand (37.25°S 175.4°E) (Figure 1.1). To the east and west of the Firth are the Coromandel and Hunua Ranges, respectively, and to the south is the low-lying Hauraki Plains. The Firth receives runoff from a 3600 km^2 catchment which is primarily drained by the Waihou (1,966 km^2) and Piako (1,476 km^2) Rivers (Lovelock *et al.,* 2010). The tide within the Firth is semi-diurnal, with average spring and neap tidal ranges of 2.9 m and 2.2 m, respectively (Swales *et al.,* 2007). The Firth shoals from a maximum depth of 35 m at its inlet. The present southern shoreline is characterised by mangrove (*Avicennia marina*) habitat that extends 1 km seaward and covers 11 km^2 of intertidal mudflat. On the landward side of the mangrove forest is a constructed stop-bank with a pump station, protecting the low-lying farmland (with elevations below mean sea level) and regulating freshwater flow into the mangrove forest (Lovelock *et al.,* 2010). The intertidal shore profile has a convex shape that is characteristic of prograding muddy coasts (Swales *et al*., 2007). The intertidal morphology can be classified as a muddy coast, with large mud supply, high suspended sediment concentrations (SSC), rapid sedimentation and moderate wave exposure (Swales *et al.,* 2007). The elevation of the mangrove platform is from 1 m above mean sea level (MSL) at the seaward limit to 2 m above MSL at the landward edge. The predicted mean high water spring tide (MHWS) elevation is 1.60 m above MSL, which is exceeded by 23% of all high tides. The landward extent of mangroves is close to the upper tidal limit and is infrequently inundated. Due to the small tidal prism within the mangrove forest, tidal creeks are poorly developed (Swales *et al*., 2015 & Lovelock *et al.,* 2007.). Prior to the 1950s, mangroves were absent from the intertidal flats which were mostly characterised

by sandy sediment. However, due to the combination of large tidal range, shallow bed slope and increased fine-sediment supply, by 2007, the 70 km^2 of intertidal mudflats had built up and the 1 km wide strip of *Avicennia marina* had developed on the mudflats (Lovelock *et al.*, 2010). The study by Swales *et al*. (2007) indicates that the changes in land use, especially deforestation, during the 1850s to the 1920s resulted in the Firth receiving large amounts of mud, which consequently lead to the accretion of intertidal flats. Following the development of the intertidal flat, mangroves naturally began to colonise the flats as conditions became suitable. Lovelock *et al.* (2010) identified that there were two major forest establishment events that occurred during 1978–1981 and 1991–1995. These events coincided with sustained El Niño periods which were characterised by reduced wind and wave energy in the Firth of Thames (Lovelock *et al.*, 2010). These findings suggest that the establishment of mangrove seedlings, and therefore expansion, requires periods of low wind and wave energy (Balke *et al.*, 2015).

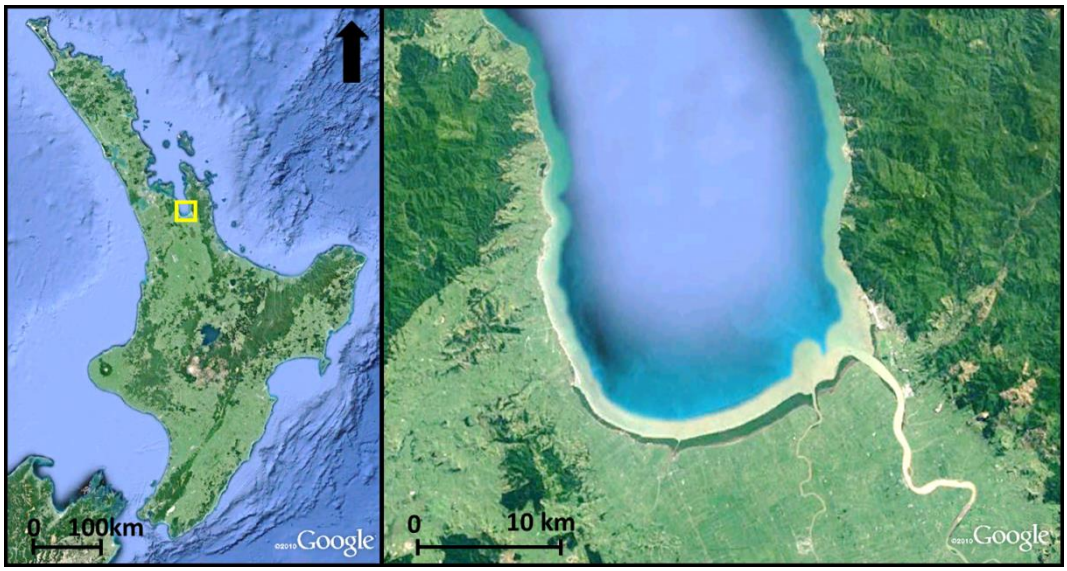

Figure 1. 1: Location of the study site, the Firth of Thames, North Island, New Zealand (Images sourced from Google Earth).

1.4 Thesis Outline

In **Chapter 2**, the findings from previous literature about mangrove ecosystems, in particular about how mangroves influence hydrodynamics and sedimentation patterns are discussed.

Chapter 3 gives a description of the field deployment completed during May 2016. Results from the field measurements are analysed and discussed to give a preliminary understanding of the hydrodynamics within the Firth of Thames.

Chapter 4 includes a description of the numerical model set up.

Chapter 5 shows the model calibration, where the field measurements described in Chapter 3 are used to calibrate water levels computed with the numerical model.

In **Chapter 6,** the outputs from the hydrodynamic model are presented. Comparisons between vegetated and non-vegetated model outputs are used to infer what influence the mangroves have on the hydrodynamics within the Firth of Thames. A sensitivity analysis is also discussed to determine the model parameters which have the largest influence on model output.

Chapter 7 contains the conclusions for the study, with the implications of the model results, in particular for sedimentation patterns. Recommendations for model improvement and future research are also included.

CHAPTER TWO - LITERATURE REVIEW

2.1 Introduction

Mangrove ecosystems have a diverse range of values. They provide ecological functions such as nursery grounds and habitat for biota, have high rates of primary productivity, they act as sinks for atmospheric carbon, and are an essential source of oceanic carbon. In the tropics, mangrove forests have significant economic value through providing food, fibre, timber, chemicals and medicine (Duke *et al.*, 2007; Donato *et al.,* 2011). Due to their position at the interface between land and sea, mangroves have also shown to provide coastal protection against storm surges and sea level rise (Donato *et al.,* 2011).

Despite their significant value, mangrove forests are disappearing worldwide by around 1-2% per year (Alongi, 2007). Some major causes for the decline in mangrove habitats include deforestation, overharvesting, aquaculture expansion, development and in some cases sea level rise (Duke *et al.,* 2007). Due to the rapid decline of mangroves around the globe there have been an increasing number of studies focused on understanding how mangrove habitats evolve and what their role is in providing coastline stability.

Mangroves typically occur at the interface between land and sea in low energy environments such as estuaries and deltas (Swales *et al.*, 2007). Such environments are largely shaped by tidal currents and sedimentation patterns. Consequently, understanding how mangroves influence flow processes, sedimentation patterns and the overall evolution of intertidal flats is of great scientific interest. Moreover, gaining insight into what interactions occur between mangroves and the physical environment is important for determining how they contribute to coastline stability, in particular shoreline accretion and erosion (Balke *et al.*, 2015; Kirwan & Megonigal, 2013; Lovelock *et al.,* 2015).

2.2 Influence of mangroves on physical processes

Recently there have been both field and theoretical modelling studies that have focused on understanding how mangroves influence hydrodynamic and sediment transport processes. One of the main ways in which mangroves influence physical

processes is through creating drag on flow, which in turn alters the direction of flow, reduces current velocities and can enhance sedimentation (Furukawa *et al.*, 1997; Wolanski, 1995; Ghisalberti, 2009; Horstman *et al.*, 2015). The effect of vegetation induced drag has implications for both the small scale sedimentation patterns and the overall evolution of intertidal flat and channel networks (van Maanen *et al.*, 2015).

Furukawa *et al*. (1997) found that the occurrence of stagnation zones behind mangrove stems can result in local trapping of water on the flood current which allows more time for the suspended sediment to be deposited. In addition to enhanced deposition, the low current velocities within mangrove forests on the ebb tide tend to lack the ability to re-suspend sediment; hence mangrove forests tend to be regions of sediment accumulation (Furukawa *et al.*, 1997; Stokes *et al.*, 2010). The effect of mangroves accelerating sedimentation rates has also been observed in the field by Stokes *et al.* (2010), who found that estuaries with mangroves present have higher bed elevations compared to estuaries where mangroves have been removed. Interestingly, even though some sites with mangroves had lower sediment availability compared to those with bare flats, the bed elevations were still higher. However, Furukawa *et al*. (1997) and Winterwerp *et al.* (2013) have noted that the ability of mangrove intertidal flats to accrete does depend on the supply of suspended sediment.

Depending on the density structure, mangroves have shown ability to significantly dampen both swell and tidal wave propagation (Massel *et al.*, 1999; Furukawa *et al.*, 1997). As a result, tidal wave distortion is often increased when mangroves are present. Mazda *et al*. (1995), Lessa & Masselink, (1995), Wolanski (1980), Furukawa (1997), Aucan & Ridd, (2000) and van Maanen *et al*., (2015) all discuss how the presence of mangrove intertidal flats can enhance ebb dominance within mangrove creeks. Due to the high friction within mangrove forests, ebb drainage becomes impaired and perched water levels can occur within the mangrove forest. Consequently, because the falling tide within the forest becomes delayed with respect to the falling tide within the creek, a strong hydraulic gradient develops which drives fast ebb velocities within the creek as the forest drains. As a result mangrove creeks often exhibit ebb dominance. Lessa & Masselink (1995) found that the steepness of the hydraulic gradient, and thus the

ebb-velocity within the mangrove creek, is proportional to the relative extent of the mangrove area.

Horstman *et al.* (2013) established that there can be different flow routing through mangrove forests depending on the elevation, exposure and vegetation density. They found that in regions with high elevated mangroves, tidal exchange occurred predominately through creek flow. In contrast, in regions where the mangroves were at a low lying elevation, the tidal flow would mainly occur as sheet flow as the forest becomes inundated. During sheet flow the magnitudes of ebbing currents showed to be heterogeneous with slower flow inside the mangrove forests and faster velocities on the mudflat in front of the forest (Horstman *et al.*, 2013). When sheet flow occurs across a mangrove intertidal flat, the extra flow resistance within the mangrove forests favours flow concentration in the channels.

As a consequence of flow concentration and ebb dominance within mangrove creeks, a positive feedback occurs where mangroves lead to a self-scouring effect in creeks. The deepening of creeks in the presence of mangroves has been observed by Wolanski *et al.* (1980), Furukawa *et al.* (1997)**,** Wolanski & Ridd (1986) and van Maanen *et al*. (2015). In addition to favouring flow concentration, the dense root structures of mangroves also contribute to the stabilisation of channel banks (Wolanski *et al.*, 1980; van Maanen *et al*., 2015).

Using a numerical model, Wolanski *et al.* (1980) highlighted that it is the density of mangroves that influences both channel size and geometry. The model showed that when mangrove density was significantly reduced, the export of sediment from the system was considerably larger than the import. The model suggested that the channel would erode and channel meandering and braiding would be accelerated if there were not enough mangroves to stabilize the sediment. When mangrove density was significantly increased, the sediment export from the system was smaller than the import, leading to siltation and narrowing of the channel (Wolanski *et al.*, 1980).

The discussed literature shows that mangroves do influence physical processes, however many of the studies imply that the degree of influence is largely dependent on the density structure of the mangroves. Hence, not all mangrove systems will evolve the same way or exhibit that same level of stability and

resilience. For example, Winterwerp *et al.* (2013) showed that the density of mangrove forests is important for maintaining coastline stability. The study highlights the high sensitivity of mangrove systems when they become degraded and forest densities are reduced. In some situations a snowball effect can occur where the loss of mangrove forest fringe can lead to increased wave penetration within the forest. Subsequently, more erosion and less sedimentation may occur causing the water depth to increase. As water depth increases, waves can penetrate further landward and eventually all mangroves can be lost from the system if the tidal flats are removed by erosion (Winterwerp *et al.,* 2013). Regardless of mangrove forest fringe degradation, the effect of sea level rise and/or reduced sedimentation rates could have a similar effect on mangrove forests. The sensitive and dynamic nature of mangrove systems, emphasises why there is a need for better understanding of how the systems evolve and what factors will control their fate with future sea level rise and increasing anthropogenic pressure (Alongi, 2008; Temmerman, 2003; Swales *et al.,* 2015; Willemsen et al., 2016).

Understanding the hydrodynamics and sedimentation patterns within a system is the first critical step for determining how a system develops. However, it is important to note that for a more complete understanding of how a mangrove system evolves, there needs to be consideration of the two-way biophysical coupling that occurs. van Maanen *et al.* (2015) emphasises that the development of a system is not just dependant on the one-way biophysical coupling, where mangroves influence physical processes, but instead dependent on a complex two-way biophysical coupling. The concept of two-way biophysical coupling implies that mangroves influence flow and sedimentation patterns, but in turn, mangroves are influenced by the physical processes as they require certain salinity and inundation regimes; hence their distribution is a function of tidal flat elevation (van Mannen *et al.,* 2015; Mariotti & Fagherazzi, 2010).

CHAPTER THREE - FIELD DATA

3.1 Introduction

This research involved a month long field deployment within the Firth of Thames. One aim of the field deployment was to collect hydrodynamic data for numerical model calibration. Instruments were placed offshore for the purpose of calibrating the large scale model and boundary conditions, while instruments within the mangrove forest were placed with the intent of calibrating the nested, finer resolution model. The other aim of the field deployment was to provide a preliminary understanding of hydrodynamics within the Firth of Thames.

3.2 Field deployment

The field deployment was completed over 27 days between 5th May 2016 and 1st June 2016. This 27-day period insured that both a spring and neap tidal cycle was included. Ten pressure sensors were deployed along three cross-shore transects, each transect approximately two kilometres apart, in the section of mangroves between the Piako and the Waitakaruru rivers (Figure 3.1.B). The placement of pressure sensors within the mangrove forest was intended to capture cross-shore and long-shore gradients in water levels. One pressure sensor was deployed in the drainage creek at the back of the mangrove forest (W1). The drainage creek is located on the landward edge of the mangrove forest and flows in and out through the Piako River.

In the offshore region, three S4 current meters were deployed approximately 10 kilometres offshore from the mangrove forest (Figure 3.1.A). The current meters were deployed offshore to provide suitable data for the calibration of model boundary conditions. Attached to the current meter at S42 was a turbidity sensor, intended for measuring offshore suspended sediment concentrations. All instrument locations were recorded using GPS (Table 3.1).

Due to data logger malfunction, the Dobie (OBS) and an ISD pressure sensor failed to collect data during the deployment. Hence, for the rest of this thesis these two instruments are no longer discussed. An RBR *Concerto* CTD was deployed at the forest fringe from the 10th May 2016 to 12th May 2016 as part of another

research project (data provided by Julia Mullarney, University of Waikato). Subsequently, the RBR *Concerto* CTD data provided a suitable replacement for the Dobie (OBS).

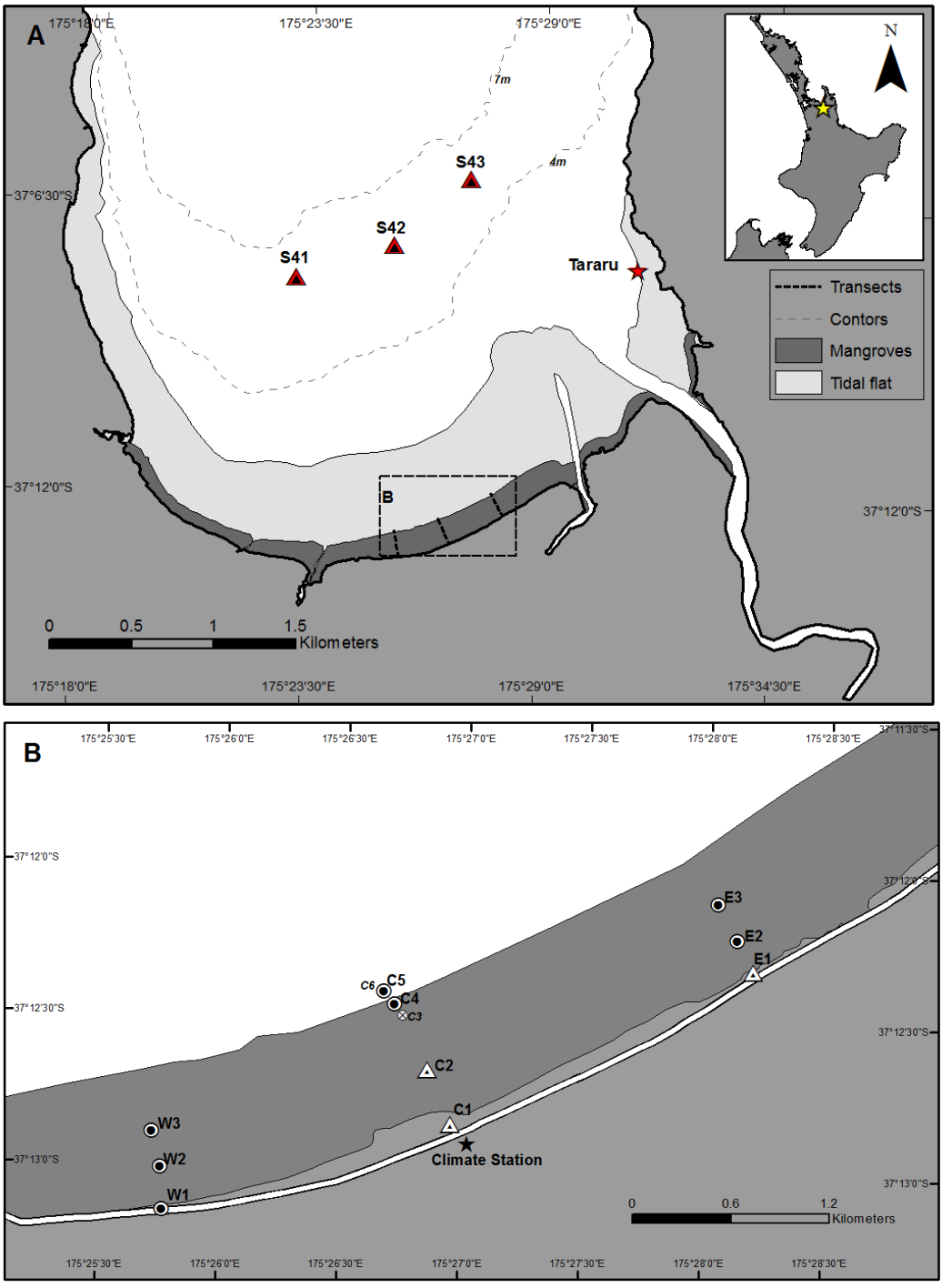

Figure 3. 1: Location of instruments deployed between 5th May and 1st June 2016, within the Firth of Thames. (A) Large scale study site with S4 locations. (B) Close up of instrument placement across the mangrove forest.

Table 3. 1: Site locations World Geodetic System 1984 (G1762).

Site Name	Instrument	Latitude	Longitude
W1	NIWA DOBIE	37°13'09.03"S	175°25'45.98"E
W2	NIWA DOBIE	37°13'00.48"S	175°25'45.32"E
W3	RBR *Duet*	37°12'53.40"S	175°25'43.14"E
C1	Solinst	37°12'50.68"S	175°26'57.17"E
C2	Solinst	37°12'40.01"S	175°26'51.18"E
C3	ISD	37°12'29.37"S	175°26'51.18"E
C4	ISD	37°12'27.30"S	175°26'42.68"E
C6	NIWA DOBIE (OBS)	37°12'24.51"S	175°26'40.42"E
C5	RBR *Concerto*	37°12'28.88"S	175°26'43.24"E
E1	Solinst	37°12'19.19"S	175°28'11.47"E
E2	NIWA DOBIE	37°12'13.09"S	175°28'07.39"E
E3	RBR *Duet*	37°12'05.90"S	175°28'02.38"E
S41	S4ADW	37°07'54.58"S	175°23'12.29"E
S42	S4ADW + SCUFA	37°07'16.56"S	175°25'30.06"E
S43	S4ADW	37°06'00.01"S	175°27'16.29"E
Tararu	Tararu tide gauge	37°07'38.23"S	175°31'14.87"E

3.2.1 Hydrodynamic loggers – principles and set up

RBR Duet and RBR Concerto C.T.D

The RBR Duet is a self-contained, autonomous, submersible tide and wave logger that records wave burst and tidal averaging. The two RBR *Duets* were deployed in the middle of the mangrove forest on the western and eastern transects (W3 & E3). Each RBR was firmly attached to an upright mangrove trunk, to ensure the pressure sensor was situated just above the sediment surface (Figure 3.2.A). The RBR were set to WAVE mode measuring pressure (dbar), water depth (m) and temperature (^{o}C). Burst averaged samples of 0.008Hz were logged every 10 minutes.

Solinst Levelogger Gold

The Solinst Levelogger Gold is an absolute (non-vented) pressure sensor which measures groundwater and surface water levels and temperature. Water levels are recorded as temperature compensated pressure readings, and can be barometrically compensated with the aid of a Barologger. Three Solinst were deployed within the mangrove forest, one in the middle of the centre transect (C2) and two at the back of the forest on the centre and eastern transects (C1 & E1). All Solinst were deployed below the ground surface in perforated PVC pipes wrapped

in geotextile fabric to avoid clogging (Figure 3.2.E). Solinst were attached to metal wiring which hung from the top of the pipe lid. All three Solinst were set to measure pressure every minute.

Barologger Gold

The Barologger Gold measures and logs changes in atmospheric pressure, which are then used to compensate water level readings recorded by a Levelogger or any other absolute pressure sensor. One Barologger was deployed inside a pelican case with the pressure sensor at location C3 (Figure 3.1.B).

ISD (Instruments Services & Developments) pressure sensors

The ISD pressure sensor measures pressure as a voltage so it was calibrated against water levels in the lab. The instrument is calibrated from 0 to 3 metre water depth. Samples were taken every 1 minute and 10 minute averages were recorded. Two ISD pressure sensors were deployed along the centre transect (C3 & C4).

NIWA DOBIE

The NIWA DOBIE is a wave gauge that measures water depths at 4Hz frequency for 10 minute bursts (Figure 3.2.A). Instrument output was given as 10 minute averaged measurements. Two DOBIE were placed within the mangrove forest (E2 & W2) and one was placed in the drainage creek (W1).

InterOcean Inc S4ADW

The InterOcean Inc S4ADW is an electromagnetic current meter that directly measures the true magnitude and direction of current motion in any water environment. Three S4ADWs were fixed to a steel frame 1 metre above the seabed (Figure 3.2.D) and measured water depths and current speed at 2Hz for 9 minute bursts every 20 minutes.

SCUFA Submersible Fluorometer

The SCUFA is a self-contained fluorometer that is able to measure fluorescence and turbidity simultaneously. It was deployed on the steel frame at location S42 and recorded turbidity measurements every 5 minutes. Due to insufficent battery life turbidity measurements were only recorded from the 5th May 2016 till the 18th

May 2016. The turbidity readings were calibrated in the lab against different sediment concentrations (Section 3.3.3).

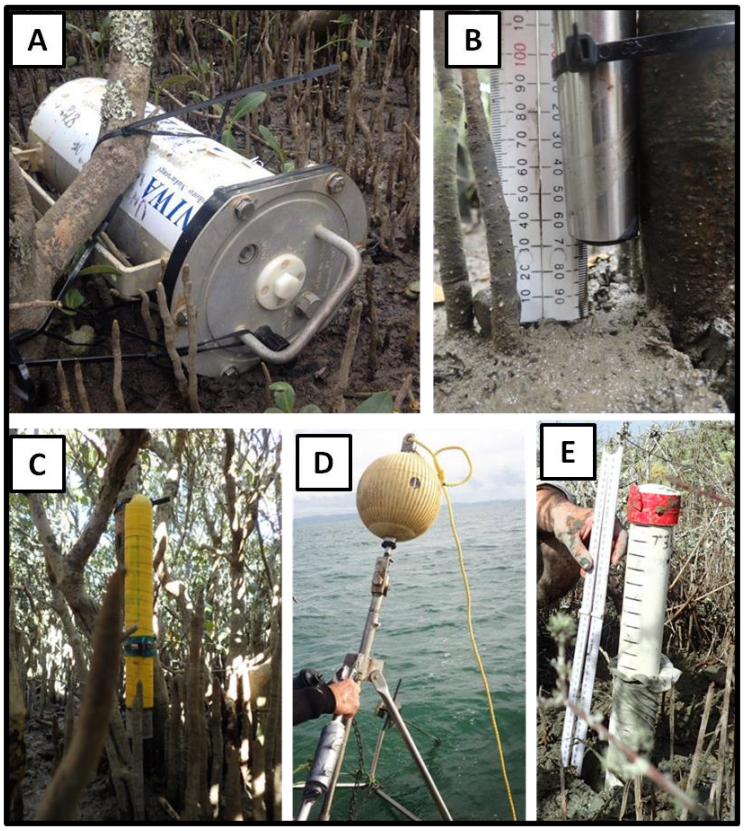

Figure 3. 2: Instruments used during the field deployment. (A) NIWA DOBIE (B) ISD pressure sensor (C) RBR *Duet* (D) InterOcean Inc S4ADW (E) Solinst Level Logger (inside PVC pipe).

3.2.2 Tararu Tide Gauge

The Tararu tide gauge (Figure 3.1) is a Waikato Regional Council monitoring site that has been recording water levels continuously since 1990. The 27 day period was downloaded for the Tararu tide gauge and used as extra data for model calibration (Figure 3.3).

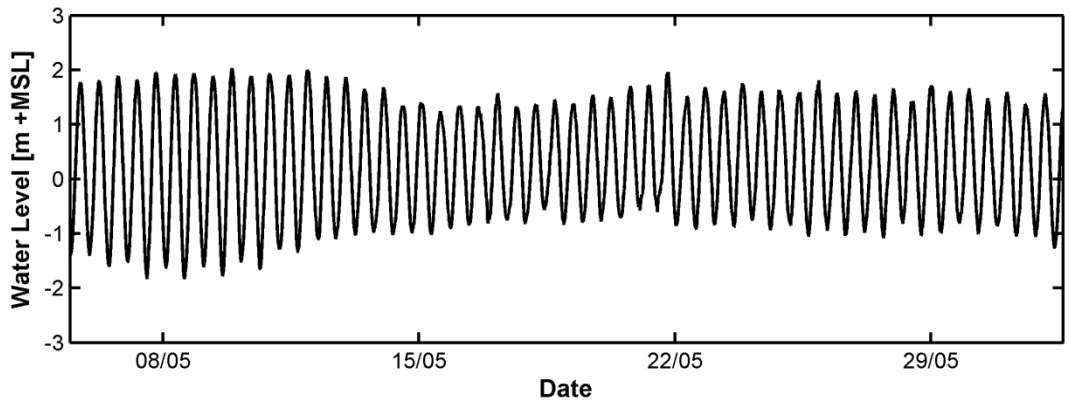

Figure 3. 3: Water levels at Tararu tide gauge between 5th May 2016 and 1st June 2016.

3.2.3 Climate station data

Measurements of mean hourly temperature, atmospheric pressure, rainfall and wind were also sourced from the NIWA Climate Station (Figure 3.4) (Firth of Thames Ews (C75241)) located south of the centre transect (37^{o} 21'52"S 175^{o} 45'03"E) (Figure 3.1).

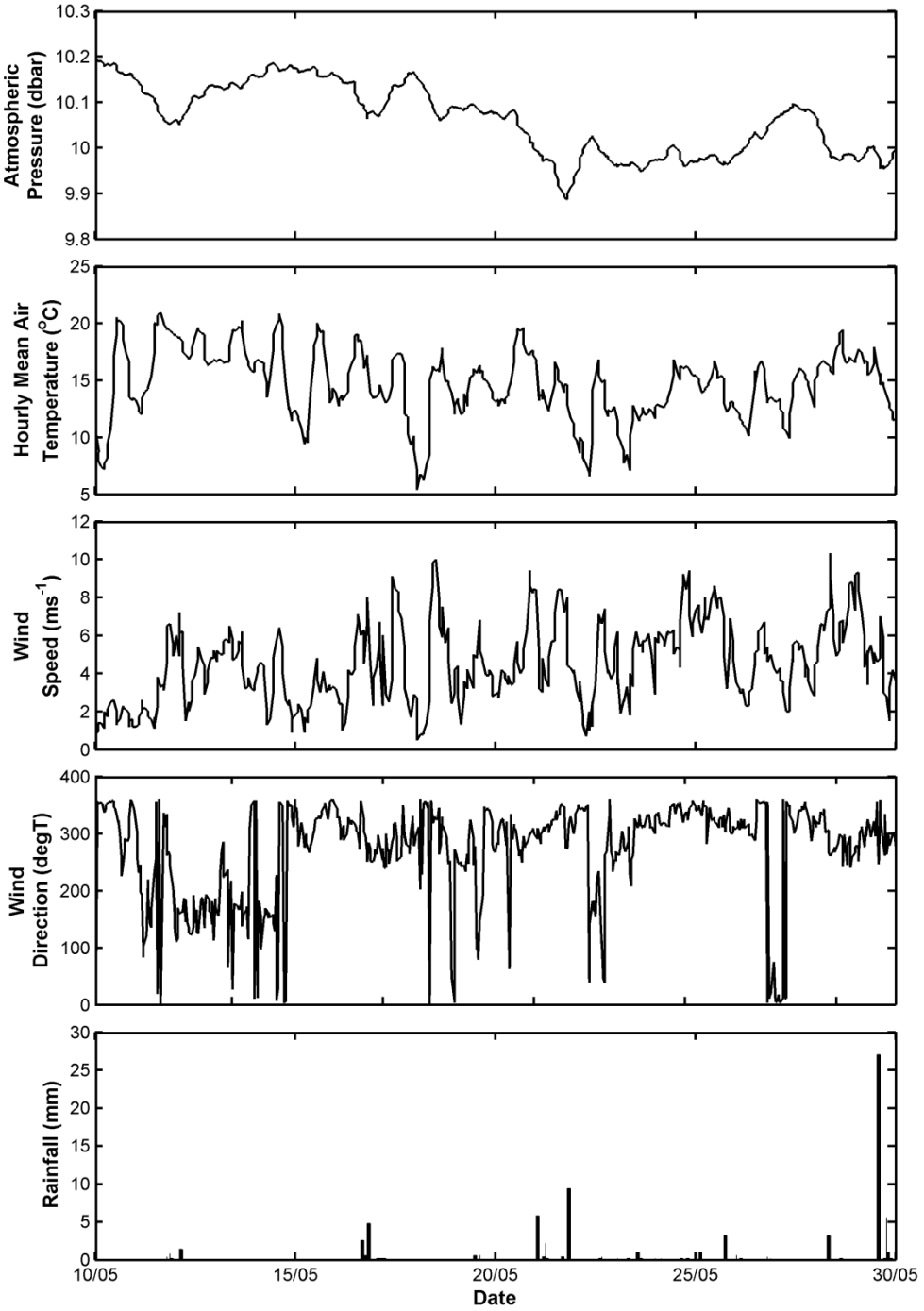

Figure 3. 4: Timeseries of all climate data measured by the NIWA Climate Station, including atmospheric pressure, air temperature, wind speed, wind direction and rainfall.

3.3 Data analysis

3.3.1 Calculating Water Levels

All pressure sensors within the mangrove forest, except the ISD, measured absolute pressure. Hence, the atmospheric pressure recorded by the Barologger was removed from all raw absolute pressure readings. For an accuracy check, the Barologger readings were compared with atmospheric pressure measured from the NIWA climate station (Figure 3.4.A) and the comparison showed an excellent match.

Equation 3.1 was used for calculating the water level relative to the local MSL vertical datum (Tararu 1952) (Z_{MSL}), where *s* is the distance from sensor to sediment, *e* is the sediment elevation relative to MSL, *p* is the water level above the pressure sensor, *h* is the sensor height relative to MSL (Equation 3.1) (Figure 3.5).

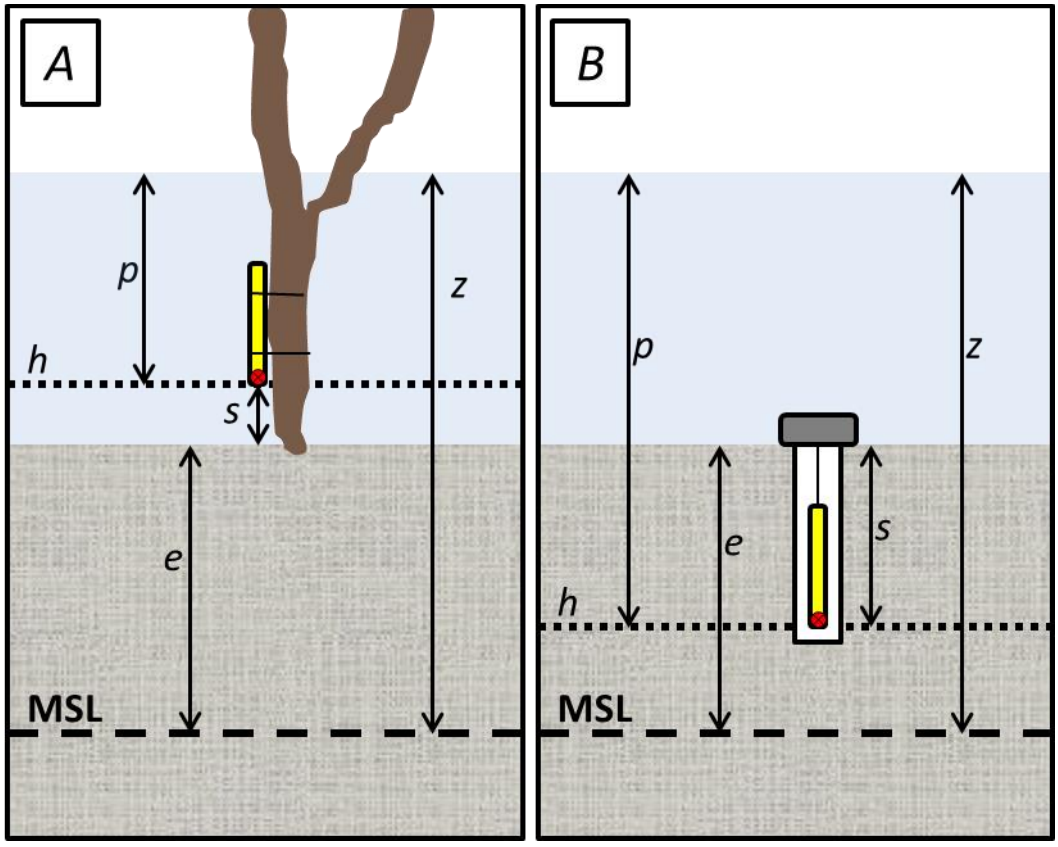

Figure 3. 5: Schematic diagram showing how water level relative to MSL was calculated from the pressure sensors that were deployed (A) above the surface and (B) within the ground. In panel B, the sensor height is negative, and in panel A, the sensor height is positive.

$$Z=p+h, \text{ where } h=e+s \quad \textbf{(3.1)}$$

3.3.2 Tidal Harmonic Analysis

Water levels measured by the three S4 current meters and the Tararu tide gauge were analysed using T_Tide. T_tide is a classical harmonic analysis script that extracts residual constituents and determines the major tidal constituents. The tidal harmonic analysis gives the frequency, period, amplitude and phase of up to 45 astronomical and 24 shallow water tidal constituents (Pawlowicz *et al.*, 2002).

3.3.3 Suspended Sediment Calibration

The turbidity measurements recorded by the SCUFA were converted to sediment concentrations using a calibration curve provided from a later deployment (November, 2016) of the same instrument using native sediment from the site (Figure 3.6). The calibration data was provided by Erik Horstman.

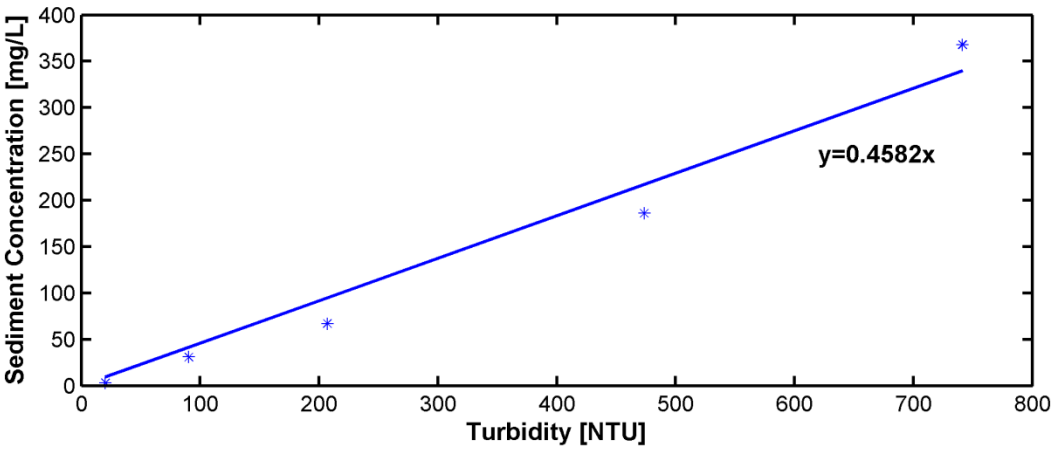

Figure 3. 6: Suspended sediment calibration results for the SCUFA (sourced from Erik Horstman).

3.4 Results

3.4.1 Offshore Tide

The major tidal constituent within the Firth of Thames is the principle lunar semi-diurnal, M2 tide (Table 3.2). The amplitude of the M2 tide is slightly larger along the sides of the Firth (S41 and Tararu) with a slight phase lag across the Firth from east to west (Table 3.3). There is also a phase lag between S43 and Tararu of approximately 13 minutes (Table 3.3). Mean high water spring (MHWS) levels are approximately 1.67 m above mean sea level whereas; mean high water neap (MHWN) levels are approximately 1.07 m (Table 3.4).

Table 3. 2: Amplitude (m) of principle harmonic components in the Firth of Thames.

Tidal Constituent	Period (hours)	Amplitude (meters)			
		S41	S42	S43	Tararu
M2	12.42	1.332	1.305	1.298	1.36
N2	12.66	0.317	0.313	0.310	0.28
S2	12.00	0.155	0.152	0.150	0.14
K1	23.93	0.064	0.062	0.062	0.059
O1	25.82	0.027	0.026	0.026	0.029

Table 3. 3: Phase of principle harmonic components in the Firth of Thames (phase is in Greenwich Mean Time (GMT)).

Tidal Constituent	Period (hours)	Phase (degrees)			
		S41	S42	S43	Tararu
M2	12.42	201.23	200.83	200.22	206.63
N2	12.66	252.16	252.04	251.44	269.15
S2	12.00	169.05	168.73	168.21	253.55
K1	23.93	151.73	151.80	151.30	146.04
O1	25.82	111.66	111.97	111.62	109.67

Table 3. 4: Mean high and low water levels for spring and neap tides (meters above MSL). Values calculated as average high and low water levels calculated from 12 spring cycles and 12 neap cycles.

Location	MHWS	MLWS	MHWN	MLWN
S41	1.713	-1.705	1.094	-1.097
S42	1.662	-1.649	1.070	-1.060
S43	1.657	-1.669	1.067	-1.060

3.4.2 Offshore Currents

Overall current velocities are greatest through the middle of the Firth and lowest along the western side (Table 3.5). All three S4 locations show overall flood dominance, however during some large spring tidal cycles, S41 shows slight ebb dominance (Figure 3.6). S43 has the lowest ebb current velocity (Table 3.6). Flood currents at S42 and S43 are predominately towards south/south-east and then rotate clockwise and flow towards north-west during the ebb tide. The circulation patterns at S41 differ, as it shows a rotation anti-clockwise (Figure 3.7 and Figure 3.8).

Table 3. 5: Maximum current velocities calculated for spring and neap tidal cycles.

	Spring		Neap	
Location	**Flood (m/s)**	**Ebb (m/s)**	**Flood (m/s)**	**Ebb (m/s)**
S41	0.307	0.001	0.276	0.004
S42	0.471	0.155	0.323	0.193
S43	0.491	0.188	0.353	0.170

During slack water (high and low tide) there is an offset from zero, indicating a residual current towards the south-west at S42 and S43 (Figure 3.7). The magnitude of the south-west current is greatest at S42. The same circulation patterns occur at spring and neap tides but the magnitude is smaller during neap tides. During neap tides at S41 the flood and ebb currents follow similar paths, however during spring tides there is more variability (Figure 3.7).

A comparison between the wind direction and residual current direction shows no significant relationship (Figure 3.8). Wind speeds during the deployment were low with the maximum wind speed being 10m/s (Figure 3.8).

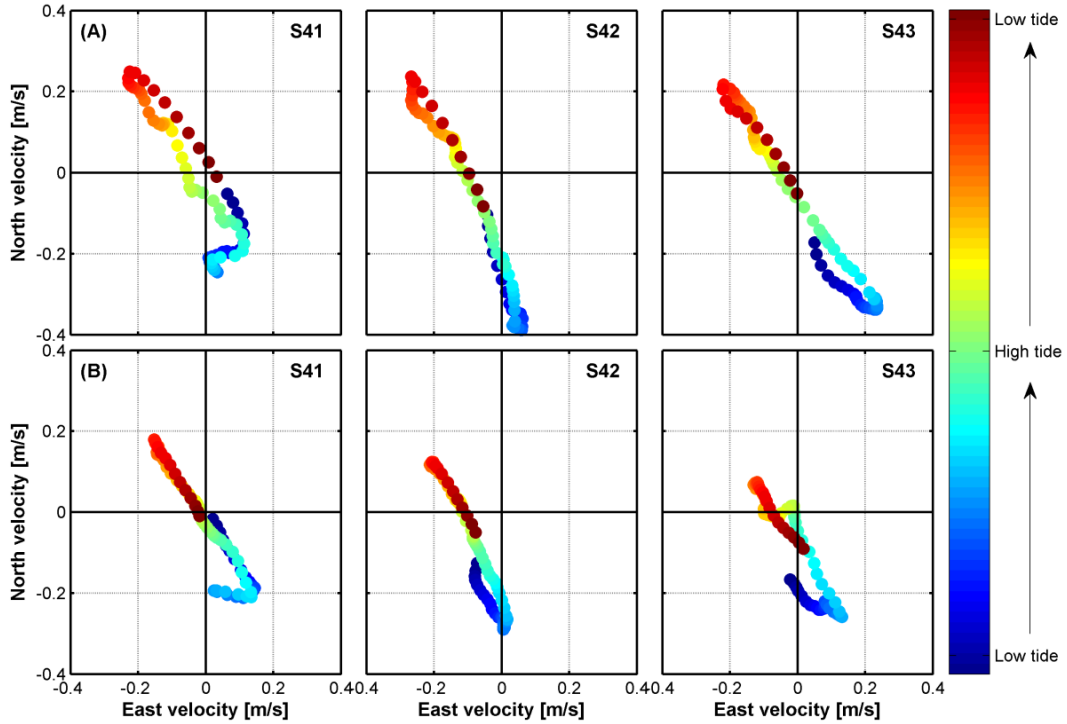

Figure 3. 7: North and east velocity components at each S4 current meter during a spring tide (A) and a neap tide (B).

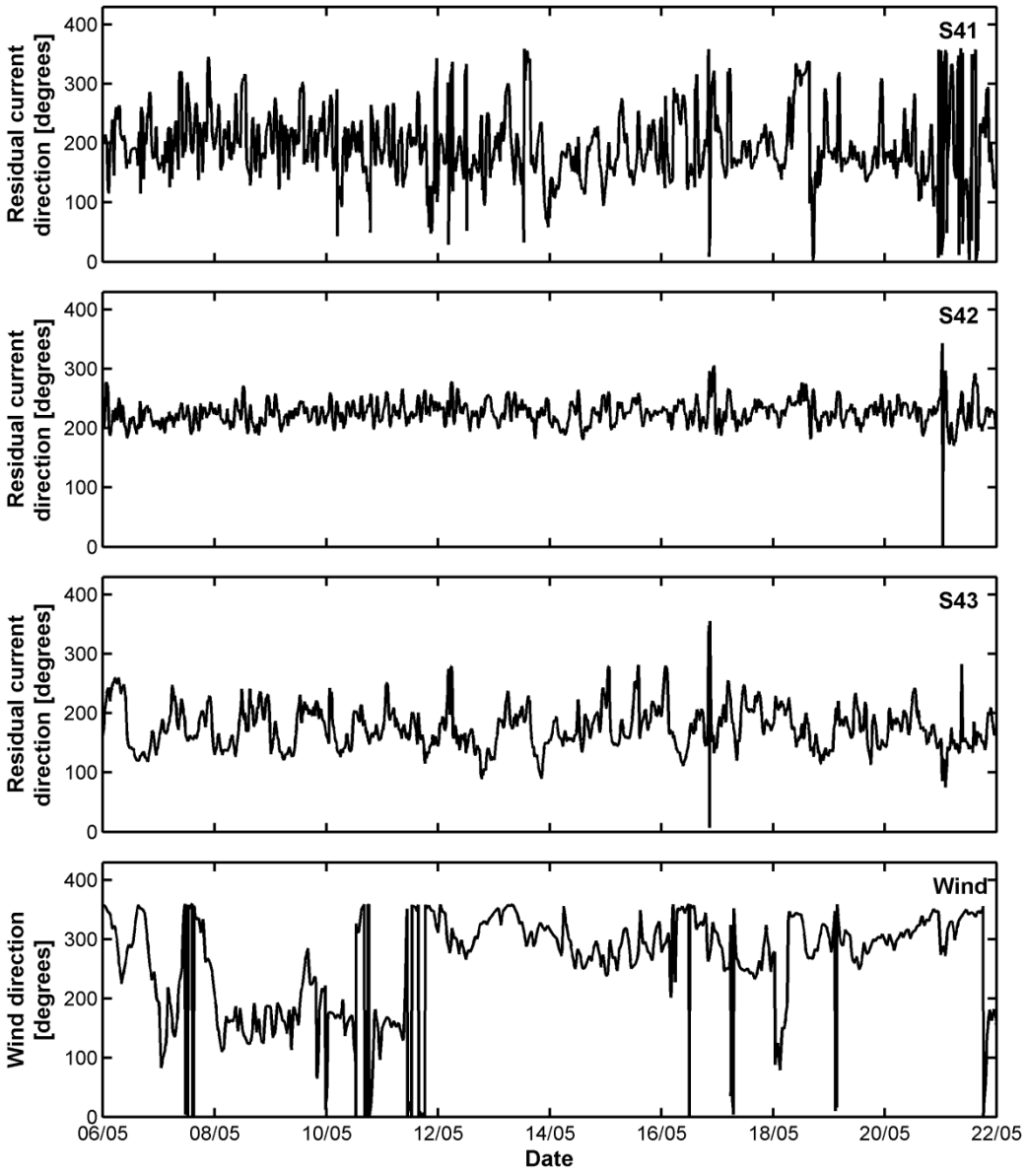

Figure 3. 8: Residual current directions calculated using T_Tide for the three offshore current meters, plus the wind direction measured from the NIWA climate station.

3.4.3 Offshore Suspended Sediment

During the spring tidal cycles at the beginning of the deployment, the offshore suspended sediment concentrations show a tidal cycle with 1 peak during the flood tide and another, slightly smaller peak at the end of the ebb tide. There appears to be several events, especially one around the 17th May that shows a large increase in suspended sediment concentrations. The explanation for these increases in suspended sediment concentration is not clear, as the timing does not coincide with rainfall or wind events (Figure 3.4).

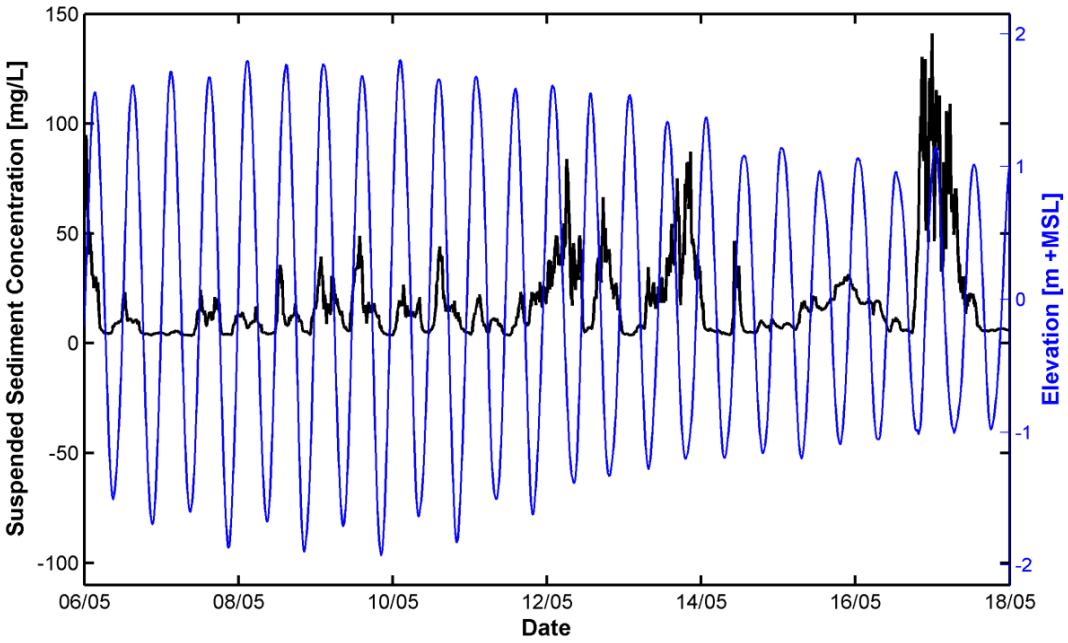

Figure 3. 9: Offshore suspended sediment concentrations (black line) with offshore water levels (blue line).

A detailed analysis of suspended sediment data was not included in this study. Understanding the hydrodynamics in the shallow vegetated areas proved more complex than expected. Also, very few publications on Delft3D models in such environments are available and so it was decided to focus on providing quality hydrodynamic predictions and use the suspended sediment data to provide context in the implications of the hydrodynamic results in the final thesis discussion (see Chapter 7).

3.4.4 Mangrove forest

3.4.4.1 Bed elevations

Elevation surveys were completed for all three transects using a Real Time Kinematic (RTK) global positioning system (GPS) which has an accuracy of 2 cm vertical and 1 cm horizontal. The elevation surveys show the tidal flat is relatively uniform in both the cross shore and long-shore directions. Most of the intertidal flat is between 1.45 and 1.68 m above MSL with a gradual slope from the forest fringe down to the tidal flat at approximately 0.50 m above MSL (Figure 3.10).

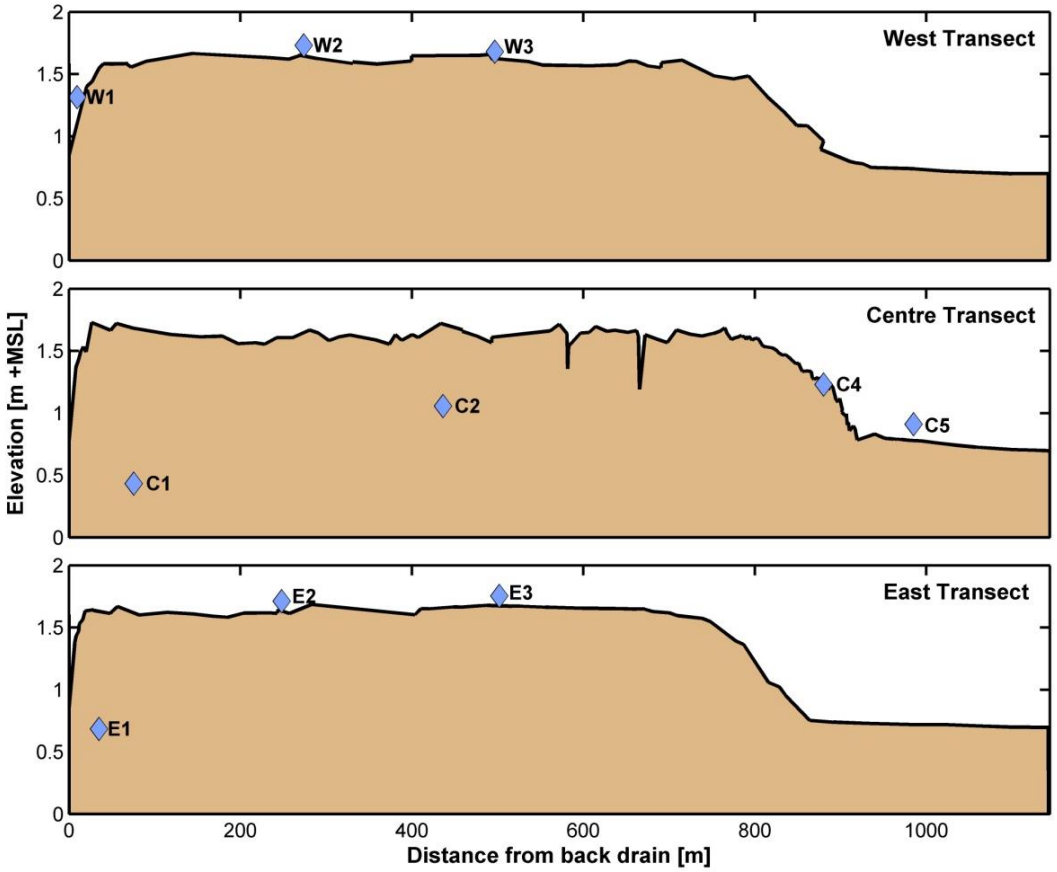

Figure 3. 10: Transect profiles surveyed by RTK GPS.

3.4.4.2 Tidal propagation

During maximum spring tidal cycles, all pressure sensors within the mangrove forest are inundated, except W2 (Figure 3.11). The degree of inundation during neap tides is less, with only C4, C2, W3 and E3 showing tidal inundation. The level of inundation at W3 and E3 is no more than 10 cm. E1 and C1 show small tidal signals in the groundwater, but water levels do not exceed the ground surface (Figure 3.11). Within the drainage creek behind the mangrove forest, W1 is inundated every tidal cycle. However, the water levels are slightly lower than water levels within the mangrove forest.

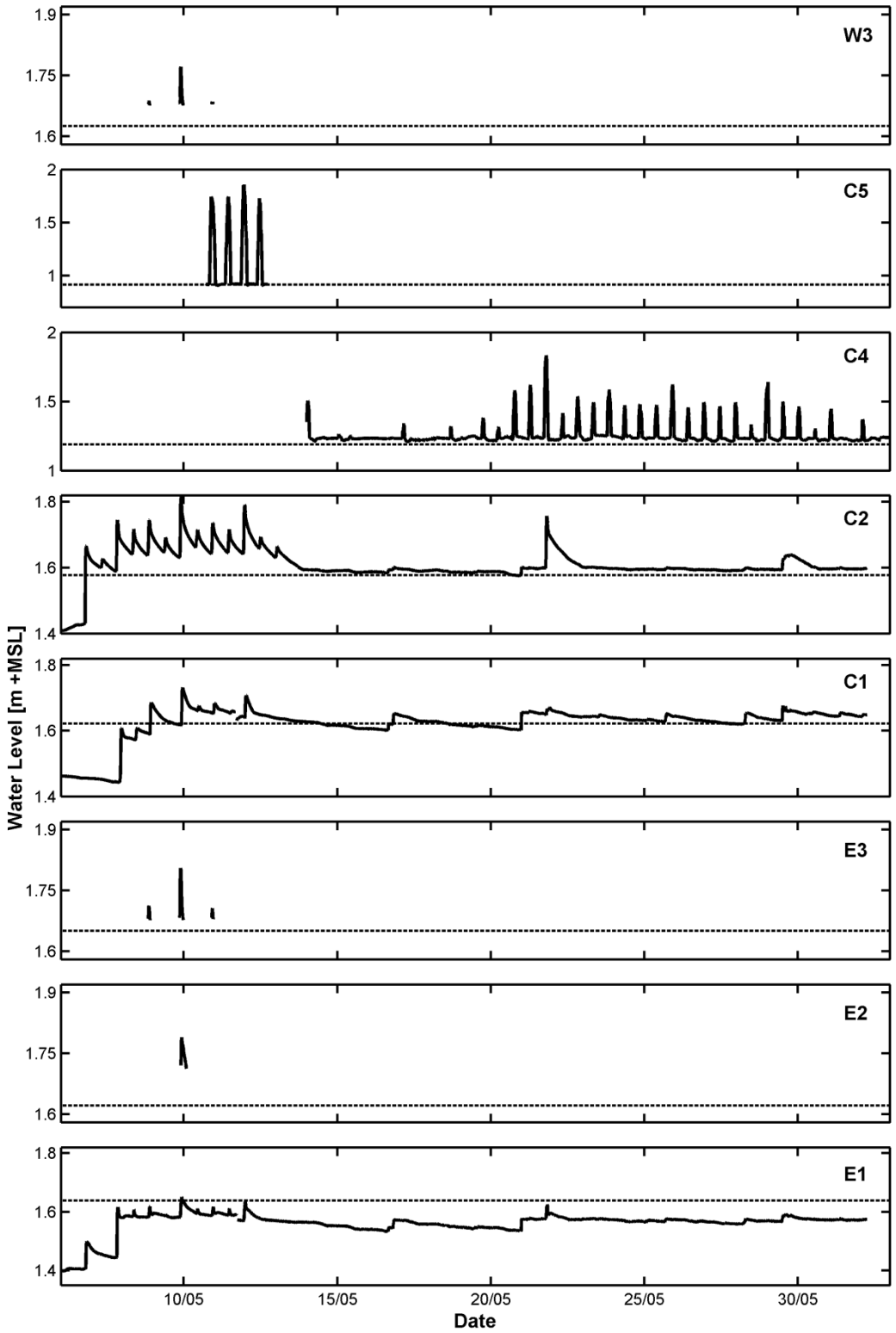

Figure 3. 11: Water levels measured throughout the mangrove forest between the 5th May and 1st June 2016. Dashed lines indicate the bed level at each pressure sensor.

The tidal amplitude in the offshore region (S42) is smaller than the tidal amplitude at the mangrove fringe (C4). However, with increasing distance landward within the mangrove forest, the tidal amplitude is reduced (Figure 3.12). For example,

the centre transect shows approximately 0.17 m reduction in the tidal amplitude over 440 m (Figure 3.12).

The shape of the tidal peak is near symmetric at the forest fringe but becomes increasingly asymmetric with distance landward. The asymmetry shows a slow, distorted ebb tide. After tidal inundation the groundwater levels do not always fall back to the same water level as the previous low tide, especially at C2 (Figure 3.12).

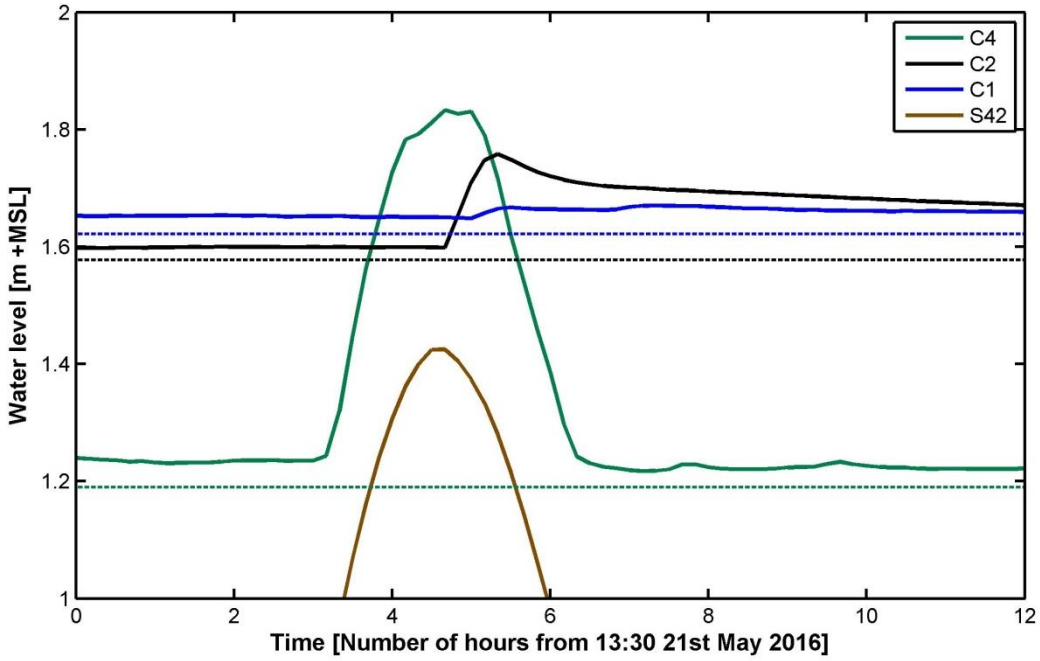

Figure 3.12: Water levels along the centre transect during the largest neap tide. Dashed lines indicate the bed level at each pressure sensor.

There is also a delay in the timing of tidal inundation throughout the forest. The tide arrives at C4 approximately 1 hour 40 minutes before it arrives 350 m further landward at C2 (Figure 3.12). In the longshore direction there is not a significant difference in the timing throughout the forest. For example, at W3 and E3 the tide arrives at the same time (Figure 3.13). However, there is a longshore variation in the phase of groundwater levels at the back of the forest (E1 is 1 hour 7 minutes before C1). There is also approximately a 40 minute delay from E1 and W1 (Figure 3.14).

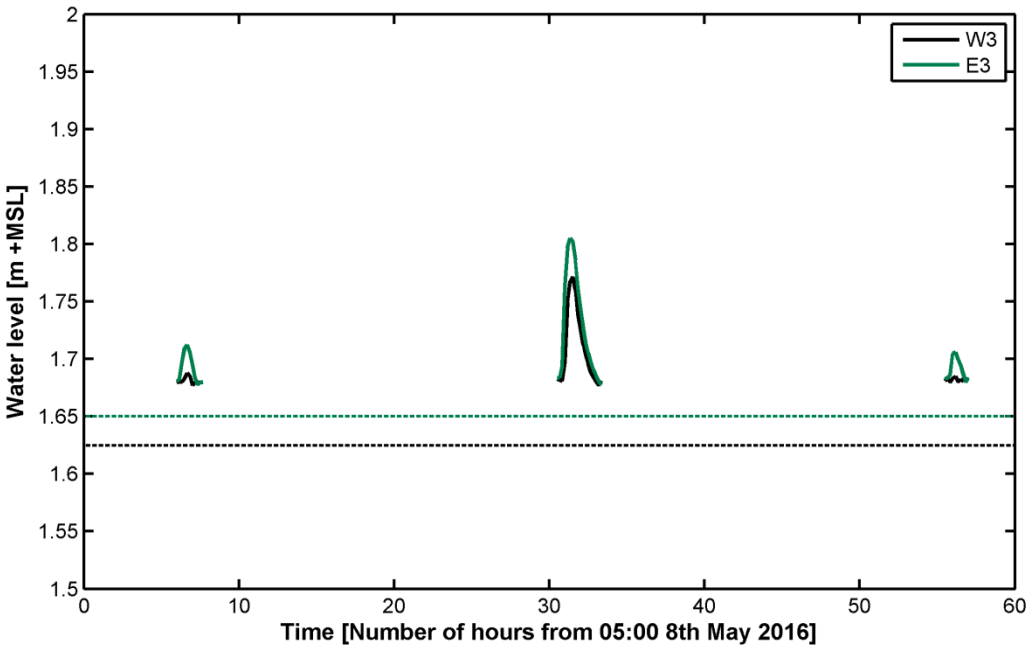

Figure 3. 13: Long-shore variations in water levels at W3 and E3. Dashed lines indicate the bed level at each pressure sensor.

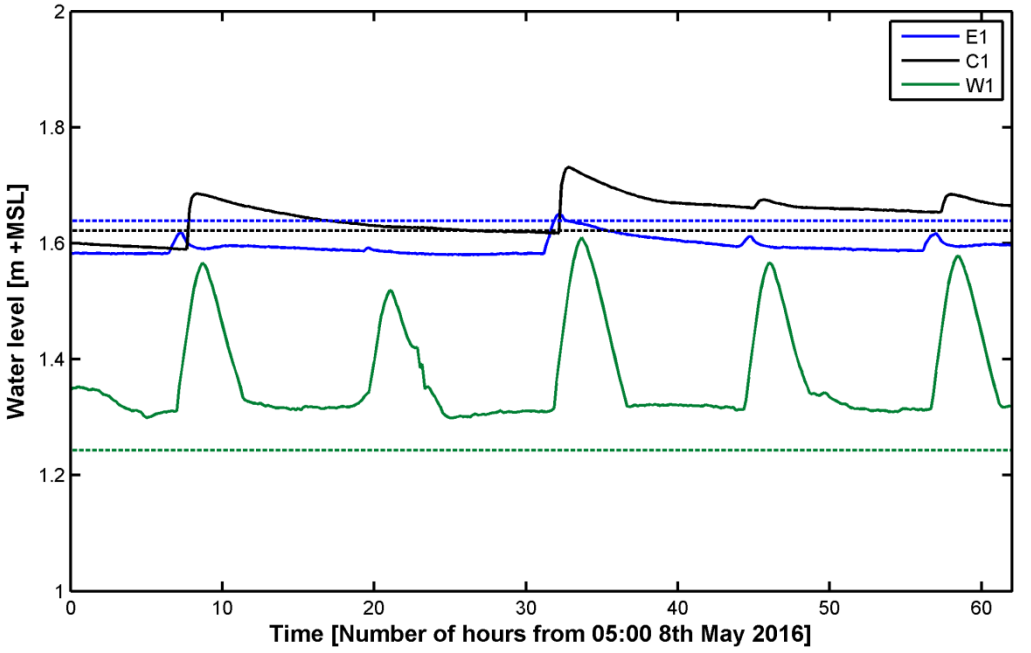

Figure 3. 14: Long-shore variation in water levels at the back of the mangrove forest (E1 & C1) and in the drainage creek (W1). Dashed lines indicate the bed level at each pressure sensor.

Water levels within the mangrove forest compared with water levels in the offshore region show different variations throughout the spring/neap cycle (Figure 3.15). On initial spring high tides, there is no tidal signal within the mangrove forest. However halfway through the spring cycle, tidal water level variation becomes evident within the mangrove forest and the water level eventually

becomes higher than the concurrent water levels in the offshore region. As the amplitudes of spring tides start to decline the tidal water level variations eventually diminish within the forest (Figure 3.15).

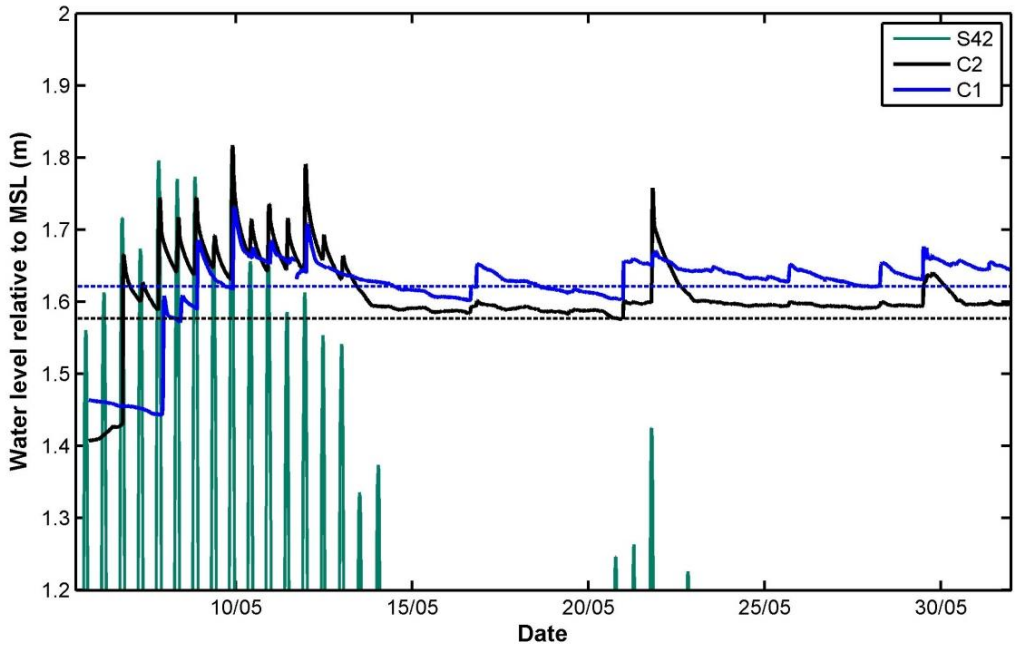

Figure 3. 15: Water level variations offshore and within mangrove forest. Dashed lines indicate the bed level at each pressure sensor within the forest.

3.5 Discussion

3.5.1 Offshore region

The fundamental tidal constituent forcing the tide within the Firth of Thames is the semidiurnal M2 tide (Table 4.1). The M2 tide is the most dominant constituent around the New Zealand coastline causing a rise and fall of sea level twice daily. The amplitude and phase extracted from T_TIDE harmonic analysis is consistent with values modelled by Walters *et al.* (2001).

When tidal constituents interact with differing bathymetry, tidal asymmetry can arise. Tidal asymmetry is where there is a difference in the magnitude of flood and ebb currents. Flood (ebb) dominance occurs when the flood (ebb) current is shorter duration and faster velocity than the ebb (flood) current (Speer & Aubrey, 1985). The large amplitude relative to channel depth within the Firth could partially explain the overall flood dominance measured by the S4 current meters (Aubrey & Speer, 1985).

Several aspects in the S4 data suggest that there is large scale clockwise circulation within the Firth of Thames. Firstly, the small phase lag shows the tide arriving on the eastern side (S43) before the western side (S41) of the Firth (Table 3.3). Secondly, the velocity vectors at S42 and S43 show the tide rotating clockwise. In addition, the residual currents at S42 and S43 are predominantly towards the south-west (Figure 3.8).

Stephens (2003) indicates circulation in the outer Firth of Thames is driven by the large scale effect of Coriolis forces deflecting currents to the left and causing stronger flood tides on the eastern side and stronger ebb tides on the western side of the Firth. Although this phenomenon is more applicable for the outer Firth, it could partly explain why the eastern side has greater flood dominance compared to the western side (Figure 3.7).

It is possible that the discharge from the Waihou River could influence some of the circulation patterns, in particular on the eastern side of the Firth. However, the relatively low ebb velocities at S43 indicate that contribution to large scale circulation from river flow is minimal (Table 3.5).

Wind stress is another factor that can influence circulation patterns. Stephens (2003) found that strong winds can modify tidal flows. Nonetheless, during this field deployment the surface wind measured at the NIWA climate station did not exceed $10ms^{-1}$. In addition, the comparison between residual current direction and wind direction indicates that there was no significant relationship (Figure 3.8). However, if winds were stronger different circulation patterns may occur.

S41 on the western side of the Firth is showing flood dominance during some tidal cycles and ebb dominance during other tidal cycles. Also during some tidal cycles the velocities at S41 show rotation anti-clockwise (Figure 3.7). The possibility of two opposing circulation patterns on either side of the Firth is plausible, looking at colouration of satellite imagery (Figure 3.16). Opposing circulation patterns would also explain why the current direction and strength at S41 is so variable (Figure 3.7). Given that there is no substantial river input on the western side and wind direction does not correlate with residual current direction, the circulation on the western side is most likely due to bathymetry.

Figure 3. 16: Satellite imagery of the Firth of Thames. Image sourced by NASA's Terra satellite on 23 October 2002 (Wikipedia).

3.5.2 Mangrove forest

The shape of the mangrove intertidal flat is relatively flat and homogeneous, lacking tidal creeks. Given that the MHWN (Mean High Water Neap) is approximately 1.07 m above MSL (Table 3.4) and the mean tidal flat elevation is 1.55 m, it is no surprise that only half of the pressure sensors were inundated during neap tides.

The increase in tidal amplitude from S42 to C4 and C5 indicates that the tidal wave shoals as it propagates across the shallow intertidal flat (van Rijn, 2010). The decrease in tidal amplitude with distance landward within the forest is most likely due to the combined effect of drag induced by mangrove trunks, roots and bottom friction (Figure 3.12) (Li *et al.*, 2012; Massel *et al.*, 1999). The effect of high drag not only dampens the amplitude of a wave but it can also influence the phase (Li *et al.*, 2012). Hence, there is a delay in the arrival time of the tide, cross-shore within the mangroves (Figure 3.12).

Since groundwater levels show tidal signals that do not always exceed the ground surface, it is likely that the back of the mangrove forest only becomes inundated through the groundwater table instead of tidal propagation from the front of the forest. The most likely path for the tide to flow into the groundwater system is up the Piako River, along the back drainage creek and into the groundwater table. Hence, the tide arrives at E1 before it arrives at C1 and W1 (Figure 3.14). The considerable delay between E1 and W1 is probably due to friction induced by the low permeable sediment above the groundwater table (Figure 3.14).

The change of shape in the tidal peak between the forest fringe and inside the forest is also most likely due to the presence of mangroves. At the forest fringe the duration of flood and ebb tides are close to equal. However, inside the forest the ebb current becomes distorted with a long drainage time. This shape is characteristic of a high resistant environment (Lessa & Masselink, 1995).

The distorted drainage creates water level and phase differences between the mangrove forest and the offshore tide. For example, on initial spring high tides, the mangroves still need to get saturated and the groundwater levels gradually increase. Consequently, tidal signals in the back of the forest are attenuated compared to the offshore tides. As the spring cycle progresses, the groundwater

levels increase and water levels within the forest and offshore take a while to become equal. However, the groundwater is not able to drain as fast as the tide does and the tide starts flooding back in while the water levels in the mangroves are still dropping. Subsequently, there is an increase in water level within the mangroves compared to the offshore tides. Nevertheless, this effect gradually attenuates, as more and more of the water stored in the mangroves drains during the low tides and eventually there is no tidal signal within the forest during neap tides (Figure 3.15). Lessa & Masselink (1995) observed similar patterns within another mangrove system. They attributed impaired drainage during the ebb tide and perched water levels to the shallow water depth and presence of mangroves on the intertidal flats.

3.6 Conclusions

Field results provide sufficient data for a preliminary understanding of hydrodynamics within the Firth of Thames. The high resistance environment within the mangrove forest appears to cause a reduction in tidal amplitude and phase. Subsequently, during spring tides there are phase lags and water level gradients between the mangrove tidal flats and the offshore tide. Previous studies indicate that these water level gradients can significantly alter tidal asymmetry. The field data collected provides suitable data to calibrate the hydrodynamic model so that it can be explored further as to whether or not it is the mangroves altering the hydrodynamics within the Firth of Thames.

CHAPTER FOUR - NUMERICAL MODEL SETUP

4.1 Introduction

Numerical modelling is an effective and highly-used method for understanding large scale hydrodynamic processes. Through using different model configurations and forcing, hydrodynamic models can be used to solve a wide range of coastal phenomena. The benefit of process-based numerical models is that they allow processes and elements to be isolated which helps with determining specific interactions. However, the generation of accurate numerical models can be difficult and limitations in true representation are inevitable. The validity of a numerical model is limited by the number of processes considered and by the simplifications adopted to describe them (Mariotti & Fagherazzi, 2013). This chapter describes the setup of the Delft3D numerical model used to generate the hydrodynamics within the Firth of Thames.

4.2 Delft3D Module and Main Equations

Delft3D is numerical modelling software that simulates flow hydrodynamics, sediment dynamics and morphological processes in shallow water environments. The Delft3D - FLOW module computes flow based on finite differenced, nonlinear, shallow water equations in two (depth-averaged) or three dimensions. The system of equations consists of the horizontal momentum equations, the hydrostatic pressure relation (vertical accelerations are assumed to be small compared to gravitational acceleration), the continuity equation, the transport equation, and a turbulence closure model (Lesser, 2004). The discretization of shallow water equations is achieved using a staggered grid pattern, where water level points are defined in the centre of a cell and velocity components are defined on the cell edges. Grid structures can be cartesian rectangular, orthogonal curvilinear (boundary fitted), or spherical (Lesser, 2004).

4.3 Model Domain/Grids

The total model domain covers the southern section of the Firth of Thames, extending approximately 19 km offshore from the southern coastline, and includes the most seaward limit of the Waihou, Piako and Waitakaruru Rivers. For minimised computational cost, a two dimensional (depth-averaged), cartesian, curvilinear grid was developed for horizontal model discretization. To further improve computational cost while increasing resolution, a nested curvilinear grid was implemented for the mangrove intertidal flats.

The overall computational grid has a coarse resolution ranging from 150 x 100 m to 300 x 300 m. An open boundary was defined across the northern side of the grid and three open boundaries were also defined at the upstream limit of each river. The grid extends 15 km upstream of the Waihou River to cover the full distance of tidal influence.

The nested computational grid has a finer resolution ranging from 30 x 30 m to 55 x 55 m, covering the mangrove intertidal flats and extending 8 km offshore to include the Waihou River plume (Figure 4.1).

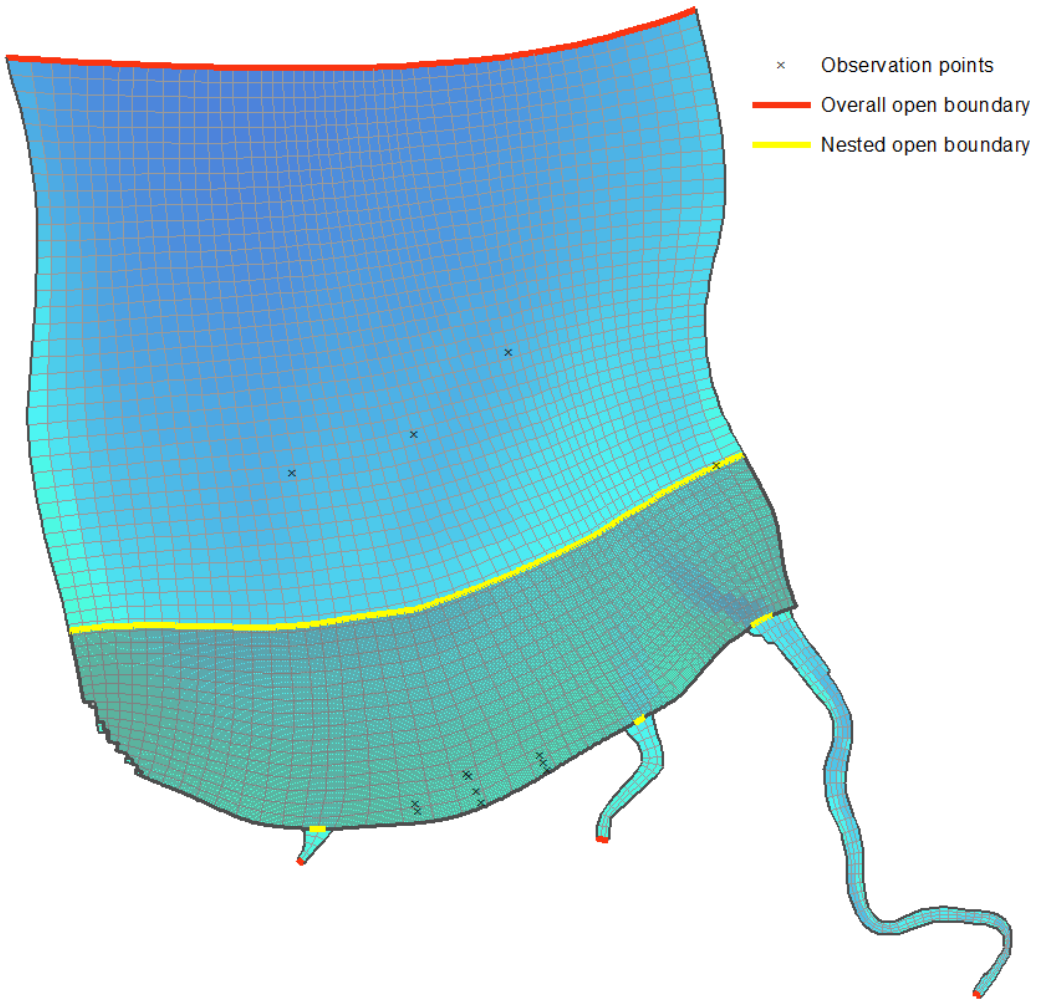

Figure 4. 1: Overall and nested model domains including locations of open boundaries.

4.4 Bathymetry development

Bathymetry is one of the most critical inputs for accurate numerical modelling. The Delft3D - QUICKIN module was used to generate bathymetry for the computational grid. QUICKIN coverts depth samples into a depth file using triangulation interpolation, grid cell averaging and internal diffusion. Depth samples were obtained from several sources (Figure 4.2). The offshore region was derived from the 1978 hydrographic chart (Figure 4.2.D). The Waihou and Piako River depths were interpolated using 2011 multiple single beam echo-sounder surveys sourced from the Waikato Regional Council (Figure 4.2.A & Figure 4.2.C). The 2011 Waihou River delta survey was also sourced from Waikato Regional Council (Figure 4.2.B).

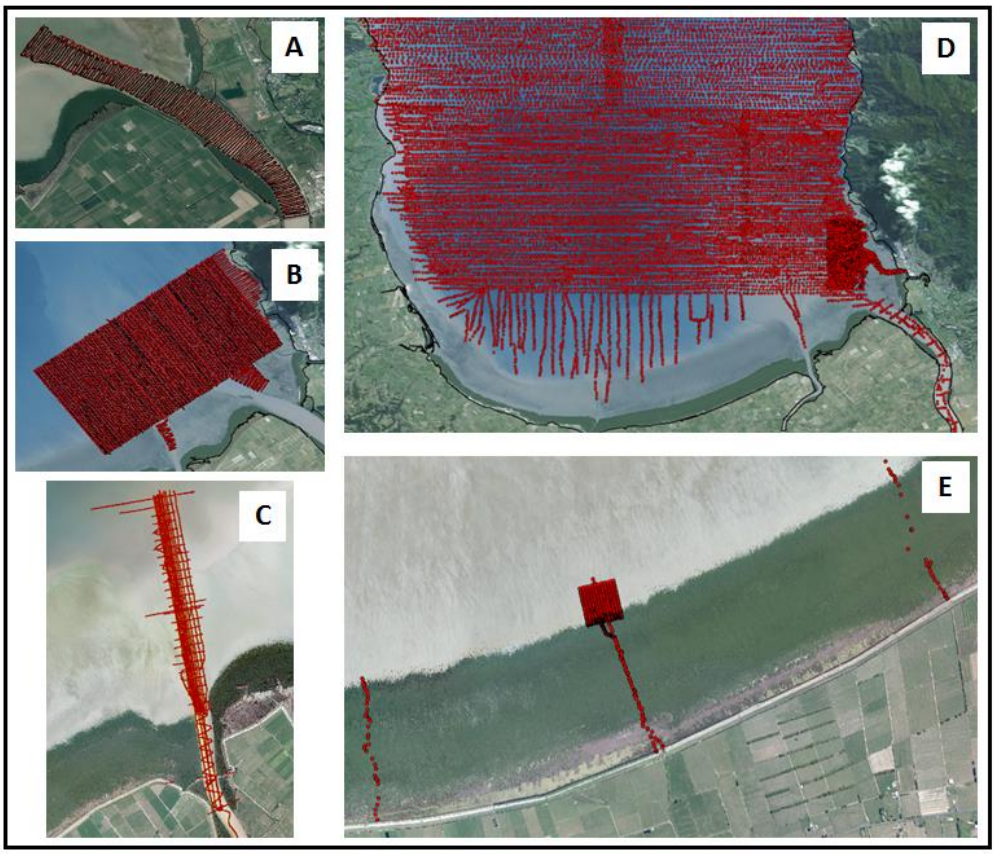

Figure 4. 2: Sample points used for model bathymetry development. (A) Waihou River 2011 Survey, (B) Waihou River Delta 2011 survey (Waikato Regional Council/ASR Ltd report, 2011). (C) Piako River Survey 2011 (Waikato Regional Council). (D) Hydrographic chart (1978). (E) RTK GPS transect surveys collected here (2016), plus Balke *et al.*, 2015 tidal flat survey (2016).

For a small portion of the mangrove intertidal flats, RTK GPS surveys were available. These surveys include the 3 transects measured during the 2016 field deployment and the 2013 tidal flat survey measured by Balke *et al.* (2015) (Figure 4.2.E). For the remainder of the mangrove intertidal flat area, a 2012 LiDAR dataset was considered for bathymetry; however, there was uncertainty in the LiDAR points due to the variable interference of radar from the vegetation canopy. An alternative method for generating the remainder of the mangrove intertidal flat bathymetry involved image analysis.

Image analysis was completed based on the observation that taller tree heights tend to occur where ground elevation is slightly higher and shorter tree heights tend to correlate with slightly lower ground elevations (Swales *et al.*, 2015). Image analysis firstly involved establishing RGB thresholds to distinguish between the dark and light coloured vegetation in aerial images (Figure 4.3). Comparison between field observation and aerial imagery confirmed that the dark

and light colours across the mangrove forest, represent short shrubby mangroves (0.5 - 1.5 m high) and tall mangroves (1.5 - 3 m high), respectively. Subsequently, in regions of dark coloured vegetation (short tree height) the ground elevation was assumed to be on average 1.55 m above MSL. Likewise, in regions of light vegetation (tall tree height) the ground elevation was assumed to be on average 1.67 m above MSL. To convert all elevation points to depth values, every elevation was multiplied by -1. All bathymetric data was converted to depth values relative to local MSL (Tararu 1952).

Although the image analysis method provides some uncertainty in the bathymetry across the intertidal flat, the derived bed elevations were compared with the bed elevations measured by the RTK GPS surveys and the MAE (mean absolute error) was 0.032 m.

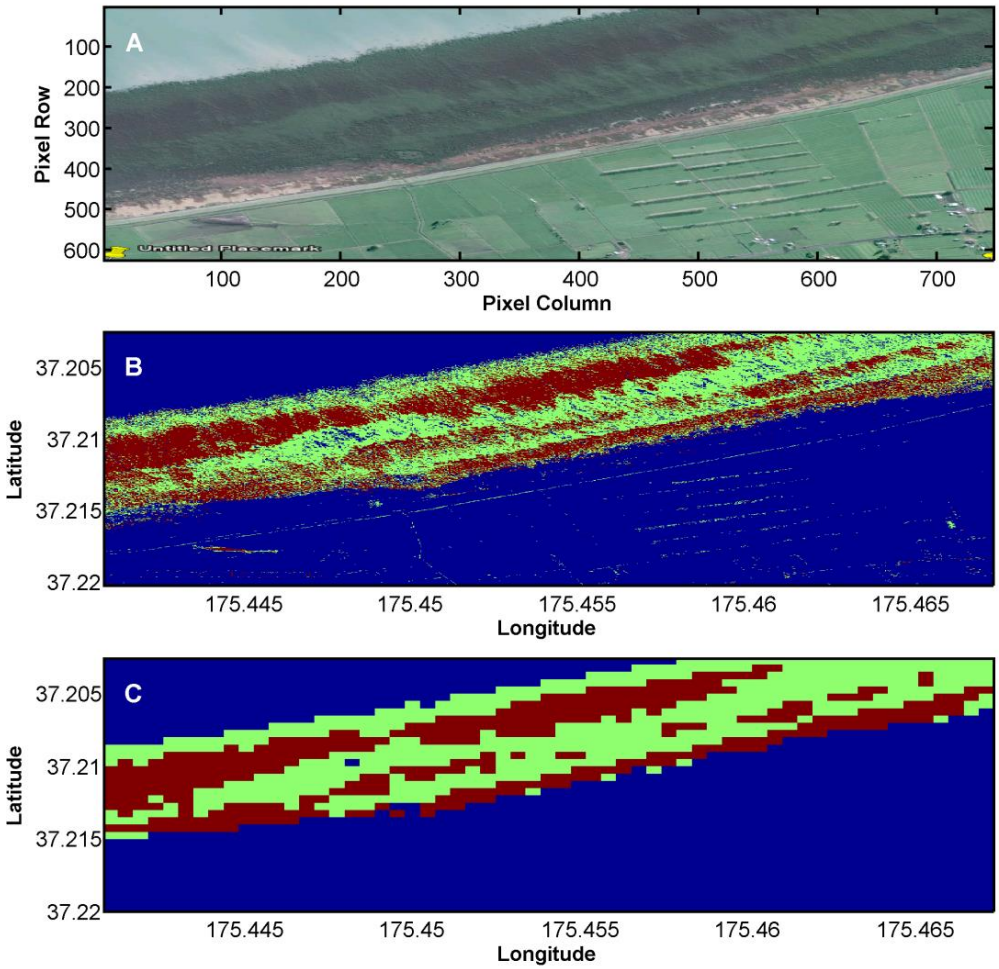

Figure 4. 3: (A) Aerial imagery (sourced from GoogleEarth). (B) RGB classification for dark (red) and light (green) coloured vegetation. (C) RGB classification gridded onto 120 meter resolution.

4.5 Simulation Period

The overall model was simulated from the 00:00:00 4th May 2016 to 00:00:00 24th May 2016. This simulation period covers the same time period as the field deployment but also allows a one day period for the model to stabilize. A timestep of 0.05 minute (3 seconds) was used. Due to computational cost, the nested model was only simulated from the 00:00:00 8th May to 00:00:00 13th May. This simulation period covers the large spring tidal cycles and since the field results indicate that the tidal flat is not inundated during neap cycles, it was decided to focus mainly on simulating the spring tides.

4.6 Boundary conditions

Boundary conditions are one of the main parameters used to force simulations. Open boundaries represent the influence of the outer world on the flow within the modelled region. Flows can be forced using water levels, currents, water level gradients, discharges and the Riemann invariant. Along closed boundaries, the velocity component is set to zero.

4.6.1 Overall Model

The open sea boundary on the overall grid was forced with an astronomical water level boundary. A year's worth of water level outputs from NIWA's calibrated New Zealand EEZ tidal model (Walters *et al.*, 2001) was analysed, using T_TIDE to extract amplitude and phase from key tidal constituents at the location of the model's open sea boundary. To ensure any long-shore phase shifts were included, the amplitude and phase of key tidal constituents was extracted for 2 locations on either side of the Firth (Figure 4.4). T_TIDE outputs showed M2, N2 and S2 tidal constituents to be the most significant at the boundary, with a small phase difference between the western and eastern side (Table 4.1). To incorporate the small phase difference into the model, a west and an east component was defined on the outer edges of the open sea boundary and the phase and amplitude of intermediate points along the boundary were linearly interpolated.

Figure 4. 4: Location of outputs from the NIWA tidal model.

Table 4. 1: Principal tidal constituents within the Firth of Thames, extracted from the NIWA tide model using T_TIDE (phase is in Greenwich Mean Time (GMT).

Location	Amplitude (metres)			Phase (degrees)		
	M2	N2	S2	M2	N2	S2
West	1.306	0.261	0.176	202.21	170.47	278.14
East	1.325	0.264	0.178	200.64	169.44	276.74

The overall model was also forced with three total discharge boundaries within each river (Figure 4.1). Five minute timeseries of river discharge for the Waihou and Piako Rivers was sourced from the Waikato Regional Council (Figure 4.5). However, discharge measurements were recorded from gauging sites at least 30 km upstream from the river mouth, giving underestimates of river discharge at the model boundaries. Consequently, the average river discharges used to force the model were increased to 50 m^3/s for the Waihou River, 30 m^3/s for the Piako River and 15 m^3/s for the Waitakaruru River. These river discharges are similar to the values used by Green & Zeldis (2015).

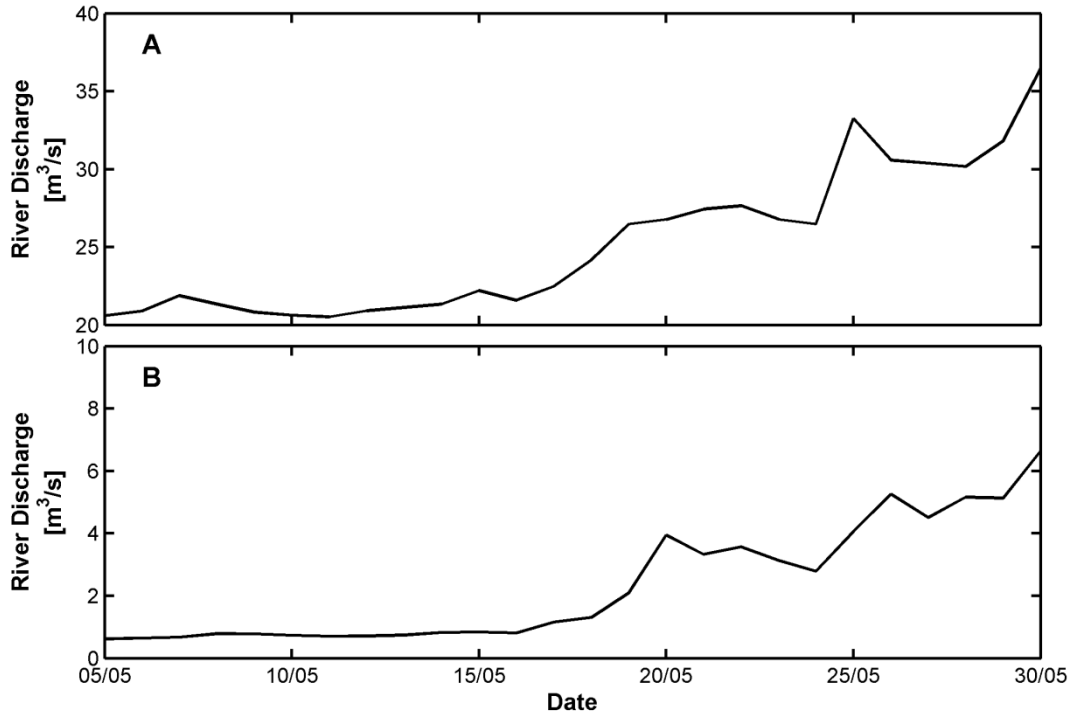

Figure 4. 5: River discharge for (A) Waihou River, measured at Te Aroha (B) Piako River measured at Paeroa-Tahuna Road Bridge.

4.6.2 Nested model

Delft3D -NESTHD1 and NESTHD2 were used to nest the fine resolution model within the overall coarse resolution model. The open boundaries of the nested model were forced by the outputs of the overall model.

4.7 Physical Parameters

Delft3D -FLOW incorporates several physical parameters describing the physical conditions in the model domain. The present numerical model includes bed roughness, eddy viscosity, wind and vegetation characteristics, but neglects waves and density differences. Bed roughness and eddy viscosity are so-called calibration parameters; hence their optimum values are determined in the calibration process (see Chapter 5). Hydrodynamic constants incorporated in the model include gravitational acceleration of 9.81 m/s^2 and water density of 1000 kg/m^3.

4.7.1 Bed Roughness

Bed roughness is a measure of the amount of frictional resistance imposed by the bed. Delft3D -FLOW has the option of several different bed roughness parameters

to represent the bed shear stress, including the Chezy, Manning and White-Colebrook friction coefficients. For the Firth of Thames model, the bottom roughness was computed based on Manning's coefficient ($s/m^{1/3}$) (Equation 4.1).

$$\text{Manning value} \qquad C = \sqrt[6]{h/n} \qquad \textbf{(4.1)}$$

Where, C is the Chezy coefficient, *h* is the water depth, and *n* is the Manning coefficient. With the Manning formulation, bottom friction dissipation has an additional inverse dependence on water depth. Estimates for Manning's coefficients typically range from 0.01 to 0.05 for smooth to rough bed surfaces. Optimum Manning values were determined through model calibration (see Chapter 5).

4.7.2 Horizontal Eddy Viscosity

Eddy viscosity is the transfer of momentum caused by turbulent eddies. In Delft3D –FLOW the 2D horizontal viscosity is assumed to comprise of two parts, molecular viscosity and 2D background viscosity. The 2D background horizontal viscosity (m^2/s) is a measure of the horizontal mixing that is not resolved by advection on the grid. Background horizontal viscosity values can be user-specified as a constant or space-varying parameter. The values of eddy viscosity depend on the flow and grid cell size. Typically, for grid sizes tens of metres or less, the eddy viscosity values are between 1 and 10 m^2/s. For grid sizes hundreds of metres or more the eddy viscosity is typically between 10 and 100 m^2/s (Deltares, 2014). Optimum viscosity values are discussed in Chapter 5.

4.7.1 Wind

Mean hourly wind data sourced from the NIWA Climate Station (Firth of Thames Ews (C75241) was applied to the model as a time varying wind file (.rgh), where surface wind direction and magnitude are taken into account (Figure 4.6).

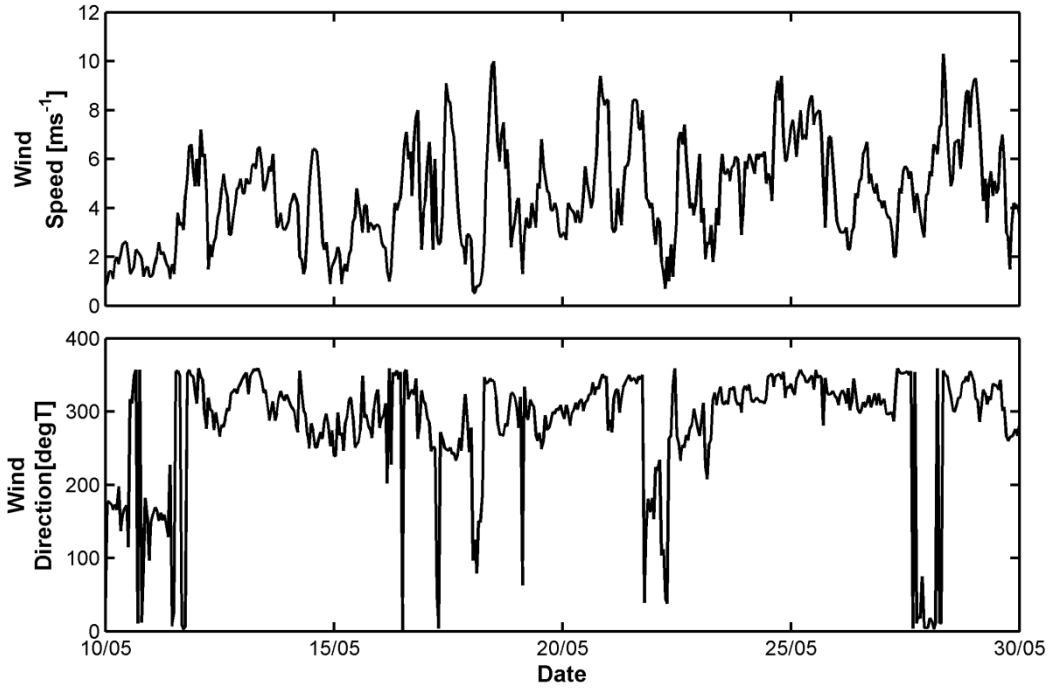

Figure 4. 6: Wind speed and direction sourced from the NIWA Climate Station and used to force the Delft3D model.

4.7.3 Vegetation Characteristics

In depth-averaged (2DH) models there are two different methods for representing vegetation characteristics. The simplified method involves adapting the Chezy roughness coefficient to increase drag (Baptist *et al.,* 2007). The other method is to use the trachytope approach. Trachytopes allow the user to specify flow resistance on a sub-grid level. At specified timesteps, the trachytopes are converted into a representative bed roughness. Vegetation flow resistance can specifically be represented by an area class trachytope which, for both submerged and emerged vegetation, is based on the equation established by Baptist (2005) (Equation. 4.2)

$$C = C_b + \frac{\sqrt{g}}{k} ln\left(\frac{h}{h_v}\right)\sqrt{1 + \frac{C_D \alpha h_v C_b^2}{2g}} \qquad \textbf{(4.2)}$$

Where α is the vegetation density (m^{-1}) ($\alpha=Nd$, where N is the number of stems per m^2 and d is the stem diameter), C_b is the Chezy bed roughness ($m^{1/2}/s$), C_D is the bulk drag coefficient (roughness of vegetation surface), g is gravity (m/s^2), k is alluvial roughness predictor, h is the water depth (m), h_v is the vegetation height (m) (Deltares, 2014).

Within the nested model, the mangroves across the intertidal flat were represented using the trachytope approach. The mangroves were represented by two different vegetation types, pneumatophores and trees. For each vegetation type, height (h_v) and vegetation density (α) were defined (Table 4.2). Height and density (stem diameter and number per m^2) were approximated based on field observations (Appendix I) and the findings from Young and Harvey (1996). The default cylindrical drag coefficient (C_D) was set to 1. The vegetation density was adjusted during calibration of the nested model (see Chapter 5).

4.8 Numerical parameters

Delft3D -FLOW uses a flooding and drying algorithm, which includes a grid cell in the computation when the water depth exceeds the threshold depth and excludes the cells when water depths fall below the threshold. For both the overall and nested model, the threshold depth was set to 0.01 m.

The numerical scheme used for solving the advective terms in the momentum equation was the flooding-scheme. The flooding-scheme is best used for rapidly varying depth averaged flows, for instance the inundation of dry land. Due to the minimal inundation observed over the tidal flats, this advective scheme was considered most appropriate.

4.9 Observation Points

Delft3D uses observation points to record the time-dependant behaviour of computed quantities at a specific location, representing an Eulerian viewpoint of model output. For calibration purposes, observation points within the overall model were located at all three S4 locations, the Tararu tide gauge and the Concerto location at the front of the mangrove forest. Within the nested model, observation points were located at the eight instrument locations within the mangrove forest (Figure 4.1).

CHAPTER FIVE - MODEL CALIBRATION

5.1 Introduction

The process of calibration involves systematic adjustment of model parameters and forcing so that the model outputs accurately reflect the real processes of interest. Calibration is necessary to provide confidence in model results. In this chapter, the calibration of the numerical model, including statistical assessment of the overall and nested model performance, are presented.

5.2 Overall Model Calibration

Calibration of the overall model was achieved by comparing 21 days (covering spring and neap tides) of measured data from the field sites S41, S42, S43, Tararu, and C5 (Figure 3.1), with model outputs from the corresponding observation points. Successful calibration of the model, so that a good fit was achieved at these five locations, helped to ensure that the conditions at the boundary of the nested model were represented accurately.

5.2.1 Calibration Parameters

For hydrodynamic simulations, typical calibration parameters include bed roughness and eddy viscosity (Table 5.1). For a series of simulation runs, a range of values for bed roughness and eddy viscosity were trialled until the values that produced minimum error were established. Bed roughness values (Manning's Coefficient) used for calibration ranged from 0.01 to 0.04 $s/m^{1/3}$. This range of values was determined based on values used in literature (Deltares, 2014; Li *et al.*, 2012; Wolanski *et al.,* 1990; Furukawa *et al.,* 1997).

Due to the overall grid cell size ranging from 150 to 300 metres, the eddy viscosity values used for calibration were between 10 and 100 m^2/s (Deltares, 2014).

Table 5. 1: Parameters and the range of values used for model calibration.

Parameter	Range of values used	Optimum value
Bottom Roughness ($s/m^{1/3}$)	0.01-0.05	0.02
Eddy Viscosity (m^2/s)	10-100	10

*changes in eddy viscosity did not alter the model output.

5.2.2 Statistics Qualification

For an objective evaluation of model performance, this study uses three statistical parameters, mean error (ME), root mean-squared error (RMSE) and relative mean absolute error (RMAE) (Table 5.2).

Table 5. 2: Statistical parameters used for model calibration.

Parameter	Equation
Mean error (ME)	$\frac{1}{N}\sum_{i=1}^{N}(y_i - x_i)$
Root mean-squared error (RMSE)	$\sqrt{\frac{1}{N}\sum_{i=1}^{N}(y_i - x_i)^2}$
Relative mean absolute error (RMAE)	$\frac{\frac{1}{N}\sum_{i=1}^{N}\lvert y_i - x_i\rvert}{\frac{1}{N}\sum_{i=1}^{N}\lvert x_i\rvert}$
Wave Height RMAE (van Rijn et al., 2003)	$\frac{\lvert H_y - H_x\rvert - \Delta H_x}{H_x}$
Current Velocity RMAE (van Rijn et al., 2003)	$\frac{\lvert V_y - V_x\rvert - \Delta V_x}{V_x}$

The ME is the mean of the differences between modelled (*Y)* and observed (*X)* values. A positive (negative) ME indicates that the model results on average overestimate (underestimate) the measured data. The RMSE is one of the most common measurements of model quality, as it contains the same scale and unit as the variables *X* and *Y*. The RMAE is considered the most robust measure of accuracy as it is not influenced by outliers and neutralizes the positive and

negative errors (Winter, 2007). van Rijn *et al.* (2003) proposed a RMAE calculation for wave height (H) and current velocity (V) that takes into account measurements errors, which was ΔH_x=0.1 m for wave height and ΔV_x=0.05 m/s for current velocity (Table 5.2). Based on the wave height and current velocity RMAE calculations, van Rijn *et al.* (2003) developed a widely used performance rating for qualifying the goodness of fit between field data and model results (Table 5.3). For calibration of water levels the RMAE calculation for wave height was used.

Table 5. 3: Performance rating according to van Rijn *et al.* 2003.

Qualification	Wave Height RMAE	Current Velocity RMAE
Excellent	<0.05	<0.1
Good	0.05-0.1	0.1-0.3
Reasonable/fair	0.1-0.2	0.3-0.5
Poor	0.2-0.3	0.5-0.7
Bad	>0.3	>0.7

5.2.3 Calibration Results

5.2.3.1 Water levels

The best calibration against field data for water levels was achieved using overall Manning coefficient 0.02 $s/m^{1/3}$ and eddy viscosity 10 m^2/s (Figure 5.1). At all three offshore locations the overall model produces an excellent representation of water levels (Table 5.4). Most importantly, the water levels computed closer to the mangrove forest (C5) also showed excellent comparison with field data. Water levels at Tararu show a slightly larger error (Table 5.4) but still qualify as a good comparison.

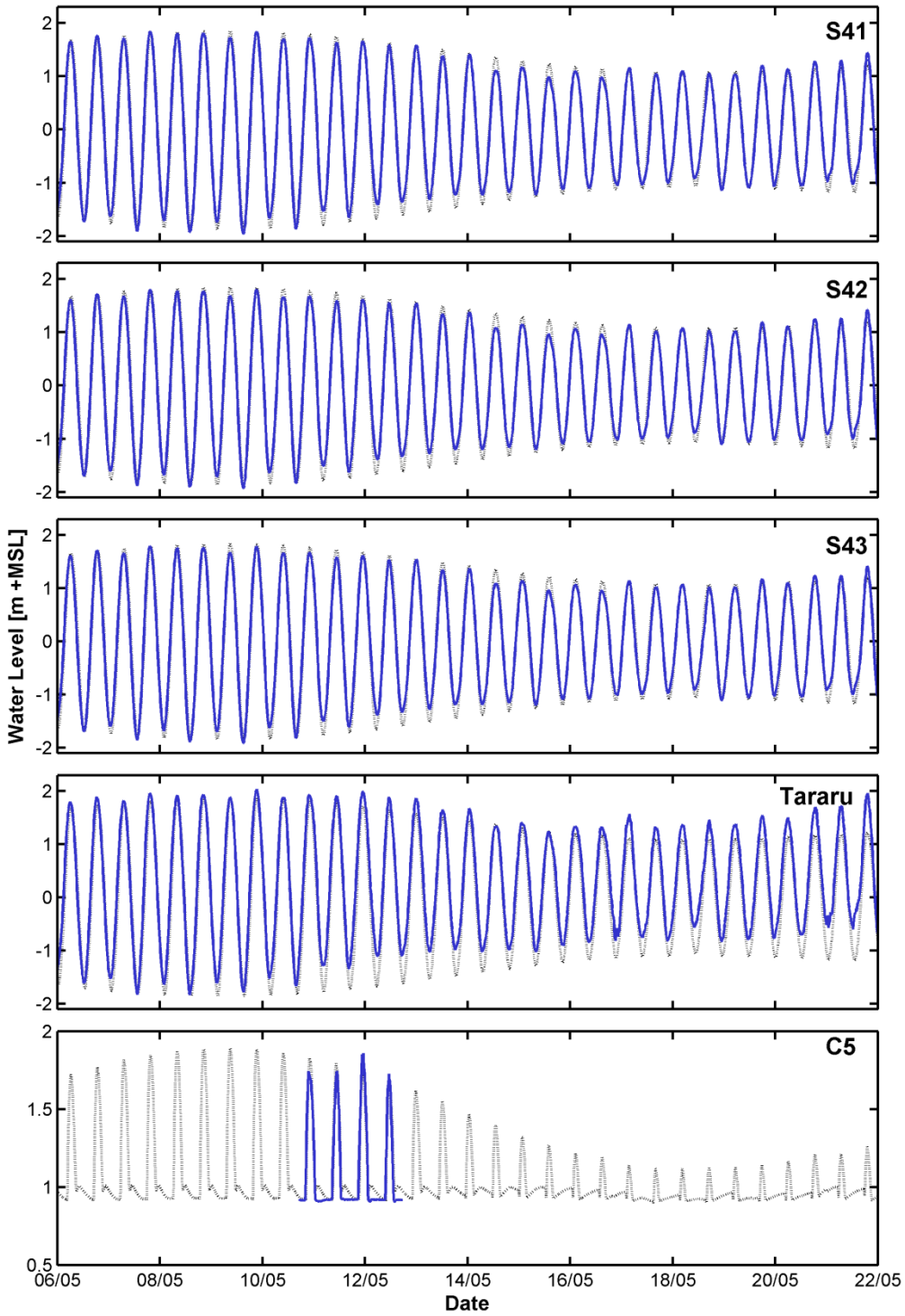

Figure 5. 1: Comparison between the water levels predicted by the overall model (dashed line) and the water levels measured in the field (solid blue line) during May 2016.

Table 5. 4: Overall model water level errors and model qualification based on van Rijn *et al.* 2003.

Location	ME	RMSE	RMAE (van Rijn)	Qualification
S41	0.106	0.073	0.007	Excellent
S42	0.113	0.098	0.015	Excellent
S43	0.112	0.095	0.014	Excellent
Tararu	0.287	0.072	0.053	Good
C5	0.057	0.074	0.039	Excellent

5.2.3.2 Current Velocities

Calibration of current velocities could only be achieved for the offshore region, as the locations Tararu and C5 did not have velocity field measurements (Figure 5.2). The current velocities computed in the offshore region showed good comparison with the S4 measurements (Table 5.5). At all three S4 locations the model overestimated the current velocity, especially for the ebb tide (Figure 5.2). S42 showed the smallest RMAE value, which was favourable since S42 is located in the centre of the Firth, making it the closest S4 to the region of interest (Table 5.5).

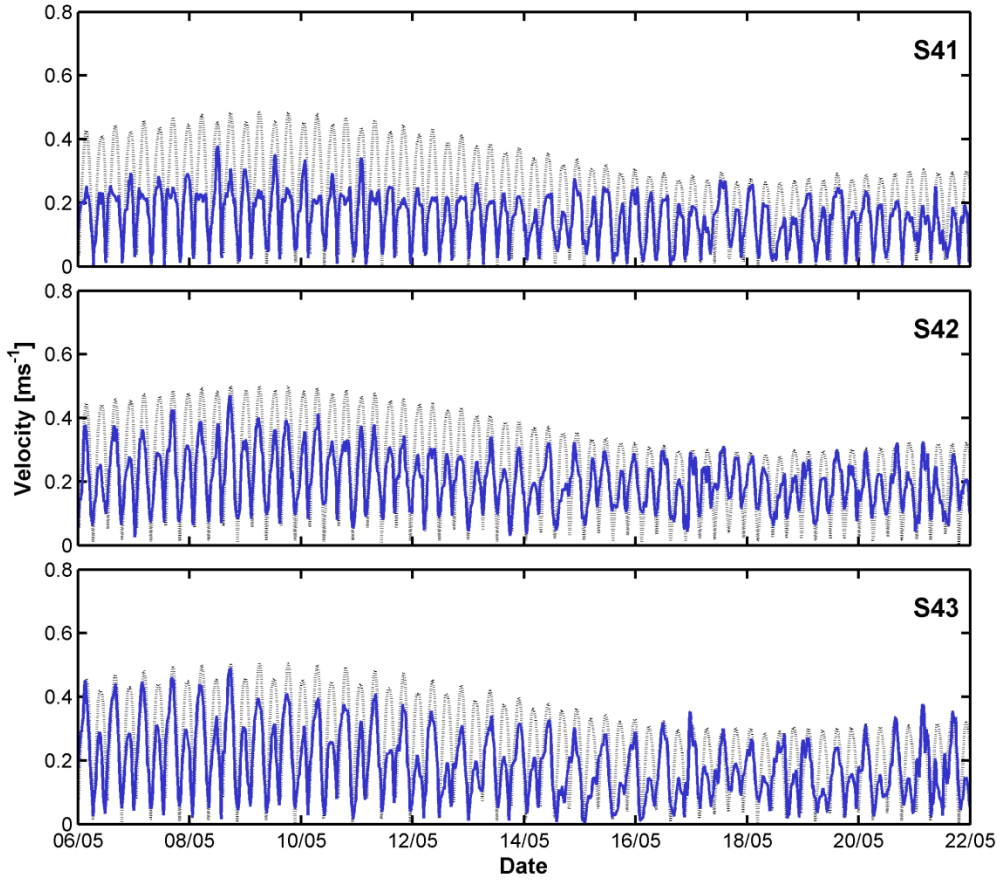

Figure 5. 2: Comparison between the current velocities predicted by the overall model (dashed line) and the current velocities measured in the field (solid blue line) during May 2016.

Table 5. 5: Overall model current velocity errors and qualification based on van Rijn *et al.* (2003).

Location	ME	RMSE	RMAE (van Rijn)	Qualification
S41	0.075	0.131	0.268	Good
S42	0.044	0.138	0.140	Good
S43	0.064	0.110	0.221	Good

5.3 Sources of error

The overall model shows a desirable level of accuracy for forcing the boundary conditions of the nested model. Some of the overall model error could be associated with the forcing from the NIWA tidal model which in itself has amplitude error 1 m and phase error 7^{o} (Walter *et al.,* 2001). However, the excellent water level calibration indicates that this error is small. The slightly larger water level error at Tararu could be due to error associated with the tide gauge readings.

Calibration of current velocities is generally more difficult than water levels because velocities tend to show larger spatial and temporal variation. Consequently, the spatial and temporal averaging of a model limits the accuracy in which the model can predict velocities (Oldman *et al.,* 2004). Hence, the coarse grid resolution in the offshore region may explain why the error in current velocity is higher than water level errors. Another factor that could explain the discrepancy between modelled and observed velocities could be that the model output is depth-averaged velocity whereas the S4 current meter data is velocity measured 1 m above the sea bed. The depth-averaged velocities are the velocity at 0.37of the mean water depth. The mean water depth near the S4 is 5.8 m; therefore the depth averaged velocity is at about 2.1 m, whereas the field measurements were taken at 1 m above the sea bed. Hence because of the logarithmic flow profile that occurs above the sea bed, the velocities higher above the bed are faster (Soulsby, 1997).

5.4 Nested Model Calibration

No velocity data within the mangrove forest were collected so only water levels could be objectively assessed for the performance of the nested model. Due to little inundation of the pressure sensors within the mangrove forest during neap tides (Chapter 3) and computational efficency, only six spring tidal cycles were

used to calibrate the nested model output (Figure 5.3). Different pneumatophore densities ranging from 50 to 500 per m^2 were trialled to determine the minimum water level error. The optimum pneumatophore density was 300 per m^2. Based on the results from the overall model calibration, bottom roughness and eddy viscoisty were kept at 0.02 $s/m^{1/3}$ and 10 m^2/s, respectively.

5.4.1 Calibration Results

Based on the van Rijn *et al.* (2003) classification, the nested model shows excellent representation of water levels within the mangrove forest (Table 5.6). The timeseries comparison shows that the timing of the tide is simulated well. Although, some of the tidal peaks that were simulated by the model are not shown in the field measurements (especially along the eastern transect). However, this discrepency is most likely due to the field instruments not measuring the very low water levels.

Table 5. 6: Nested model water level errors and qualification based on van Rijn *et al.* (2003).

Location	ME	RMSE	RMAE (van Rijn)	Qualification
E1	0.08	0.08	-0.01	Excellent
E2	0.06	0.06	-0.03	Excellent
E3	0.03	0.03	-0.04	Excellent
C1	0.01	0.02	-0.05	Excellent
C2	0.02	0.03	-0.05	Excellent
C5	0.09	0.11	-0.01	Excellent

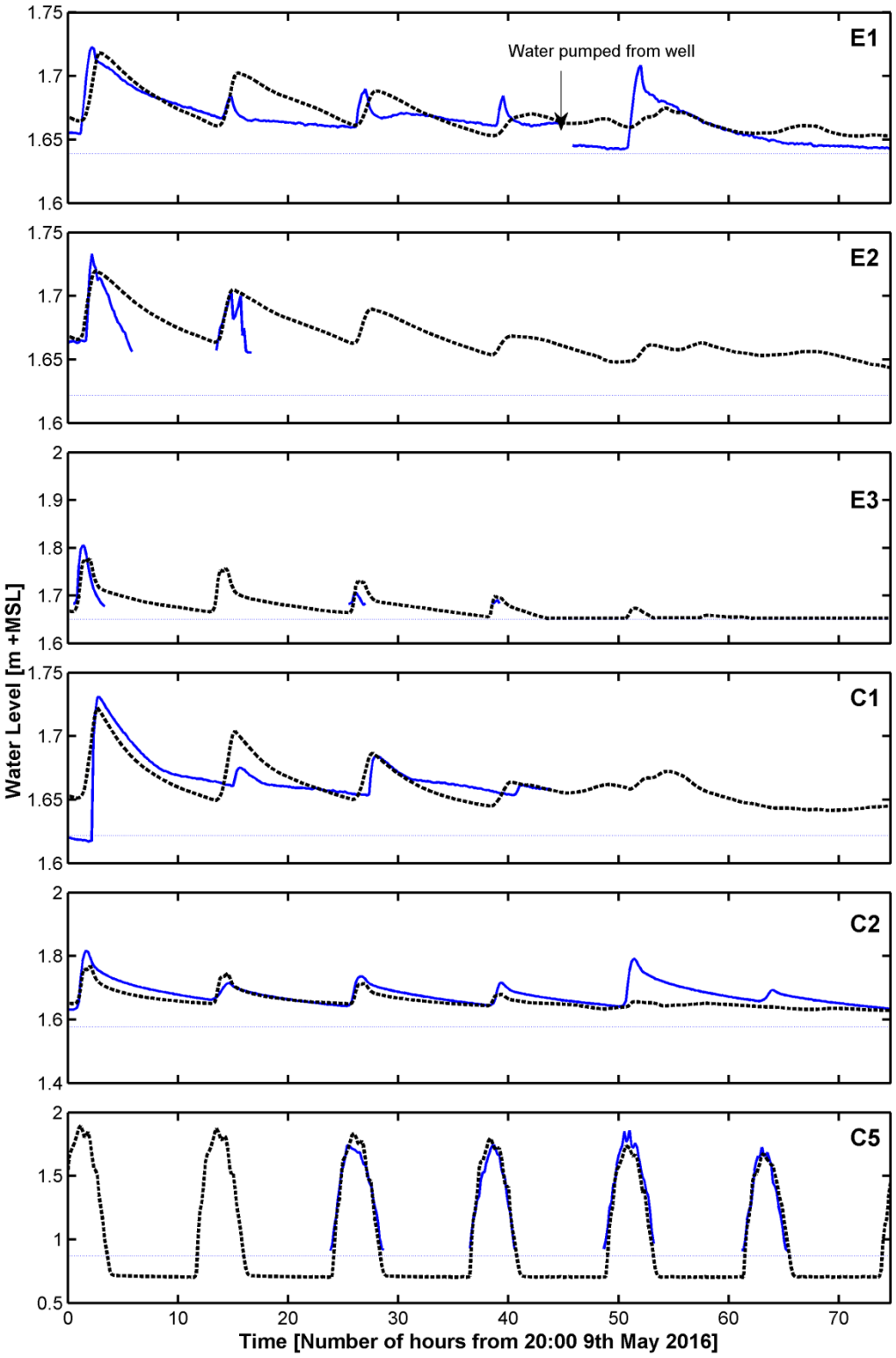

Figure 5. 3: Comparison between the water levels predicted by the nested model (dashed line) and the water levels measured in the field (solid blue line) during May 2016 (site locations are provided in Figure 3.1).

5.5 Conclusion

Trials of different bed roughness and vegetation density allowed the overall and nested models to be successfully calibrated against field data. Both models show excellent representation of water levels, both offshore and within the mangrove forest. Velocities in the offshore region also calibrated well for the overall model, with slightly larger errors due to the large spatial and temporal variation associated with current velocities. The quantitative evaluation of model performance provides some confidence in the model results for assessing the hydrodynamics within the mangrove forest in the Firth of Thames. Due to the nested model only being calibrated to spring tidal cycles, the following chapters and analyses are focused only on the spring tide hydrodynamics.

CHAPTER SIX - TIDAL WAVE CHARACTERISTICS WITHIN MANGROVE FOREST

6.1 Introduction

Numerical models are a useful tool to undertake controlled experiments on the effect on hydrodynamics conditions of vegetation. Although there are many parameterisations within these models, these parameterisations represent our best understanding of how the system responds to changes. Field conditions are variable so there is always uncertainty in some input parameters. Sensitivity analyses are often used to understand what influence the different input parameters have on model outputs.

Previous studies have used sensitivity analyses to explore in more detail how different aspects within a system can affect the processes of interest. For example, Horstman *et al.* (2015) completed a sensitivity analysis to isolate the effects and determine the different contributions of different biogeophysical settings (topography, vegetation density, relative elevation, sediment supply and mangrove expanse) to tidal flow routing and deposition within a mangrove forest. Likewise, Mazda *et al.* (1995) trialled a series of different vegetation drag coefficients within a mangrove swamp and were able to identify that as drag increased within the forest, creek ebb-tide velocities increased, but when drag became excessive the effect was decreased. Sensitivity analyses can also help with generalising results to other sites with slightly different conditions (Horstman *et al*., 2013).

In the following chapter, firstly the water level and velocity patterns from the calibrated model, that includes mangroves, are compared with the water levels and velocities from a model that has no vegetation input. In order to explore the effects and processes further, a sensitivity analysis is also discussed to identify what aspects of the vegetation have the largest effect on model output. Finally, model velocities are compared against velocity measurements from the field.

6.2 Effect of Vegetation

Results from the numerical model indicate that the presence of mangroves in the Firth of Thames does influence the tidal wave dynamics. Cross-sections of the centre transect, with and without vegetation present differences in both the water levels and velocities as the tide propagates across the intertidal flat (Figure 6.1). Offshore water levels and velocities are identical for both the model including vegetation and the model without vegetation. However, as soon as the tide reaches the vegetation, there is a reduction in the propagation speed and current velocities are reduced (Figure 6.1.A) with the introduction of vegetation. As the tide moves further through the forest, it continues to slow down compared to the tide when there is no vegetation (Figure 6.1.B). Overall, when mangroves are present both the flood and ebb velocities are reduced (Figure 6.2). The reduced current velocity within the mangrove forest is consistent with the findings from van Maanen *et al*. (2015), Horstman *et al.* (2015) and Li *et al*. (2012). Previous studies describe how the linear effect of friction removes energy from the tidal wave and as a result the amplitude and propagation speed are reduced (Parker, 1985). The water level plots for locations C1 and C2, demonstrate how the amplitude of the tidal crest and trough are reduced when mangroves are present (Figure 6.2.B).

Within the mangrove forest (C1 and C2) the tidal wave is slightly progressive (Figure 6.3). In a completely progressive wave, the water level and current velocities are in phase so that the maximum velocity occurs at the same time as the maximum amplitude. Dronkers (1986) explains how friction removes energy from the incoming tidal wave, consequently the reflected wave is smaller than the incoming wave and the tidal motion has the character of a partly progressive wave. Parker (1985) also mentions how friction can cause a wave to become more progressive.

As a consequence of slowed tidal wave propagation within the mangroves, there is a delayed response between the water levels inside the forest and water levels offshore. This is displayed in the interesting dome shape that occurs for a short period of time in the water level surface when vegetation is present (Figure 6.1.D). Water levels at the back of the mangrove forest continue to flood while the front of the forest starts to drain (Figure 6.1.D). In contrast, without vegetation the

water levels at the landward extent of the intertidal flat, respond almost immediately to the changes in water level offshore (Figure 6.1.D).

The delayed response is also evident at end of the ebb tide where the tidal flat is still draining at the time the incoming tide starts to flood. Hence, for a short period of time, the velocities at C4 are negative/offshore, even though the water levels have started to increase (Figure 6.1.F & Figure 6.2.A). The delayed ebb drainage from the tidal flat also appears to influence the initial flood velocities further offshore at C5. Although the initial flood velocities at C5 are not negative, they are close to zero and are probably dampened due to the opposing ebb drainage offshore (Figure 6.2.A). The concept of delayed ebb drainage from mangrove tidal flats has also been observed by Lessa & Masselink (1985), Mazda *et al.* (1995) & Furukawa *et al.* (1997). These studies attribute delayed ebb drainage within mangrove creeks to the perched water levels that occur due to the high friction environment within the mangroves. Figure 6.2.B shows that the low tide water levels within the forest are higher when vegetation is present, indicating that the phenomena of perched water levels also occurs within the mangroves in the Firth of Thames. The model simulation without mangroves does not show perched water levels, and hence there is not the same extent of retarded outflow of water on the ebb tide (Figure 6.1.F & Figure 6.2.A).

Even though the pressure gradient between water levels within the forest and offshore, is greater with vegetation (due to more water being trapped) (Figure 6.1.E), the frictional effect of vegetation dampens the ebb velocities, hence the falling tide without vegetation still has higher velocities (Figure 6.1.E).

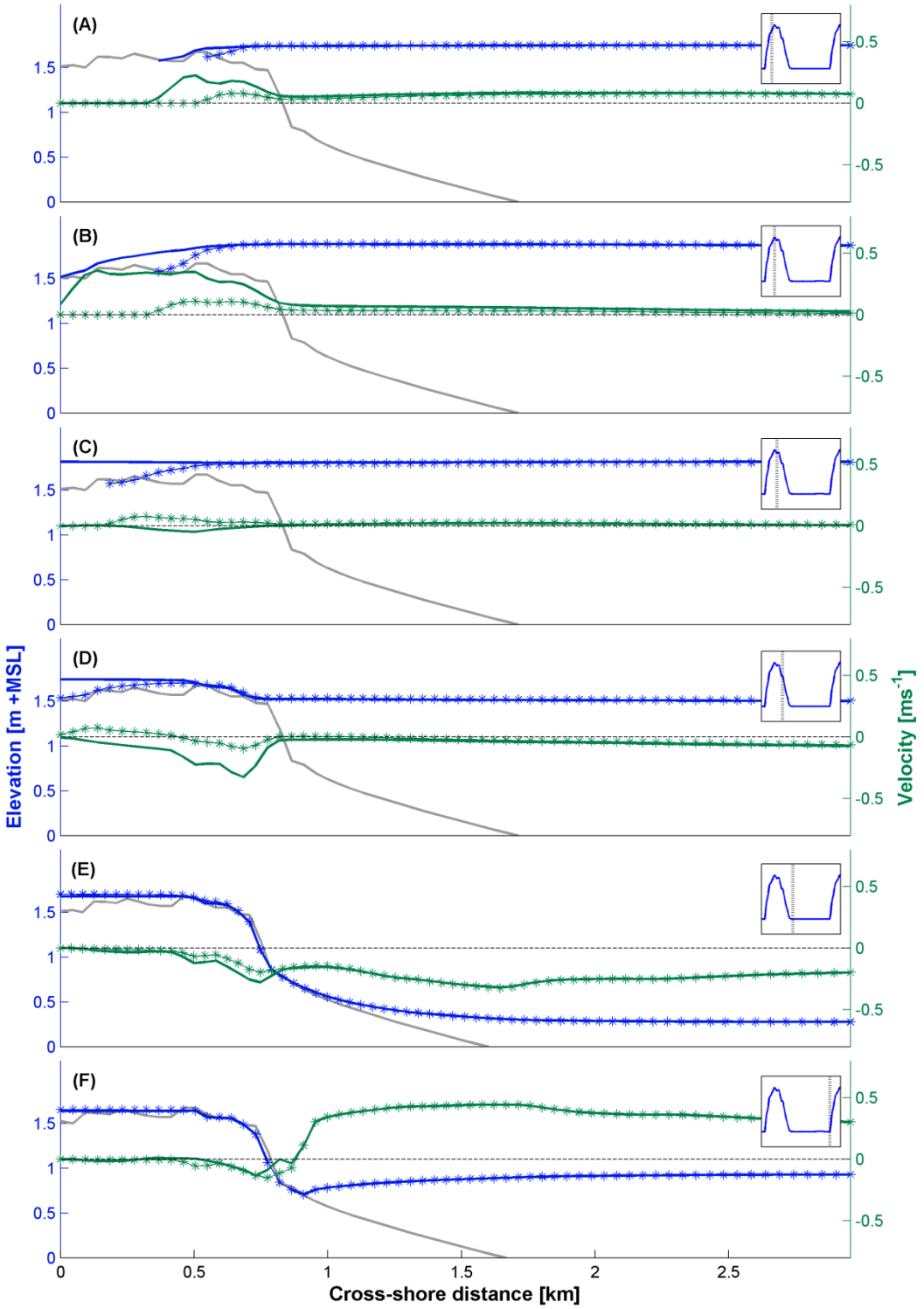

Figure 6. 1: Cross-sections along the centre transect with water levels (blue) and velocity (green) for the vegetated (*) and non-vegetated (solid lines) models. The stage of the tidal cycle is indicated by the vertical line in the water level subplots (top right corner).

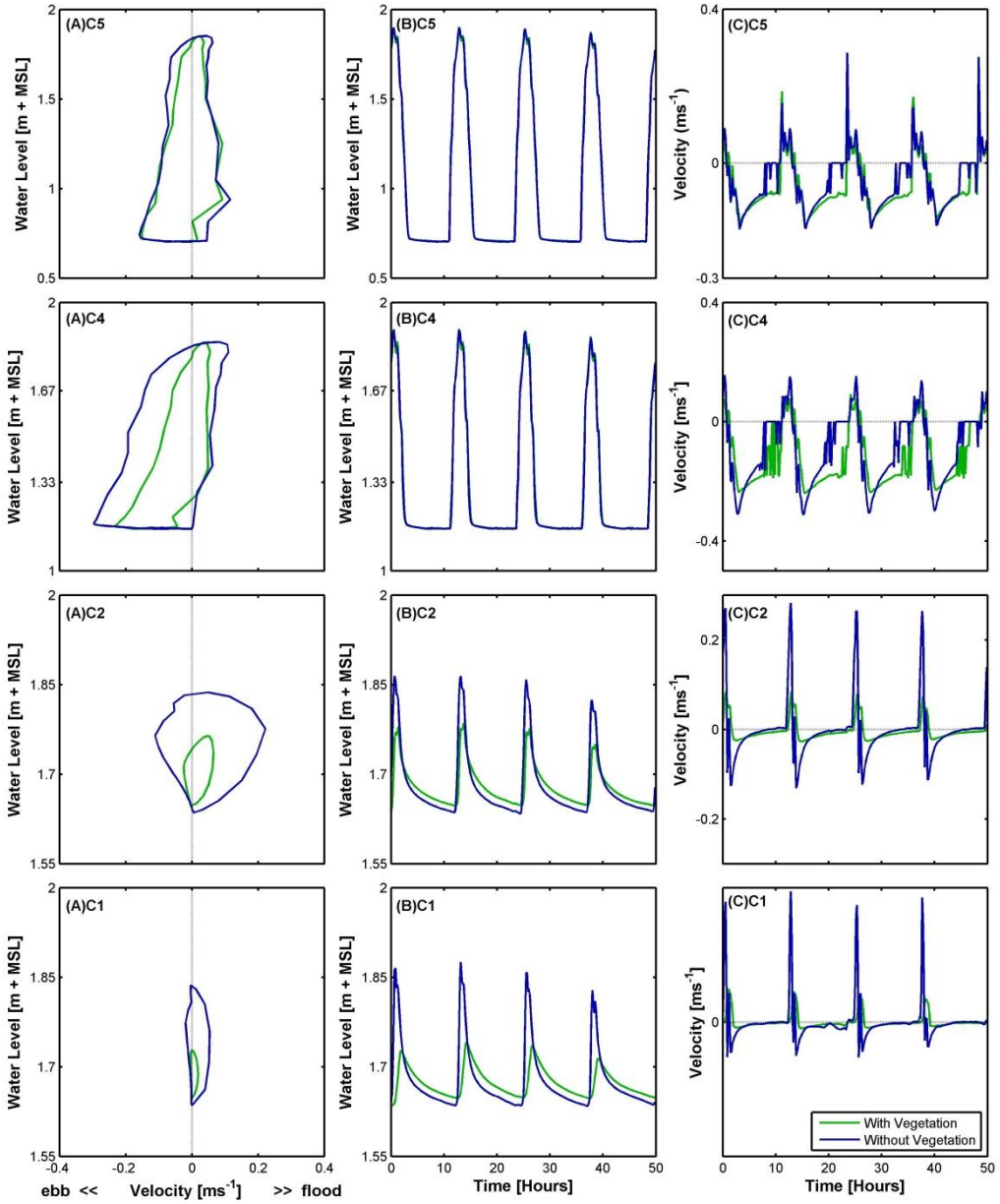

Figure 6. 2: Tidal stage plots (A), water level timeseries (B) and velocity timeseries (C) for model output with vegetation and without vegetation for four sites along the middle transect.

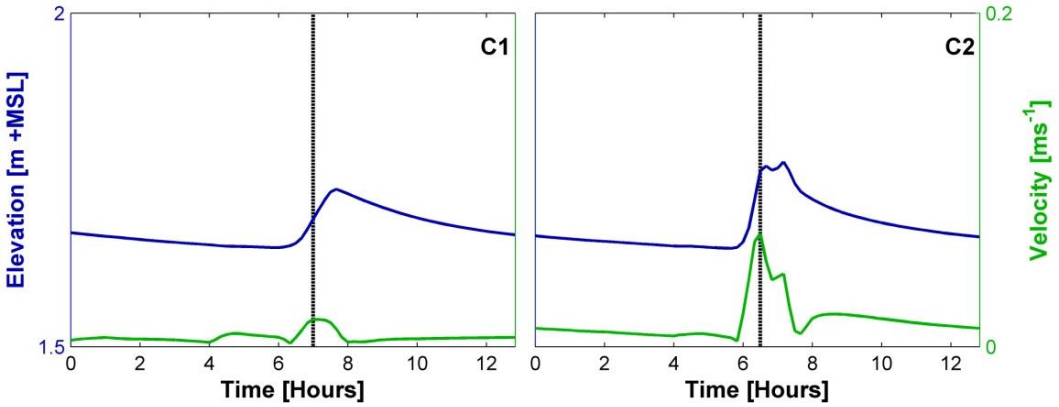

Figure 6. 3: Velocity and water level timeseries for a single tidal cycle within the mangrove forest at C1 and C2 (black horizontal line indicates the time of maximum current velocity).

6.2.1 Tidal Asymmetry

Tidal asymmetry is the distortion of the tidal wave due to the growth of tidal harmonics, which normally arises from the inertial terms in the momentum equation, but can equally arise from the effect of nonlinear friction. If the duration of the flood tide is shorter/longer than that of the ebb tide, then the maximum flood velocities tend to be larger/smaller than the maximum ebb velocities and the system is referred to as flood/ebb dominant, respectively (Dronkers, 1986).

Comparison between the maximum flood and maximum ebb current velocities calculated from the model output, indicate that at outside the forest (C5) and at the fringe (C4) the tidal wave is ebb dominant, whereas within the mangrove forest (C1 & C2) the tidal wave is flood dominant (Table 6.1).

This transition from ebb to flood dominance was explored further; with the velocities and water levels extracted for 11 grid cells cross-shore from within the forest to seaward of the forest fringe (Figure 6.4). The tidal stage plots and asymmetry calculations for each grid cell indicate that it is approximately 30 metres from the edge of the upper tidal flat, that the tidal wave changes from ebb to flood dominant. The tidal stage plots also show how the magnitude of flood dominance progressively increases with distance into the forest.

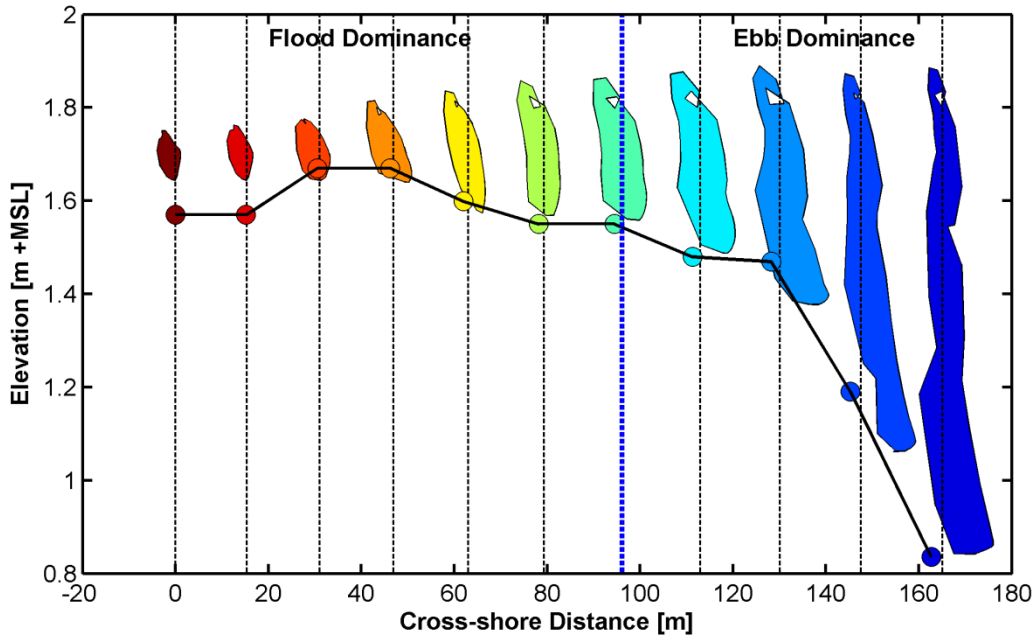

Figure 6. 4: Cross-shore variation in tidal stage plots (water level against current velocity) for 11 grid cells across the mangrove fringe. Black dashed lines indicate the change from ebb to flood velocities in each tidal stage plot. The blue dashed line indicates the grid cell where the tide changes from ebb to flood dominant. Light blue to dark blue shows increasing ebb dominance and Green through to red shows increasing flood dominance. (Cross-shore distance 0 occurs at 37°12'42.29"S 175°26'47.82"E).

Interestingly, the same spatial pattern in tidal asymmetry (flood dominance within the upper tidal flat and ebb dominance at the edge) occurs even when mangroves are not present (Table 6.1). However, when comparing the magnitude of flood/ebb dominance, the magnitude of asymmetry is greater when mangroves are present (Table 6.2).

Table 6. 1: Maximum current velocities calculated at each location along the centre transect for the flood and ebb tide, with and without vegetation (red indicates the larger/dominant tidal stage).

Location	Tidal stage	Without vegetation	With Vegetation
C5	Flood	0.116	0.093
	Ebb	0.159	0.152
C4	Flood	0.111	0.055
	Ebb	0.297	0.232
C2	Flood	0.222	0.066
	Ebb	0.111	0.025
C1	Flood	0.054	0.019
	Ebb	0.020	0.004

Table 6. 2: Ratio of maximum ebb to maximum flood currents at each location along the centre transect, with and without mangroves (ebb dominance>1, flood dominance<1).

Location	Dominance	Magnitude of dominance (max ebb velocity/max flood velocity (ms^{-1})	
		Without Vegetation	With Vegetation
C5	Ebb	1.366	1.634
C4	Ebb	2.681	4.216
C2	Flood	0.501	0.376
C1	Flood	0.366	0.206

The flood dominance across the intertidal flats can most likely be attributed to the effect of nonlinear frictional momentum loss associated with shallower water depths. The linear effect of friction, discussed in Section 6.2.1, causes a delay and decreased amplitude in both high and low waters, but does not distort the wave profile. However, Parker (1985) states that friction can also have nonlinear effects that contributes to the development of harmonics and the distortion of a tidal wave. In the momentum equation (Equation 6.1) (where u is the cross-sectionally averaged velocity, t is time, g is gravity, h is the average depth below mean sea level, η is the surface elevation above mean sea level, and C_f is the friction coefficient), the friction term ($\frac{1}{h+\eta}\, C_f\, u|u|$), has two nonlinear aspects, the quadratic term ($u|u|$) and the elevation effect, due to η in the denominator.

$$\frac{\partial u}{\partial t} + u\frac{\partial u}{\partial x} = -g\frac{\partial \eta}{\partial x} - \frac{1}{h+\eta}\, C_f\, u|u| \qquad \textbf{(6.1)}$$

The elevation effect on frictional momentum loss (per unit volume of fluid), is where frictional loss is greater for smaller water depths. Consequently, friction has a greater impact on the trough (low tide), causing the amplitude and propagation speed of the trough to be reduced compared to the crest (high tide). The resulting wave profile has a shorter flood tide with stronger currents and a longer ebb tide with weaker currents (Parker, 1985, Dronkers, 1986).

The concept of increased frictional effects promoting flood dominance through nonlinear momentum loss is evident in a number of studies (Speer & Aubrey, 1985, Friedrichs & Aubrey, 1988, Brown & Davies, 2007). For example, Speer and Aubrey (1985) showed through numerical modelling that there is a trend

towards flood dominance in shallow channels where friction increases as a function of water depth.

Within the Firth of Thames, the nonlinear frictional elevation effect can also explain the flood dominance across the intertidal flats. Without vegetation, the tide propagates as a shallow water wave across the intertidal flat and hence due to the effect of nonlinear frictional momentum loss, the trough (low tide) becomes delayed. With mangroves present, the friction across the intertidal flat is increased even further, hence the shallow water tidal wave becomes even more distorted and the flood dominance greater (Table 6.2).

Due to the tidal wave distortion across the intertidal flats, the rate of the falling tide across the flats becomes reduced with respect to the falling tide offshore. Consequently, this results in a relatively steep hydraulic gradient that generates fast ebb velocities at the edge of the intertidal flat, hence why there is ebb dominance at C4 and C5 (Table 6.2) (Dronkers, 1986). Since there is greater distortion across the intertidal flats when mangroves are present, the hydraulic gradient becomes greater and therefore the ebb dominance is greater (Table 6.2 & Figure 6.5).

Ebb dominance at the edge of the mangrove forest is similar to the findings of Lessa & Masselink (1995), Mazda *et al.* (1995) and Friedrichs and Aubrey (1988) who discuss how ebb dominance within mangrove creeks increases as the drag within the mangrove forest increases. Lessa & Masselink (1995) found that the steepness of the hydraulic gradient, and thus the ebb-velocity within the mangrove creek, is proportional to the relative extent of the mangrove area.

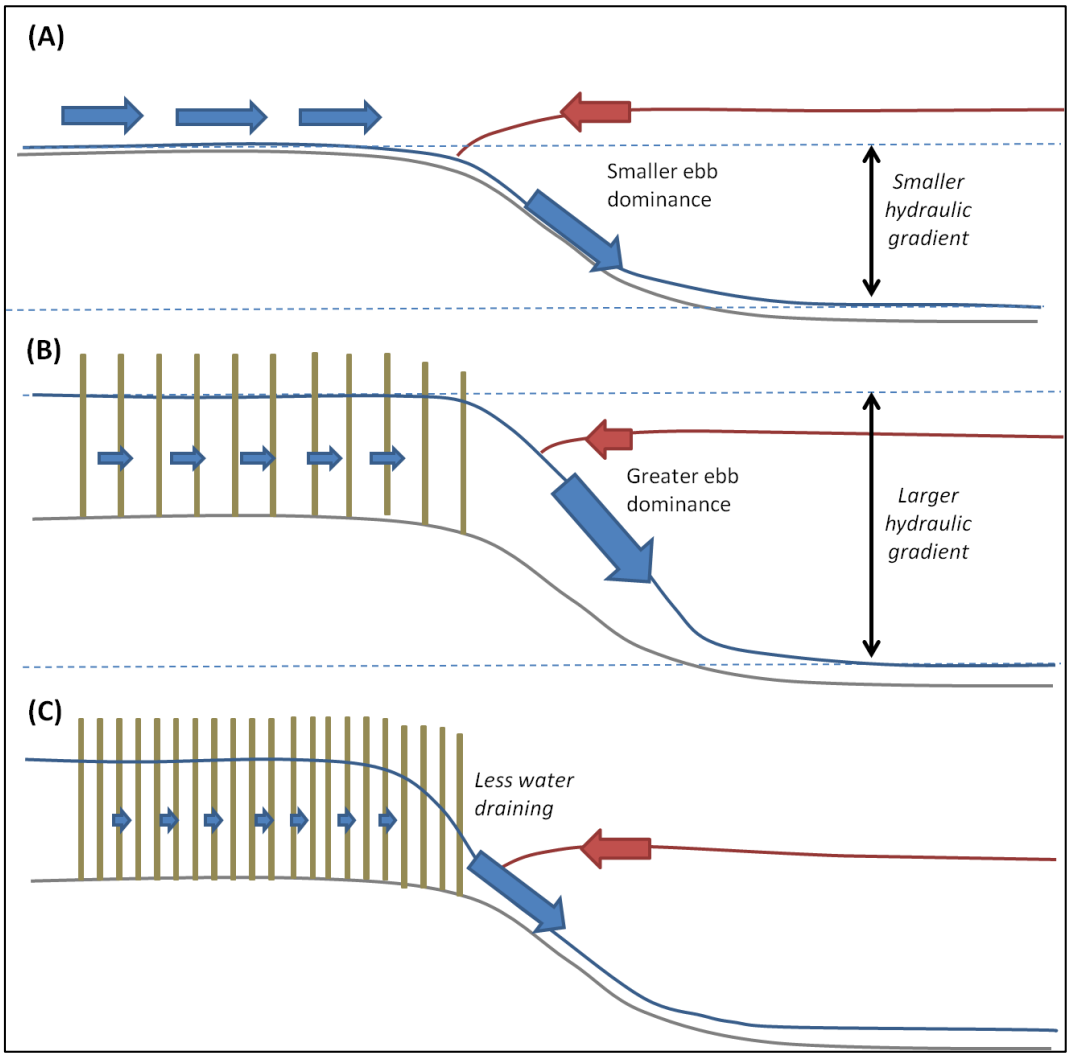

Figure 6. 5: Schematic diagram showing the difference in hydraulic gradients and, hence ebb dominance (A) without mangroves, (B) with mangroves. Plus the ebb drainage and velocity difference at the beginning of the flood tide with (B) standard pneumatophore density and (C) very high pneumatophore density.

6.3 Sensitivity Analysis

Although the comparison between vegetated and non-vegetated model outputs highlighted that the mangroves do influence the tidal wave characteristics, a sensitivity analysis was completed to help understand to what extent and how the different model parameters associated with vegetation influence the tidal characteristics.

A series of 15 different scenarios was run with only a single parameter being altered in each simulation, whilst the others were held constant. Parameters adjusted during the sensitivity analysis are: pneumatophore density,

pneumatophore height, tree density, bulk drag coefficient (C_D) (the roughness of vegetation surface) and bed roughness (Table 6.3). The range of values used for pneumatophore density, pneumatophore height and tree density were determined based on field observations (Appendix I). The range of values applied for bulk drag coefficient and bed roughness were based on values in literature (Nepf, 1999).

Model outputs from the four observation points along the centre transect were used for comparison. The model sensitivity is represented as percentages computed from Equation 6.1, where U_{max} is the maximum flood/ebb velocity for each model run and U_{max0} is the maximum flood/ebb velocity for the baseline model run. Sensitivity percentages were computed for locations C3 and C5 to compare the sensitivity at the forest fringe with the sensitivity within the mangrove forest (Table 6.4).

$$S = \frac{U_{max} - U_{max0}}{U_{\max 0}} \quad \textbf{(6.1)}$$

Table 6. 3: Model parameters adjusted during sensitivity analysis.

Model Parameter	Standard value	Range of trialled values
Pneumatophore Density (no. per m^2)	200	50-500
Pneumatophore height (m)	0.02	0.1-0.4
Tree density (no. per m^2)	5	0.1-15
Bulk drag coefficient (C_D)	1	1-1.6
Bed roughness (Manning coefficient $m^{-1/3}s$)	0.02	0.02-0.04

Table 6. 4: Sensitivity results of U_{max} for each parameter change.

Parameter		Forest Fringe (C4)		Within Forest (C2)	
		Flood	Ebb	Flood	Ebb
Pneumatophore Density	Increase (500per m^2)	-15%	-30%	-34%	-48%
	Decrease (50per m^2)	33%	52%	76%	136%
Pneumatophore Height	Increase (0.4m)	-7%	-2%	-11%	-10%
	Decrease (0.1m)	28%	4%	64%	69%
Tree Density	Increase (15per m^2)	-5%	-9%	-11%	-16%
	Decrease (0.1per m^2)	4%	6%	7%	11%
Bulk Drag Coefficient	Increase (1.3)	-5%	-9%	-11%	-17%
	Increase (1.6)	-8%	-16%	-19%	-28%
Bed roughness	Increase (0.03 $m^{-1/3}s$)	-1%	-5%	-2%	-3%
	Increase (0.04 $m^{-1/3}s$)	-2%	-14%	-4%	-8%

6.3.1 Pneumatophore Density

Overall, the model outputs, both at the forest fringe and within the forest, are most sensitive to changes in pneumatophores density (Table 6.4). The highest sensitivity is apparent in the ebb currents within the forest, where a decreasing pneumatophore density to 50 per m^2 increases the depth-averaged currents with up to 136% and increasing density to 500 per m^2 reduces the depth-averaged currents by up to 48% (Table 6.4). In general, increasing pneumatophore density reduces all current velocities throughout the forest, which is consistent with the concept of increased friction removing tidal energy (see Section 6.2).

An interesting result that is consistent with literature is that as pneumatophore density increases, the ebb drainage becomes gradually more delayed (Lessa & Masselink (1995); Mazda *et al.*, (1995). For the high densities (200 per m^2 and 500 per m^2) there are negative/offshore velocities at the beginning of the flood tide at C4. Whereas at the same tidal stage, for low pneumatophore density (50 per m^2), the velocities are positive/onshore (Figure 6.6.A). This pattern was also observed between the vegetated and non-vegetated model runs (Figure 6.2.A). The sensitivity analysis indicates that once past a density threshold (between 50 per m^2 and 200 per m^2), the ebb tide becomes so delayed that, for a short period of time while the incoming tide starts to flood at C4, there is an opposing current offshore.

Interestingly at C5, the flood velocities are greater in magnitude for higher densities (500 per m^2) than compared to lower pneumatophore densities (50 & 200 per m^2) (Figure 6.6.A). When pneumatophore density is really high less water drains out on the ebb tide and the effect of the opposing ebb drainage has slightly less of an impact on the initial flood velocities (Figure 6.5.C & Figure 6.6.A). Consequently, the flood velocities for high pneumatophore density are slightly larger than the low pneumatophore density (Figure 6.6.A).

Water levels at the edge of the mangrove forest show no variation with changes in pneumatophore density (Figure 6.6.A). However, within the forest the water levels are sensitive to pneumatophore density (Figure 6.6.A). Water levels at high tide are reduced with increasing density and during low tide water levels are higher when pneumatophores density is greatest (Figure 6.6.A). Again, the increased friction associated with higher pneumatophore density can explain why the tidal amplitude is reduced and perched water levels become greater (Parker, 1985; Lessa & Masselink, 1985).

The higher low tide water levels associated with higher pneumatophore density indicate that more water is trapped as the drag increases. Consequently, since more water is trapped within the forest, the ebb currents are reduced because water drains less efficiently. At the edge of the mangrove forest (C4 & C5) the effect of frictional drag from vegetation is not significant enough to reduce the tidal amplitude.

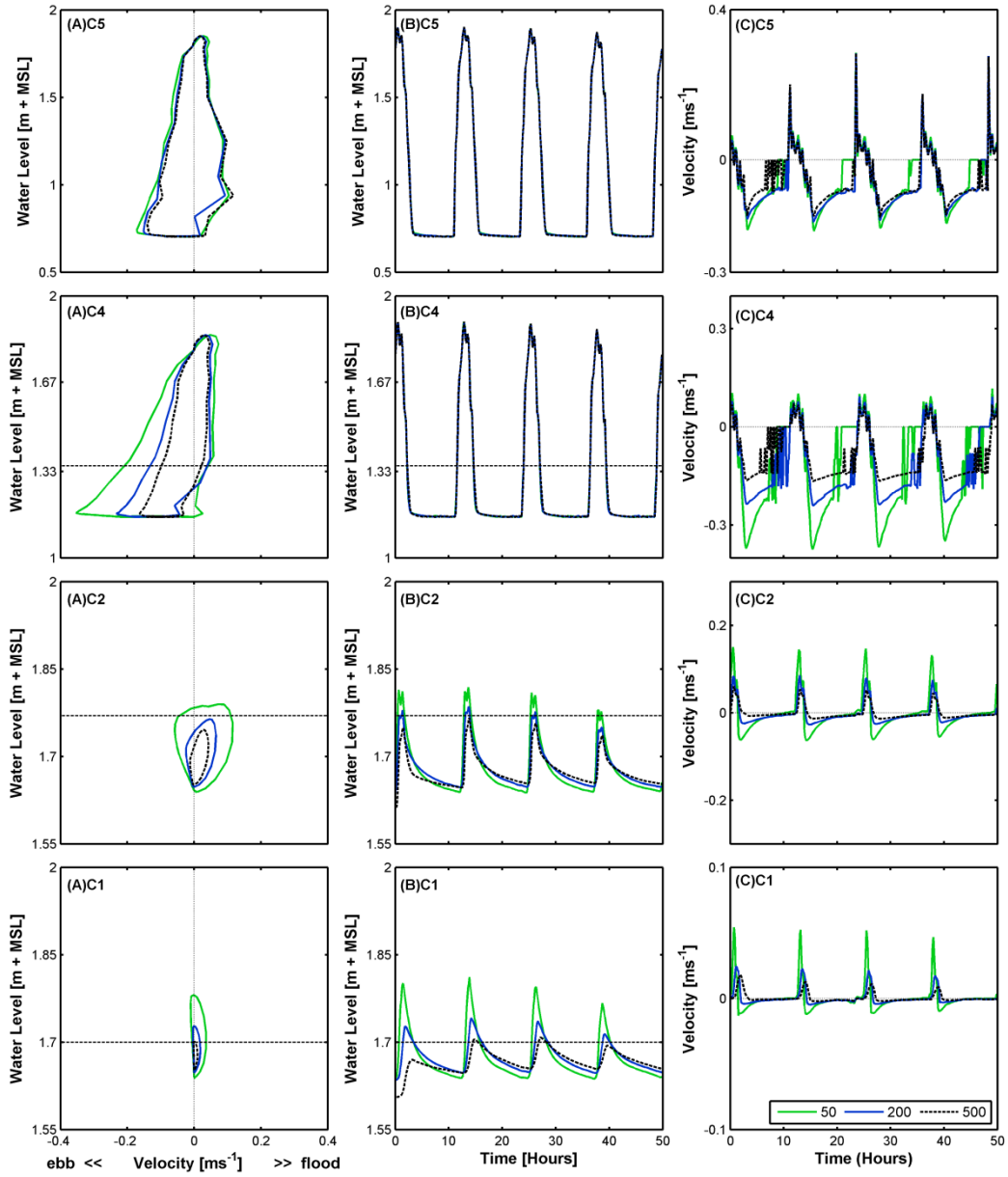

Figure 6. 6: Tidal stage plots (A), water level timeseries (B) and velocity timeseries (C) with different pneumatophores densities (number per m^2) for four sites along the middle transect. Dashed horizontal line represents height of pneumatophores (0.2 m) at each location.

6.3.2 Pneumatophore Height

Pneumatophore height is the parameter with second largest influence on model output. Similar to increasing pneumatophore density, increasing pneumatophore height causes a reduction in current velocity, especially on the ebb tide within the mangrove forest (Table 6.4). This is because when pneumatophore density or height is increased, the surface area of vegetation is increased, therefore the drag is increased and current velocity is reduced (Nepf, 1999). At the edge of the forest (C4 & C5), the pattern in velocities near the beginning of the flood tide for

pneumatophore heights 0.1 m and 0.2 m demonstrate the delayed drainage off the tidal flat, with offshore/negative velocities dominating for a short period of time (Figure 6.7.A). However, when pneumatophore height is 0.4 m the velocities at the beginning of the flood tide are onshore/positive (Figure 6.7.A). The water levels within the forest are reduced for pneumatophore heights 0.4 m (Figure 6.7.B), indicating that less water is flooding into the forest and therefore less water is draining on the ebb tide. Consequently, there is not the same delayed drainage off the tidal flat (as seen with 0.1 and 0.2 m) hence the positive velocities dominate at the beginning of the flood tide (Figure 6.7.A).

The increase in pneumatophore height from 0.1 m to 0.2 m causes the greatest reduction in current velocity at C4; whereas the effect of a further increase from 0.2 m to 0.4 m causes a relatively small reduction (Figure 6.7.A). The difference between pneumatophores heights of 0.1 m and 0.2 m is that the top of the 0.1 m pneumatophore canopy becomes submerged during the high stage of the tide. Consequently, the velocity profile increases above the vegetation (Baptist *et al.*, 2007); hence there is an increase in (depth-averaged) current velocity at the end of the flood tide and at the beginning of the ebb tide (Figure 6.7.A). Since the water depths within the mangrove forest rarely exceed 0.2 m, pneumatophore heights of 0.2 m and 0.4 m are almost always emergent. Depth-averaged flows through emergent vegetation are typically reduced compared to flows through submerged vegetation (Nepf,1999) (Figure 6.8). The high tide water levels within the forest are also reduced when the pneumatophores are 0.2 m and 0.4 m high. Similar to the differences in current velocity, when vegetation is emergent, the entire water column is subject to energy dissipation, whereas in submerged vegetation, the water column above the canopy is less influenced by the friction imposed by the vegetation, hence there is greater dampening of the tidal amplitude and current velocity when the vegetation is emergent (Nepf, 2012; Parker, 1985).

Unlike the effect of increased density, there is no difference in the low tide water level (Figure 6.7.B) indicating that pneumatophore height does not influence how much water is trapped during low tide (Figure 6.9). However, because the high tide water level is lower for taller pneumatophores, there is a smaller drop in the

water level and the ebb-tidal discharge is reduced when pneumatophore height is larger.

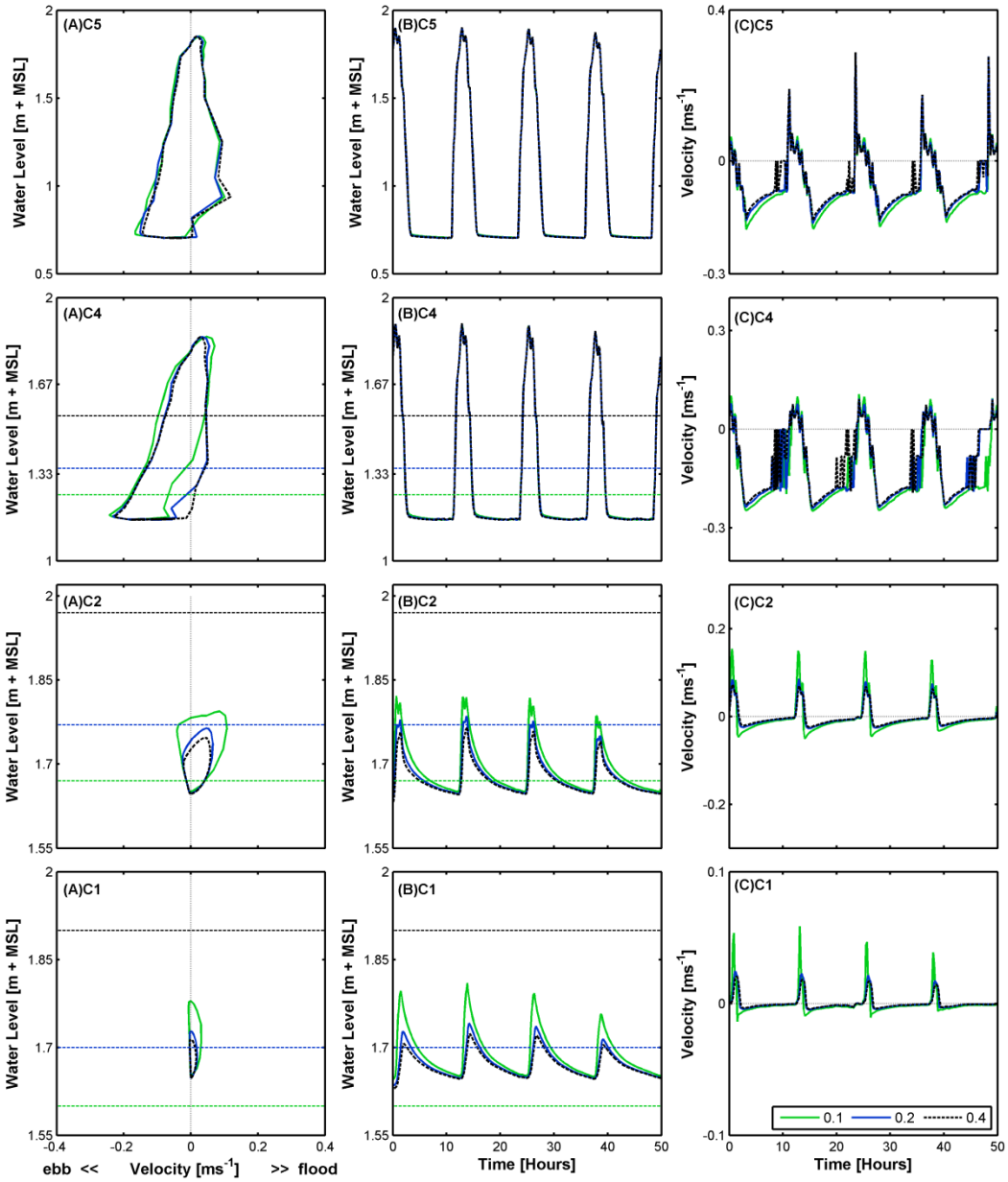

Figure 6. 7: Tidal stage plots (A), water level timeseries (B) and velocity timeseries (C) with different pneumatophores heights (m) for four sites along the middle transect. Dashed horizontal lines represent different pneumatophores heights at each location.

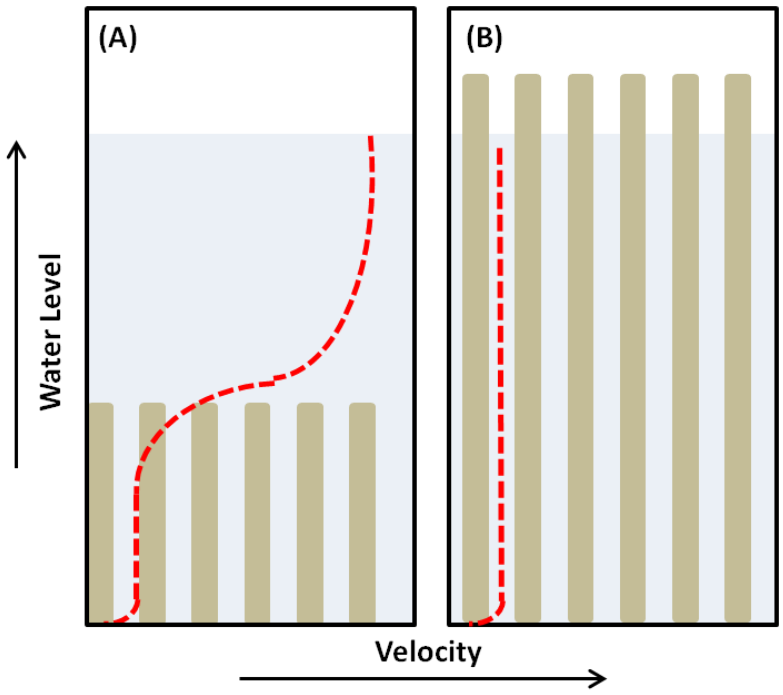

Figure 6. 8: Schematic diagram showing the velocity profile (red dashed line) for flow through (A) submergent vegetation and (B) emergent vegetation.

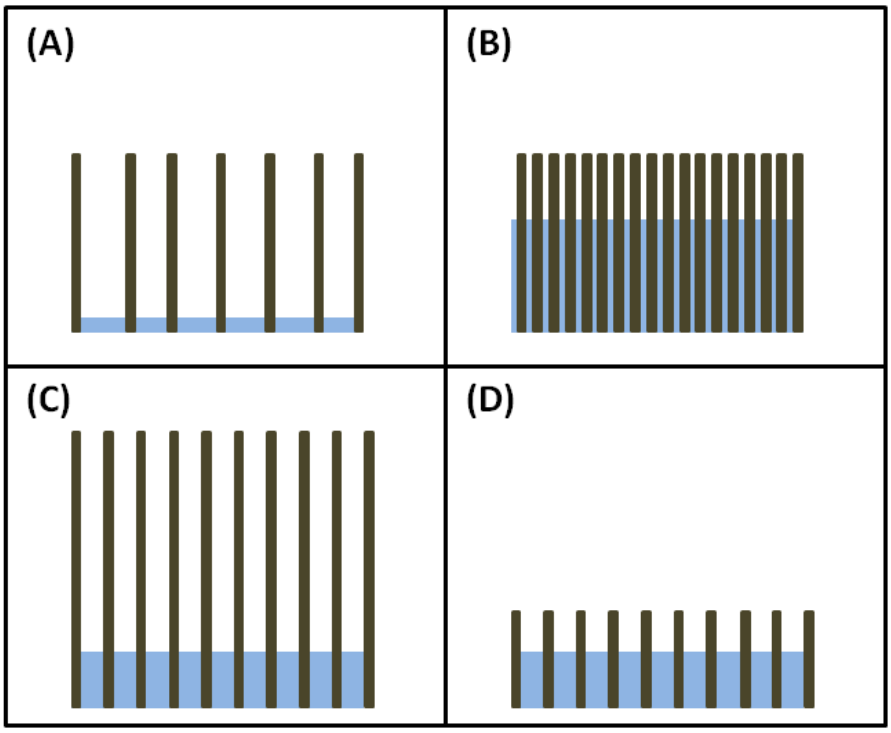

Figure 6. 9: Schematic diagram showing the difference in effects between pneumatophore density (A & B) and pneumatophore height (C & D) on low tide water levels. (A) Low density (B) High density (C) Tall pneumatophores (D) Short pneumatophores.

6.3.3 Tree Density

Tree density has a small influence on model output. As density is increased the water levels and velocities within the forest are slightly reduced (Figure 6.10). Outside the forest (C5) the higher density shows larger flood velocities than the low density (0.1 per m^2) (Figure 6.10.A). These patterns are similar to those described with the changes in pneumatophores density, however the influence of tree density is only minor compared to pneumatophore density (Table 6.4). Although mangrove trees have larger diameters than pneumatophores, they occur in much lower numbers compared to pneumatophores. The frontal area per canopy volume (α) (Equation 6.2) (Nepf, 2012) is the vegetation density parameter used for vegetation input within the model (Equation 4.2), where N is the number of stems per m^2 and d is the stem diameter. The α value for the standard number of trees (5 per m^2) is 6.4 times smaller than the α value for standard number of pneumatophores (200 per m^2) (Table 6.5).

$$\alpha = Nd \quad \textbf{(6.2)}$$

Table 6. 5: Frontal area per canopy volume values for different vegetation sensitivity simulations.

Type of mangrove vegetation	Number per m^2 (N)	Diameter [m] (d)	Frontal area per canopy volume [m^{-1}] (α)
Tree	0.1	0.050	0.005
Tree	5	0.050	0.250
Tree	15	0.050	0.750
Pneumatophore	50	0.008	0.400
Pneumatophore	200	0.008	1.600
Pneumatophore	500	0.008	4.000

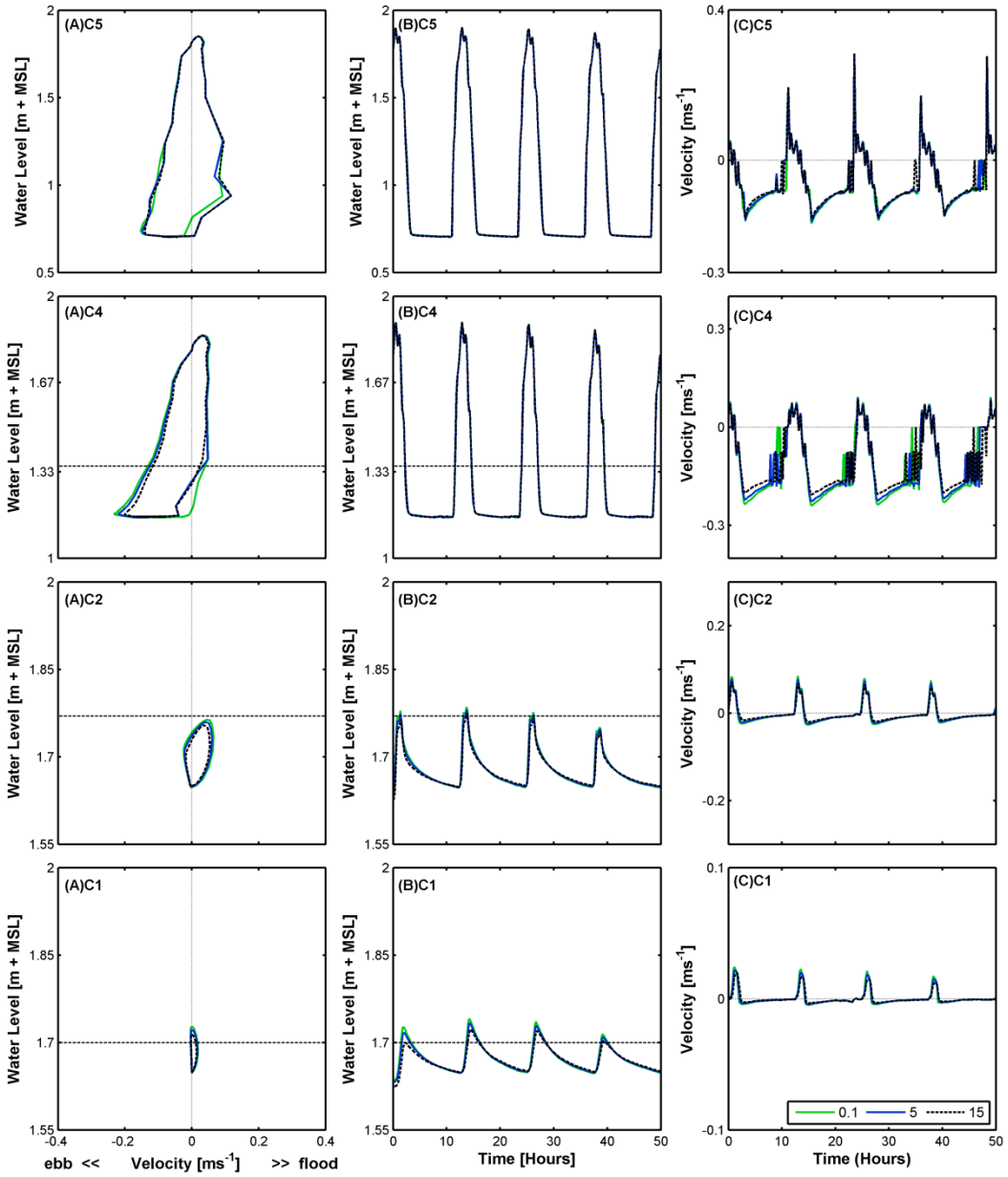

Figure 6. 10: Tidal stage plots (A), water level timeseries (B) and velocity timeseries (C) with different tree densities (number per m^2) for four sites along the middle transect. Dashed horizontal line represents height of pneumatophores (0.2 m) at each location.

6.3.4 Bulk Drag Coefficient (C_D)

The effect of increasing the bulk drag coefficient (C_D) from 1 to 1.6 causes a very small reduction in current velocity and water level throughout the forest (Figure 6.11). Similar to the pneumatophore density and height simulations, the ebb currents were more sensitive than flood currents to variations in C_D values (Table 6.4). The influence of C_D on model output is not as large as the influence of pneumatophore density (Table 6.4). This is because the model input only

multiplies the C_D value by the density (Equation 4.2). Hence, because the variation in C_D values is a lot smaller than the variation in pneumatophore density, there is less of a difference in model output.

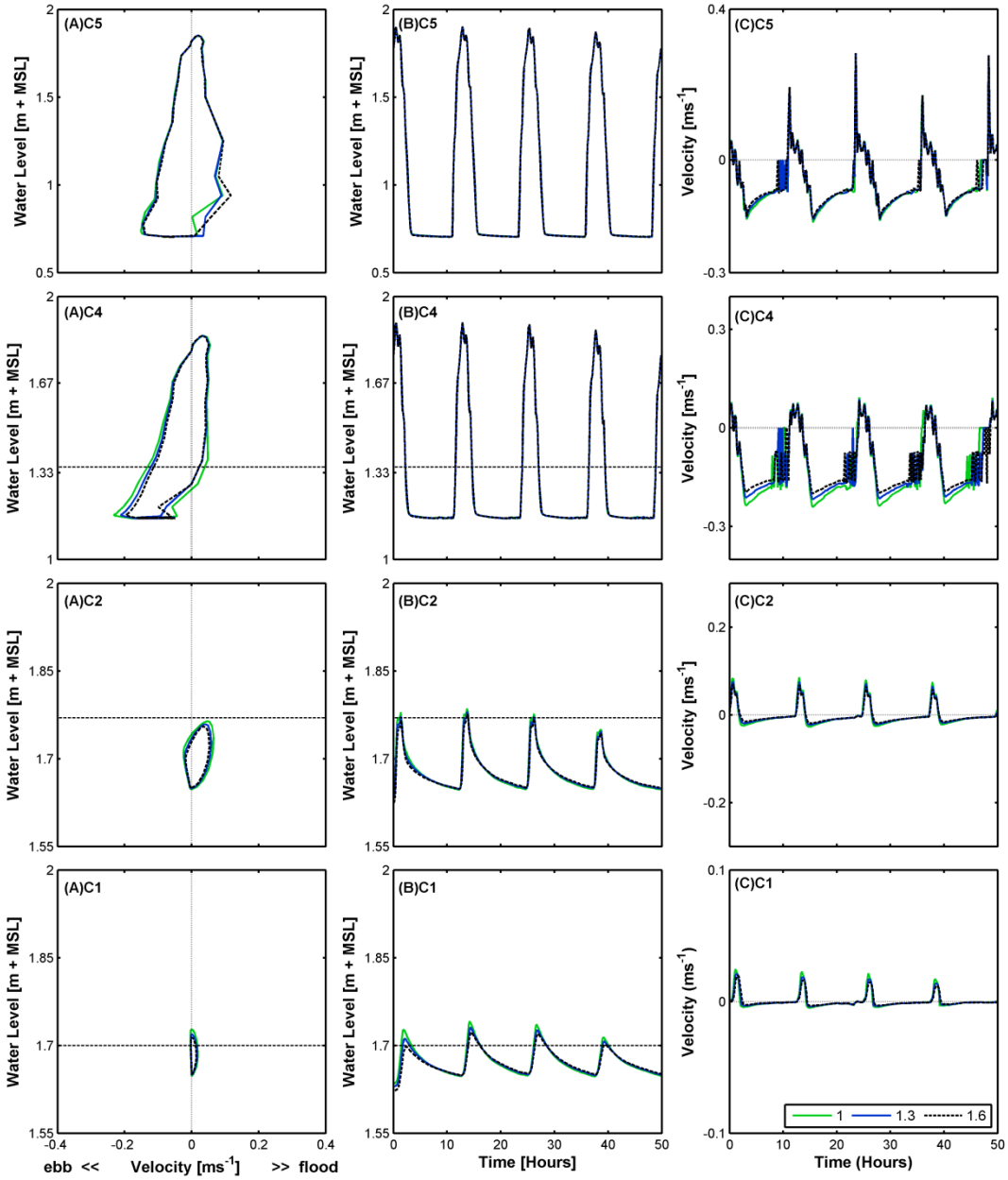

Figure 6. 11: Tidal stage plots (A), water level timeseries (B) and velocity timeseries (C) with different bulk drag coeffients for four sites along the middle transect. Dashed horizontal line represents height of pneumatophores (0.2 m) at each location.

6.3.5 Bed Roughness

The sensitivity to bed roughness within the forest is very small (Table 6.4); this is most likely due to the effects of vegetation dominating hydrodynamic energy dissipation (Nepf, 2012). Bed roughness had the greatest influence on the current velocities at C4, where increasing bed roughness reduces the current velocity (Figure 6.12.C). The influence of bed roughness is partly dependent on water depth. For example, during high water levels at site C4 & C5 there is no difference in velocity with varied bed roughness, however, during low water levels the influence is evident (Figure 6.12.A). The effect of vegetation at C4 is less than that within the forest (C1 & C2) and the water depths are shallower compared to the offshore site C5, hence the bed roughness has a greater impact on current velocities at this site (Figure 6.12.A).

Although changing the bed roughness within the forest does not appear to have a large influence on the velocities within the forest, it does appear to have an effect over the entire system. This is because at C4 the initial flood velocities become more negative for the highest bed roughness, which can only be due to the delayed discharge from the inner forest (Figure 6.12.A). So, increasing the bed roughness within the forest causing the changes at C4 as well as the effect of changing roughness at C4 itself.

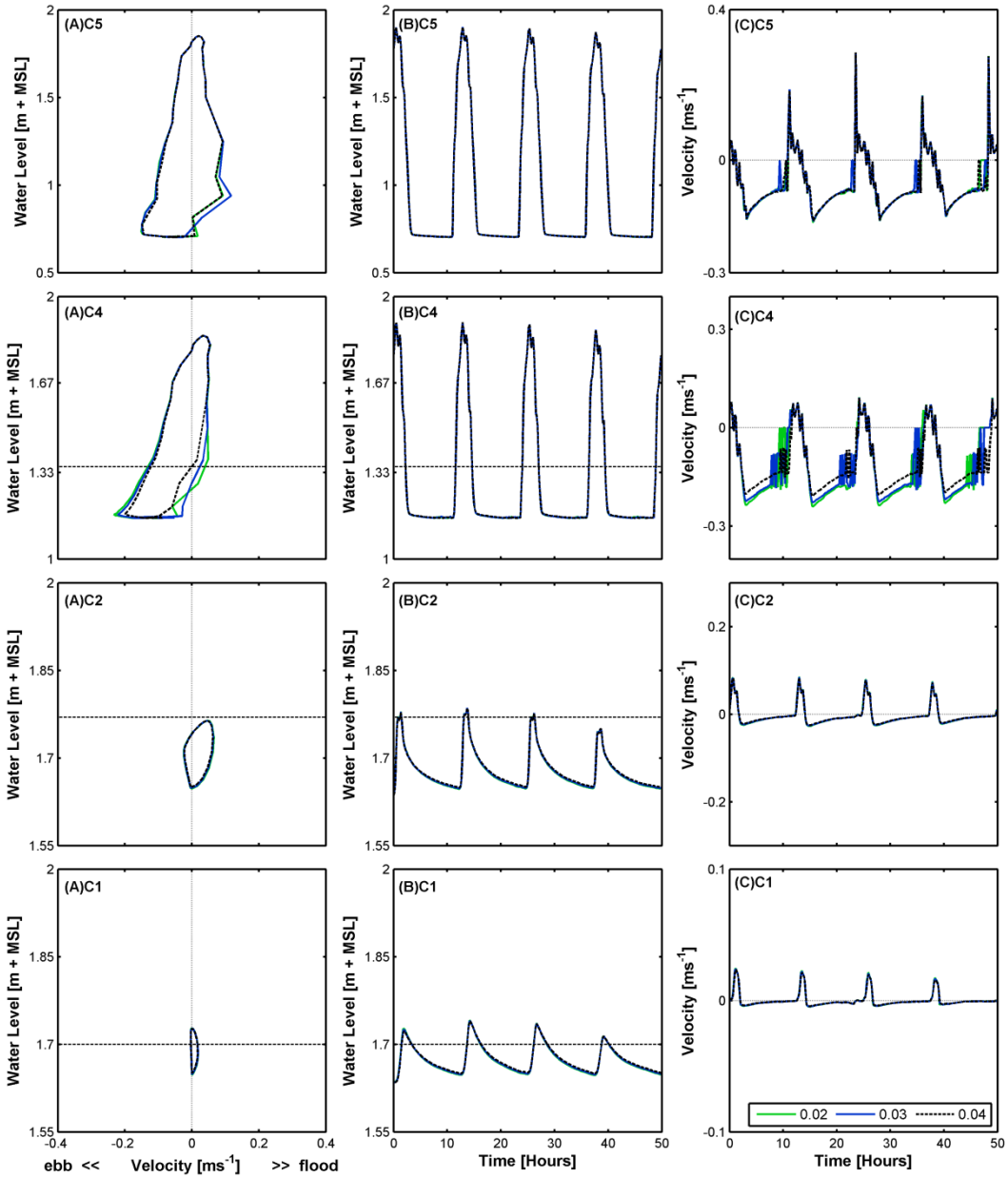

Figure 6. 12: Tidal stage plots (A), water level timeseries (B) and velocity timeseries (C) with different bed roughness for four sites along the middle transect. Dashed horizontal line represents height of pneumatophores (0.2 m) at each location.

6.4 Real World Comparison

While velocity data was not collected during the May 2016 field deployment for complete model calibration (Chapter 5), velocity was measured close to location C4 during a separate field deployment between 14th and 25th November, 2016 (funded under Marsden contract 14-UOW-011 to Karin Bryan and Julia Mullarney). This data was provided so that I could undertake a preliminary validation of my modelled tidal currents. Data from the Aquadopp current meter

deployed in November was compared with the C4 outputs from the model simulated for the 4th to 24th May, 2016. The segment of data was aligned to the modelled data so that data from the same stages of the spring-neap cycle were compared. The comparison shows a relatively good fit, with the model simulating average velocity and water level patterns, close to what is observed in the real data, particularly on the flood tide (Figure 6.13). However, there is a relatively large discrepancy between model and observed velocities at the end of the ebb tide, where the field data does not show the same ebb-drainage pattern (Figure 6.13).

One factor that could explain this discrepancy is that the model does not take in account groundwater flow. It is possible that within the real system the ebb velocities are not as strong because the very low water levels infiltrate into the groundwater, instead of flowing offshore. The model represents an impermeable bed, where the only flow path for the ebb tide is across the ground surface.

Within the real system there are also small runnels that are about 20 to 40 cm wide (Karin Bryan, personal communication, November 30, 2016). Although there are no large creek systems within the Firth of Thames, the small runnels could help drain the very low water levels and display velocity patterns similar to those characteristic of mangrove creeks. Due to the model grid resolution (30 x 30 m) these small features are not included in the model. However, if velocity measurements were taken from within one of the small runnels, it may compare better with the strong ebb-drainage simulated by the model.

In general, the comparison with field measurements suggests that the large ebb velocities simulated near the forest fringe is an artefact produced by the model; hence the true ebb dominance at this location is most likely attenuated.

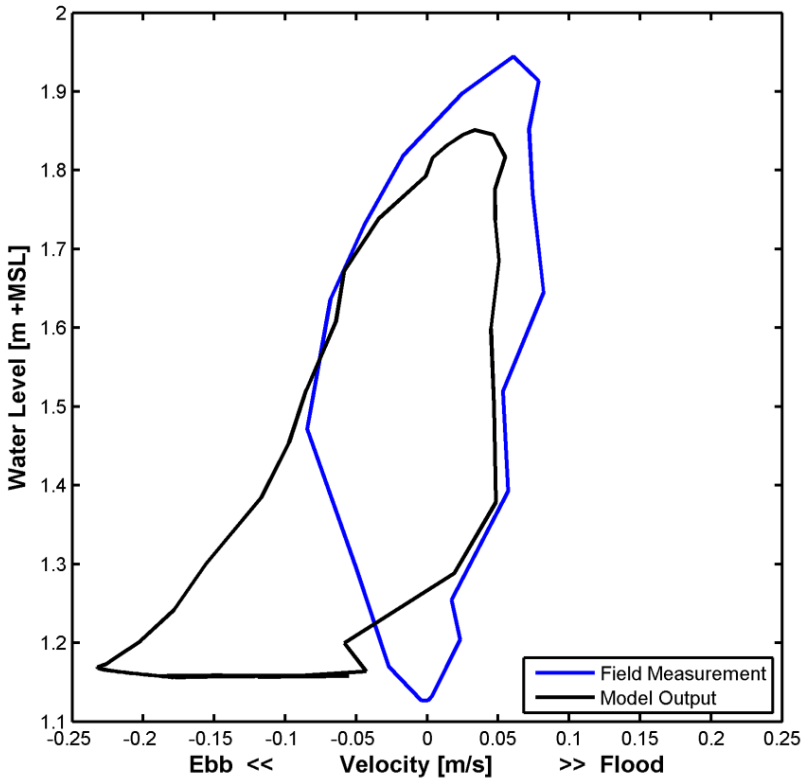

Figure 6. 13: Time averaged tidal stage plot comparing model output from location C4 with Aquadopp current metre data measured during 14th to 25th November, 2016.

6.5 Conclusions

Numerical model simulations indicate that the mangroves in the Firth of Thames do influence the characteristics of tidal wave propagation across the intertidal flats. While the presence of mangroves causes a reduction of the current velocities through the linear effect of friction, it also causes an increase in the tidal asymmetry through the nonlinear friction effect. Increasing friction, in particular through increasing pneumatophore density, increases the magnitude of flood dominance within the mangrove forest and the ebb dominance at the edge of the forest. Limited velocity measurements throughout the forest provide some uncertainty to the simulated ebb velocity patterns; however the simulated flood tide within the forest fringe does show good comparison with field measurements. A more comprehensive validation against velocity and water level measurements throughout the forest would improve the applicability of these results.

CHAPTER SEVEN - IMPLICATIONS, RECOMMENDATIONS AND CONCLUSIONS

7.1 Introduction

Establishing the hydrodynamic patterns in the Firth of Thames is an important step towards understanding the sediment transport patterns, tidal flat morphodynamics and subsequently the long term stability of the system. Determining the true sedimentation patterns within the Firth of Thames would require further numerical modelling and field measurements; nonetheless, the outputs from the present hydrodynamic model provide insight into what the residual sedimentation patterns are likely to be. This chapter discusses the implications of the hydrodynamic patterns for sediment transport within the Firth of Thames. Recommendations for further numerical model improvements are also discussed and overall thesis conclusions are provided.

7.2 Implications for Sediment Transport

The main factors influencing sediment transport patterns within a system are the sediment supply and the sediment characteristics relative to the hydrodynamic energy available for entraining and transporting. Sediment entrainment is typically a function of bed shear stress, which is proportional to flow speed. Subsequent sediment transport depends directly on the currents. Consequently, within estuarine environments, residual sedimentation patterns are largely determined by the relative direction and strength of ebb and flood tidal currents (tidal asymmetry) (Dronkers, 1986). The difference between the maximum tidal currents occurring during the ebb and flood phases tends to affect the residual flux of suspended coarse sediment, whereas the duration of slack water periods between ebb and flood (usually at high tide) tends to affect the residual flux of suspended fine sediment (Dronkers, 1986).

Although exact details of sediment supply and sediment characteristics within the Firth of Thames were not included in this study, the likely sediment transport patterns can be inferred from the hydrodynamics. The tidal asymmetry simulated

by the numerical model, should cause net sediment transport into the mangrove forest, due to the mean flood currents being larger magnitude than the mean ebb currents. This asymmetry effect is also accompanied by a spatial change in the strength of tidal currents. When the incoming tide reduces current velocity as it moves through the forest, it loses the capacity to transport sediment and therefore the suspended sediment settles out. The ebb tide has weaker currents; consequently, it lacks ability to re-suspend the sediment and therefore net deposition would occur within the forest. Just at the fringe, the model showed ebb dominance, which would therefore mean that the net sediment transport would be offshore. This pattern of residual sediment transport would lead to a shore profile where the mangrove tidal flat elevation increases with a convex, steepened slope at the fringe. However, based on the comparison with real velocity measurements the ebb dominance at the fringe may not be as strong as modelled, in which case the offshore flux of sediment at the fringe would be smaller.

The same pattern of tidal asymmetry was also evident when mangroves were not included in the model. Therefore, it is likely that the net accumulation of sediment onto the intertidal flat would occur regardless of whether or not the mangroves are present. This concept is consistent with findings from Swales *et al.*, (2015), where physical processes are attributed to the initial mud-deposition on the upper intertidal flat. However, because the model results show that mangroves further reduce the currents and increase the tidal asymmetry on the upper intertidal flat, it is evident that the mangroves are not just passive opportunists within their environment but instead they do alter the physical conditions and are likely to further enhance the sedimentation rates within the Firth of Thames. In addition to reducing current velocities, the mangroves trap more water on the upper intertidal flat, enhancing the duration of the slack water period and therefore allowing more time for fine sediments to deposit, compared to if there was no vegetation. These predictions of sedimentation patterns are consistent with previous studies which imply mangrove forests behave as sediment sinks (Furukawa *et al.*, 1997; Stokes *et al.*, 2010). My modelled tidal currents at the fringe of the forest can be used to make a rough calculation of the likely supply of sediment into the forest between the time when I did my experimental work (2016), and when the survey published in Swales *et al.*, (2015) was collected (2005) (Figure 7.1). Based on the suspended

sediment concentrations measured by the SCUFA during the field deployment (Chapter 3), and the tidal discharge predicted by the model (Chapter 6), the net flux of sediment into the forest over a tidal cycle can be estimated using Equation 7.1.

$$Net\ sediment\ flux = (Sed_{in} - Sed_{out}) \times T \quad \textbf{(7.1)}$$

Where Sed_{in} and Sed_{out} can be calculated from Equations 7.2 and 7.3, respectively. Sed_{in} is the average flux of suspended sediment into the mangrove forest (kg/m^2/s), Sed_{out} is the average flux of suspended sediment out of the forest (kg/m^2/s) and T is the number of seconds in a tidal cycle (44640 seconds). $\overline{D}_{Flood}$ is the average flood discharge in to the forest (m^3/s), $\overline{D}_{Ebb}$ is the average ebb discharge out of the forest (m^3/s), C_{Flood} is the average offshore suspended sediment concentration on the flood tide (kg/m^3).

$$Sed_{in} = \overline{D}_{Flood} \times C_{Flood} \quad \textbf{(7.2)}$$

$$Sed_{out} = \overline{D}_{Ebb} \times C_{Flood} \quad \textbf{(7.3)}$$

Using the average flood and ebb discharges at the forest fringe, the net sediment flux into the mangrove forest during a single tidal cycle is estimated to be 7.75 kg (Table 7.1). This net sediment flux can be applied to the 11 year period (between 2005 and 2016), and compared to the estimated amount of sediment accumulation based on the 2 transect surveys (Figure 7.1).

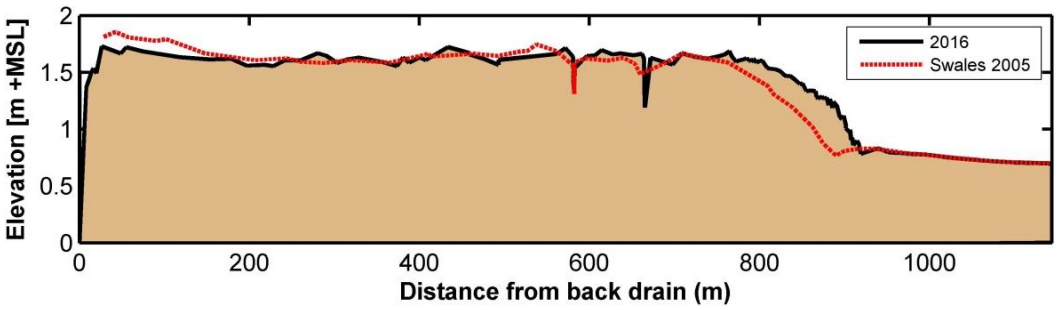

Figure 7. 1: Comparison of the 2005 elevation survey (Swales *et al.*, 2007) and the recent 2016 survey, showing the extent of seaward accretion over the last 11 years.

Table 7. 1: Values of variables used to calculate the net flux of sediment into the forest, based on model results.

Variable	Unit	Value
C_{Flood}	kg/m^3	0.02489
$\overline{D}_{Flood}$	m^3/s	0.00983
$\overline{D}_{Ebb}$	m^3/s	0.00135
Sed_{in}	kg/s	0.00020
Sed_{out}	kg/s	0.00003
Net sediment flux per tidal cycle	kg	7.75
Net sediment flux in 11 years (8030 tidal cycles)	kg	62269

Based on the difference between the 2 surveys (Figure 7.1), the volume of the sediment wedge accumulated at the forest fringe since 2005 can be estimated. Equation 7.4 calculates the total sediment weight (kg) deposited since 2005 (V_{Total}), where v is the wedge volume (m^3), ε_{por} takes into account that bed porosity is 0.4 (following van Maanen, 2011) and ρ is the sediment density (kg/m^3) (Table 7.2).

$$V_{Total} = v \times \varepsilon_{por} \times \rho \quad \textbf{(7.4)}$$

Table 7. 2: Values of the variables used to calculate the volume of the sediment wedge accumulated since 2005 (Figure 7.1).

Variable	Unit	Value
v (height x length x width)	m^3	35.8
height	m	0.24
length	m	150
width	m	1
ε_{por}	-	0.6
ρ	kg/m^3	2650
V_{Total}	kg	56954

The rough calculation based on the model outputs shows a net delivery of 62269 kg (39 m^3) for every metre alongshore of mangrove forest (Table 7.1). Although an overestimate, this is surprisingly similar to the approximate volume of the

wedge of sediment that has accumulated since 2005 which is 56954 kg (22 m^3) (Table 7.2). This overestimation is probably because the calculation generalizes the flux of sediment during a spring tide to be the same for all tides throughout the year. It is most likely that during neap tides the sediment flux into the forest is reduced. On the other hand, one could expect a much larger delivery during storm events when suspended sediment concentration in the rivers is elevated. Note that these calculations are extremely simplified, and sediment transport within vegetation can be more complicated than just a function of current strength and the suspended sediment measured offshore. For example, deposition and erosion can occur on the intervening tidal flats, and wind waves can play a strong influence in controlling sediment fluxes. Ideally, more detailed calculations should be included and completed for the full spring-neap cycle.

The rapid accretion shown at the fringe over the last 11 year indicates that the fringe is a strong depositional environment. Indeed, it has often been assumed that when vegetation is really dense the bed can be protected so that the bottom boundary layer of flow occurs at the top of the vegetation rather than within the vegetation canopy (Lopez and Garcia, 1998). Subsequently, based on the low bed shear stress within the mangroves, sediment deposition would be expected to take place. However, Tinoco & Coco (2015) and Yang *et al.*, (2016) discuss how canopy-scale turbulence can play an important role in suspending sediment within vegetation. These studies found that even though current speed is significantly dampened within dense vegetation, the amount of sediment lifted into suspension increased as the vegetation density increased due to the canopy-scale turbulence (Tinoco & Coco, 2015, and Yang *et al.*, 2016). Therefore the role of the pneumatophores in protecting the bed is still under dispute, and many of these new findings are not incorporated in the Delft3D vegetation formulation.

7.3 Recommendations

The present hydrodynamic model successfully simulated the large scale tidal wave propagation through the mangrove forest and has provided insight into the influence of mangroves on hydrodynamics. As with all numerical models, there are limitations and elements that can be improved to increase the accuracy of different aspects of the model.

Firstly, collecting multiple velocity measurements throughout the forest would benefit a more complete model validation. As mentioned in Chapter 6, the low water levels and ebb velocities at the forest fringe did not accurately match the field measurements. One way to improve this aspect would be to increase the threshold depth; however, this may create numerical instability due to the large grid size. Alternatively, the grid resolution across the mangrove forest could be increased so that the small runnels within the forest could also be included in the bathymetry. However, because the runnels are less than 1 m wide, this would significantly increase the computation time. Another option for improvement would be to include the groundwater flux, as this may be where some of the low water levels drain to.

Simulation and analyses of the neap tide hydrodynamics across the mangrove intertidal flat could also be beneficial to understanding further how the mangroves influence the overall hydrodynamics. While the field data indicated that the inner mangrove forest was not inundated during neap tidal cycles, the fringe did show some inundation (Chapter 3) and it would be interesting to determine whether the same hydrodynamic patterns displayed during spring tides, also occur during neap.

The incorporation of vegetation characteristics could also be improved so that there is a variation in density and height across the intertidal flat that is more representative of the true system. Within the real system, the mangrove forest exhibits variations in pneumatophore density and height, which from the sensitivity analysis is shown to significantly influence the water levels and velocities. Therefore, incorporating this density variation in vegetation properties could improve the model accuracy.

In addition, to further explore the effect of the mangroves on the sedimentation patterns, a sediment transport model should be included with the hydrodynamics. Development of the sediment transport model would require an input of sediment supply from the rivers, measurements of sediment grain size and, as mentioned in Section 7.2, the incorporation of canopy-scale turbulence may be important for determining sediment suspension. Furthermore, to understand what influence the mangroves have on the long term stability of the system, an ecogeomorphic model similar to that developed by van Maanen *et al.* (2015) could be applied, to take

into account the two-way biophysical coupling between mangroves and the physical processes.

7.4 Overall Conclusions

The primary aim of this research was to determine whether or not the mangroves in the Firth of Thames influence the tidal wave propagation across the intertidal flats. The development of a hydrodynamic model allowed vegetation to be removed from the system so that the effects of the mangroves could be isolated. Model outputs compared well with field measurements after calibration and the results of numerical experiments imply that the mangroves within the Firth of Thames do alter the large scale hydrodynamic patterns. The main impacts of vegetation include: overall reduced current velocities and tidal amplitude, and enhanced tidal asymmetry, meaning that the flood dominance across the upper intertidal flat and the ebb dominance at the seaward edge of the intertidal flat are increased. The sensitivity analysis indicates the pneumatophores have the largest impact on tidal wave dynamics, as they occur in high densities and thus impose the most drag on the tidal wave. The trees, although providing the largest visual impact of the forest, are mostly above water and so do not influence the flows significantly.

Physical processes, such as tidal asymmetry, are likely to have caused the initial accretion and tidal flat development, making it suitable for mangrove growth. However, now that there is a vast area of mangroves, they are altering the hydrodynamics and therefore are also contributing to the accretion and overall stability of the system. Some questions to explore in future studies are: to what extent are the mangroves enhancing sedimentation rates and, without the mangroves, would the system continue to accrete and be able to keep up with sea level rise?

REFERENCES

Alongi, D. M. (2008). Mangrove forests: resilience, protection from tsunamis, and responses to global climate change. Estuarine, Coastal and Shelf Science, 76(1), 1-13.

Aucan, J., & Ridd, P. V. (2000). Tidal asymmetry in creeks surrounded by saltflats and mangroves with small swamp slopes. *Wetlands Ecology and Management*, *8*(4), 223-232.

Balke, T., Swales, A., Lovelock, C. E., Herman, P. M., & Bouma, T. J. (2015). Limits to seaward expansion of mangroves: translating physical disturbance mechanisms into seedling survival gradients. *Journal of Experimental Marine Biology and Ecology*, *467*, 16-25.

Baptist, M. J. (2005). *Modelling floodplain biogeomorphology* (Doctoral dissertation, TU Delft, Delft University of Technology).

Baptist, M., Babovic, V., Rodríguez Uthurburu, J., Keijzer, M., Uittenbogaard, R., Mynett, A., & Verwey, A. (2007). On inducing equations for vegetation resistance. Journal of Hydraulic Research, 45(4), 435-450.

Brown, J. M. & Davies, A. G. (2007). Flood/ebb tidal dominance in an estuary: sediment transport and morphology. In: Proceedings of 5th IAHR international symposium on 'river, coastal and estuarine morphodynamics', University of Twente, Enschede, The Netherlands, 17–21 September 2007, vol 2, pp 779–787.

Deltares Systems. (2014). Delft3D-FLOW: Simulation of multi-dimensional hydrodynamic flows and transport phenomena, including sediments. (UserManual: Hydro morphodynamics). Rotterdamseweg, The Netherlands: Deltares.

Donato, D. C., Kauffman, J. B., Murdiyarso, D., Kurnianto, S., Stidham, M., & Kanninen, M. (2011). Mangroves among the most carbon-rich forests in the tropics. Nature Geoscience, 4(5), 293-297.

Dronkers, J. (1986). Tidal asymmetry and estuarine morphology. *Netherlands Journal of Sea Research*, *20*(2-3), 117-131.

Duke, N. C., Meynecke, J.O., Dittmann, S., Ellison, A. M., Anger, K., Berger, U., Field, C. D. (2007). A world without mangroves? Science, 317(5834), 41-42.

Friedrichs, C. T., & Aubrey, D. G. (1988). Non-linear tidal distortion in shallow well-mixed estuaries: a synthesis. *Estuarine, Coastal and Shelf Science*, *27*(5), 521-545.

Furukawa, K., Wolanski, E., & Mueller, H. (1997). Currents and sediment transport in mangrove forests. Estuarine, Coastal and Shelf Science, 44(3), 301-310.

Ghisalberti, M. (2009). Obstructed shear flows: similarities across systems and scales. Journal of Fluid Mechanics, 641, 51-61.

Green, M., Zeldis, J. (2015). Firth of Thames water quality and ecosystem health. Waikato Regional Council Technical Report 2015/23.

Horstman, E., Dohmen-Janssen, C., Bouma, T., & Hulscher, S. (2015). Tidal-scale flow routing and sedimentation in mangrove forests: Combining field data and numerical modelling. Geomorphology, 228, 244-262.

Horstman, E. M., Dohmen-Janssen, C. M., & Hulscher, S. J. (2013). Flow routing in mangrove forests: A field study in Trang province, Thailand. Continental Shelf Research, 71, 52-67.

Kirwan, M. L., & Megonigal, J. P. (2013). Tidal wetland stability in the face of human impacts and sea-level rise. *Nature*, *504*(7478), 53-60.

Lessa, G., & Masselink, G. (1995). Morphodynamic evolution of a macrotidal barrier estuary. *Marine Geology*, *129*(1), 25-46.

Lesser, G. R., Roelvink, J. A., Van Kester, J. A. T. M., & Stelling, G. S. (2004). Development and validation of a three-dimensional morphological model. *Coastal engineering*, *51*(8), 883-915.

Li, L., Wang, X. H., Williams, D., Sidhu, H., & Song, D. (2012). Numerical studyof the effects of mangrove areas and tidal flats on tides: A case study of Darwin Harbour, Australia. *Journal of Geophysical Research: Oceans*, *117*(C6).

Lopez, F., Garcia, M., (1998). Open-channel flow through simulated vegetation: suspended sediment transport modelling, *Water Resources Research 34(9)*: 2341–2352, 612 DOI:10.1029/98WR01922.

Lovelock, C. E., Sorrell, B. K., Hancock, N., Hua, Q., & Swales, A. (2010). Mangrove forest and soil development on a rapidly accreting shore in New Zealand. Ecosystems, 13(3), 437-451.

Lovelock, C. E., Cahoon, D. R., Friess, D. A., Guntenspergen, G. R., Krauss, K. W., Reef, R., & Saintilan, N. (2015). The vulnerability of Indo-Pacific mangrove forests to sea-level rise. *Nature*.

Mariotti, G., & Fagherazzi, S. (2010). A numerical model for the coupled long-term evolution of salt marshes and tidal flats. Journal of Geophysical Research: Earth Surface (2003–2012), 115(F1).

Mariotti, G., & Fagherazzi, S. (2013). A two-point dynamic model for the coupled evolution of channels and tidal flats. Journal of Geophysical Research: Earth Surface, 118(3), 1387-1399.

Massel, S., Furukawa, K., & Brinkman, R. (1999). Surface wave propagation in mangrove forests. Fluid Dynamics Research, 24(4), 219-249.

Mazda, Y., Kanazawa, N., & Wolanski, E. (1995). Tidal asymmetry in mangrove creeks. In *Asia-Pacific Symposium on Mangrove Ecosystems* (pp. 51-58). Springer Netherlands.

Nepf, H. M. (1999). Drag, turbulence, and diffusion in flow through emergent vegetation. *Water resources research*, *35*(2), 479-489.

Nepf, H. M. (2012). Flow and transport in regions with aquatic vegetation. *Annual Review of Fluid Mechanics*, *44*, 123-142.

Oldman, J.W., Senior, A., Haskew, R., Ramsay, D. (2004). Hauraki regional harbour model: set-up, calibration and verification. NIWA Client Report: HAM2004-038.

Parker, B. B. (1984). Frictional effects on the tidal dynamics of a shallow estuary.

Pawlowicz, R., Beardsley, B., & Lentz, S. (2002). Classical tidal harmonic analysis including error estimates in MATLAB using T-TIDE. Computers and Geosciences, 28(8), 929-937.

Soulsby, R. (1997). *Dynamics of marine sands: a manual for practical applications*. Thomas Telford.

Speer, P. E., & Aubrey, D. G. (1985). A study of non-linear tidal propagation in shallow inlet/estuarine systems Part II: Theory. *Estuarine, Coastal and Shelf Science*, *21*(2), 207-224.

Stephens, S. (2003). Ecological sustainability assessment for Firth of Thames shellfish aquaculture: Task 1-hydrodynamic modelling. *NIWA Report HAM2003-113. 32p*.

Stokes, D. J., Healy, T. R., & Cooke, P. J. (2010). Expansion dynamics of monospecific, temperate mangroves and sedimentation in two embayments of a barrier-enclosed lagoon, Tauranga Harbour, New Zealand. Journal of Coastal Research, 113-122.

Swales, A., Bentley, S. J., Lovelock, C., & Bell, R. G. (2007). Sediment processes and mangrove-habitat expansion on a rapidly-prograding muddy coast, New Zealand. Paper presented at the Coastal Sediments.

Swales, A., Bentley, S. J., & Lovelock, C. E. (2015). Mangrove-forest evolution in a sediment-rich estuarine system: Opportunists or agents of geomorphic change? Earth Surface Processes and Landforms.

Temmerman, S., Govers, G., Meire, P., & Wartel, S. (2003). Modelling long-term tidal marsh growth under changing tidal conditions and suspended sediment concentrations, Scheldt estuary, Belgium. Marine Geology, 193(1), 151-169.

Tinoco, R. O., & Coco, G. (2016). A laboratory study on sediment resuspension within arrays of rigid cylinders. *Advances in Water Resources*, *92*, 1-9.

van Maanen, B. (2011). *Modelling the long-term morphological evolution of tidal embayments* (Doctoral dissertation, University of Waikato).

van Maanen, B., Coco, G., & Bryan, K. (2015). On the ecogeomorphological feedbacks that control tidal channel network evolution in a sandy mangrove setting. Paper presented at the Proc. R. Soc. A.

van Rijn, L. C., Walstra, D. J. R., Grasmeijer, B., Sutherland, J., Pan, S., & Sierra , J. P. (2003). The predictability of cross-shore bed evolution of sandy beaches at the time scale of storms and seasons using process-based profile models. *Coastal Engineering*, *47*(3), 295-327.

van Rijn, L. C. (2010). Tidal phenomena in the Scheldt Estuary. *Report, Deltares*, 105.

Walters, R. A., Goring, D. G., & Bell, R. G. (2001). Ocean tides around New Zealand. *New Zealand Journal of Marine and Freshwater Research*, *35*(3), 567-579.

Willemsen, P. W. J. M., Horstman, E. M., Borsje, B. W., Friess, D. A., & Dohmen-Janssen, C. M. (2016). Sensitivity of the sediment trapping capacity of an estuarine mangrove forest. *Geomorphology, 273*, 189-201. doi:http://dx.doi.org/10.1016/j.geomorph.2016.07.038

Winter, C. (2007). On the evaluation of sediment transport models in tidal environments. *Sedimentary Geology*, *202*(3), 562-571.

Winterwerp, J., Erftemeijer, P., Suryadiputra, N., Van Eijk, P., & Zhang, L. (2013). Defining eco-morphodynamic requirements for rehabilitating eroding mangrove-mud coasts. Wetlands, 33(3), 515-526.

Wolanski, E., Jones, M., & Bunt, J. (1980). Hydrodynamics of a tidal creek-mangrove swamp system. Marine and Freshwater Research, 31(4), 431-450.

Wolanski, E., & Ridd, P. (1986). Tidal mixing and trapping in mangrove swamps. Estuarine, Coastal and Shelf Science, 23(6), 759-771.

Wolanski, E., Mazda, Y., King, B., & Gay, S. (1990). Dynamics, flushing and trapping in Hinchinbrook Channel, a giant mangrove swamp, Australia. *Estuarine, Coastal and Shelf Science*, *31*(5), 555-579.

Wolanski, E. (1995). Transport of sediment in mangrove swamps. In *Asia-Pacific Symposium on Mangrove Ecosystems* (pp. 31-42). Springer Netherlands.

Woodroffe, C. D. (1990). The impact of sea-level rise on mangrove shorelines. Progress in Physical Geography, 14(4), 483-520.

Yang, J. Q., Chung, H., & Nepf, H. M. (2016). The onset of sediment transport in vegetated channels predicted by turbulent kinetic energy. *Geophysical Research Letters*, *43*(21).

Young, B. M., & Harvey, E. L. (1996). A spatial analysis of the relationship between mangrove (Avicennia marinavar. australasica) physiognomy and sediment accretion in the Hauraki Plains, New Zealand. *Estuarine, Coastal and Shelf Science, 42*(2), 231-246.

APPENDIX I

		Pneumatophores				Trees		
	Site #	**Number per 0.5 m^2**	**Height (mm)**	**d_bot (mm)**	**d_top (mm)**	**Number per 1 m^2**	**Height (m)**	**d_0.3 (mm)**
Average	1	0						
	2	32	254	8	4			
	3	96	229	7	4	1	1.87	40.08
	4	97	170	6	4	1	2.90	58.00
	5	81	125	7	4	6.4	2.34	29.60
	6	89	77	8	4	11.4	1.52	28.40
Maximum	1	0						
	2	118	389	10	6			
	3	137	364	11	6	3	3	110
	4	118	335	11	7	2	3.2	104
	5	104	210	12	5	7	2.6	38
	6	138	212	12	11	15	1.8	44
Minimum	1	0						
	2	2	62	6	3			
	3	68	52	5	3	0	0.8	0.23
	4	74	39	3	2	0	2.6	37
	5	62	30	4	3	6	2.1	23
	6	39	16	5	3	9	1	11

*d_0.3 = stem diameter at 30cm above the bed, d_bot = basal diameter of pneumatophore, d_top = diameter at top of pnematophore.